SEARCH FOR THE HIGGS BOSON IN THE $ZH \rightarrow \nu\nu b\bar{b}$ CHANNEL AT CDF RUN II

DISSERTATION

Presented in Partial Fulfillment of the Requirements for

the Degree Doctor of Philosophy in the

Graduate School of The Ohio State University

By

Brandon Scott Parks, B.S., M.S.

* * * * *

The Ohio State University

2008

Dissertation Committee:

Prof. Brian L. Winer, Adviser

Prof. Richard E. Hughes

Prof. Junko Shigemitsu

Prof. Linn Van Woerkom

Approved by

Adviser

Graduate Program in Physics

ABSTRACT

This analysis focuses on a low mass Higgs boson search with 1.7 fb^{-1} of data. The focus is on Higgs events in which it is produced in association with a W or Z boson. Such events are expected to leave a distinct signature of large missing transverse energy for either a Z$\rightarrow$ $\nu\nu$ decay or a leptonic W decay in which the lepton goes undetected, as well as jets with taggable secondary vertices from the H$\rightarrow$ $b\bar{b}$ decay. Utilizing a new track based technique for removing QCD multi-jet processes as well as a neural network discriminant, an expected limit of 8.3 times the Standard Model prediction at the 95% CL for a Higgs boson mass of 115 GeV/c^2 is calculated, with an observed limit of 8.0*SM.

For my daughter Elise Rose and to the memory of Maya Grace

ACKNOWLEDGMENTS

Where do I begin. It has been a long, difficult, inspiring, enlightening, enjoyable experience for me at THE Ohio State University. First, I would like to thank my adviser Brichard. The efficiency with which you could advise students while performing your own physics analysis simultaneously often made it seem like you were in two places at once. In fact, strangely enough, there almost seemed to be two connected yet separate personalities. The first, named Richard, gave me a foundation with which I could build confidence and independence. Throughout the duration of graduate school, seeing the way he thought and reacted created a new and improved version of myself. I learned quickly that physics analysis is 25% intelligence and 75% creativity. He provided me with a skill set that could not have been obtained from anyone else, and my future career has been molded by the lessons I have learned working closely with him. The second personality preferred to be called Brian. The wealth of knowledge contained there was immense, and I know that I should have exploited it more than I did. However, it was inevitable that at least some of it soaked into me given his close proximity. I had thought it hard to believe that there was a more convenient way to get answers than Google, but I was proven wrong. Any advice I received regarding analysis was essentially truth, and I can only hope to have learned a fraction of what was available to be learned. When these personalities combine to form Brichard, it is an unstoppable force possessing physics skills I find difficult to

comprehend. While I know that I drove you crazy at times, your 'corrections' to my proposed analysis strategies have provided me with numerous enhanced capabilities which I know will be invaluable in the future.

Perhaps the greatest part of the Ohio State CDF group is instinct regarding who to hire. Ben Kilminster, my third adviser, is a great friend and an exceptional physicist. I regret not being resident at Fermilab due to the amount of skill and innovation I could have seen on a daily basis. I would like to think that I picked up on some of it remotely. Ben was always the third kick-in-the-pants to move things forward, and provided yet another example of how to be great physicist. Thank you for talking me off the ledge before my 'blessing' and fighting off the waves of attack. Additionally, a fourth adviser, Kevin Lannon, was present whenever I needed him. A large amount of feedback and knowledge came from this source which is likely present nowhere else in the collaboration. Thanks for not getting annoyed with my likely repetitive questions. I would also apologize for the blisters on your fingers you've almost certainly gotten responding to my mail messages, but I've heard that 40 page lectures on physics are common even when someone is just asking if you want to go to lunch.

The team of graduate students I have worked with have been an amazing, amusing and unforgettable group. Three of them were constantly talking about particle physics in 'outer-space', which was a bit strange, but I couldn't blame them for trying to relive their childhood astronaut dreams. Patrick's constant reference to 'right ascension' and 'declination' was really confusing however. I guess that is Texas slang for pseudorapidity and phi. Fred's physics skills were matched only by his ability to B.S., although he tended to buy into this space idea as well. I was really concerned

when they all flew down to Florida to watch a satellite called GLAST launch, claiming that they would finally get data. Finally, I just decided to just tell them that the CDF data I was sending them was from space, and we could measure the Higgs if we measured the aftermath of enough supernova. Jonathan and Jason were more understanding of the actual situation, so I was able to interact and learn from them more. Jonathan's analysis created a road map for all Higgs analysis at CDF. I believe that his moving on to the LHC has been a huge hit to the collaboration which we are still recovering from. Jason has been a great friend and colleague with whom I have shared many ideas and laughs. I hope we can work together in the future, either in physics or stand-up comedy.

I would like to thank all of my family who have supported me throughout my academic career and life. My parents, who have given so much to me and never asked anything in return. Your support has meant more to me than I will likely ever convey, and you have given me strength in the times in which I have needed it most. My sister has been a shining example of generosity, love and kindness to all those who need it most. If no one else will laugh at my jokes, I usually have you there to laugh with me. And finally, to my wife and daughter who are the loves of my life. Elise never fails to make me smile, no matter what the situation. You are my inspiration and my joy. Esther, you have given me more than I could have ever asked for. Thank you for being patient and for being the balance in my life. Your everyday presence has provided me with something that was never there before. I look forward to the coming years with great excitement, and thank you for giving me all that I need.

VITA

May 2002 ..... B.S. in Physics, Purdue University, West Lafayette, IN

March 2007 ..... M.S. in Physics The Ohio State University, Columbus, OH

PUBLICATIONS

"Search for New High Mass Particles Decaying to Lepton Pairs in $p\bar{p}$ **Collisions at** $\sqrt{s} = 1.96$ **TeV,"** A. Abulencia et al., The CDF Collaboration, Phys. Rev. Lett. **95**, 252001 (2005).

"Search for $B_s^0 \to \mu^+\mu^-$ **and** $B_d^0 \to \mu^+\mu^-$ **Decays in** $p\bar{p}$ **Collisions with CDF II,"** A. Abulencia et al., The CDF Collaboration, Phys. Rev. Lett. **95**, 221805 (2005).

"Measurement of Bottom-Quark Hadron Masses in Exclusive J/ψ **Decays with the CDF Detector,"** D. Acosta et al., The CDF Collaboration, Phys. Rev. Lett. **96**, 202001 (2006).

"Measurement of the Ratios of Branching Fractions $\mathcal{B}(B_s^0 \to D_s^- \pi^+)/\mathcal{B}(B^0 \to D^- \pi^+)$ **and** $\mathcal{B}(B^0 \to \overline{D}^0 \pi^+)/\mathcal{B}(B^0 \to D^- \pi^+)$**,"** A. Abulencia et al., The CDF Collaboration, Phys. Rev. Lett. **96**, 191801 (2006).

"Search for Neutral Higgs Bosons of the Minimal Supersymmetric Standard Model Decaying to τ **Pairs in** $p\bar{p}$ **Collisions at** $\sqrt{s} = 1.96$ **TeV,"** A. Abulencia et al., The CDF Collaboration, Phys. Rev. Lett. **96**, 011802 (2006).

"Direct Search for Dirac Magnetic Monopoles in $p\bar{p}$ Collisions at $\sqrt{s} = 1.96$ TeV," A. Abulencia et al., The CDF Collaboration, Phys. Rev. Lett. **96**, 201801 (2006).

"Top Quark Mass Measurement Using the Template Method in the Lepton + Jets Channel at CDF II," A. Abulencia et al., The CDF Collaboration, Phys. Rev. D **73**, 032003 (2006).

"Precision Top Quark Mass Measurement in the Lepton + Jets Topology in $p\bar{p}$ Collisions at $\sqrt{s} = 1.96$ TeV," A. Abulencia et al., The CDF Collaboration, Phys. Rev. Lett. **96**, 022004 (2006).

"A Search for $t \to \tau\nu q$ in $t\bar{t}$ Production," A. Abulencia et al., The CDF Collaboration, Phys. Lett. B 639 (2006) p. 172.

"Search for Charged Higgs Bosons from Top Quark Decays in $p\bar{p}$ Collisions at $\sqrt{s} = 1.96$ TeV," A. Abulencia et al., The CDF Collaboration, Phys. Rev. Lett. **96**, 042003 (2006).

"Measurement of the Helicity of W Bosons in Top-Quark Decays," A. Abulencia et al., The CDF Collaboration, Phys. Rev. D**73**, 111103 (2006).

"Evidence for the Exclusive Decay $B_c^{\pm}$ $J/\psi\pi^{\pm}$ and Measurement of the Mass of the $B_c^{\pm}$ Meson," A. Abulencia et al., The CDF Collaboration, Phys. Rev. Lett. **96**, 082002 (2006).

"Measurement of the Top Quark Mass with the Dynamical Likelihood Method using Lepton plus Jets Events with b-tags in $p\bar{p}$ Collisions at $\sqrt{s} = 1.96$ TeV," A. Abulencia et al., The CDF Collaboration, Phys. Rev. D**73**, 092002 (2006).

"Measurement of the Inclusive Jet Cross Section in $p\bar{p}$ Interactions at $\sqrt{s} = 1.96$ TeV Using a Cone-based Jet Algorithm," A. Abulencia et al., The CDF Collaboration, Phys. Rev. D**74**, 071103 (2006).

"Measurement of $\sigma_{\Lambda_b^0}/\sigma_{\overline{b}^0} \times B(\Lambda_b^0 \to \Lambda_c^+\pi^-)/B(\overline{B}^0 \to D^+\pi^-)$ in $p\bar{p}$ Collisions at $\sqrt{s} = 1.96$ TeV," A. Abulencia et al., The CDF Collaboration, Phys. Rev. Lett. **98**, 122002 (2007).

"Measurement of the Dipion Mass Spectrum in $X(3872) \to J/\psi\pi^+\pi^-$ Decays," A. Abulencia et al., The CDF Collaboration, Phys. Rev. Lett. **96**, 102002 (2006).

"Search for Second-Generation Scalar Leptoquarks in $p\bar{p}$ Collisions at $\sqrt{s}$ = 1.96 TeV," A. Abulencia et al., The CDF Collaboration, Phys. Rev. D**73**, 051102 (2006).

"Search for Higgs Bosons Decaying to $b\bar{b}$ and Produced in Association with W Bosons in $p\bar{p}$ Collisions at $\sqrt{s}$ = 1.96 TeV," A. Abulencia et al., The CDF Collaboration, Phys. Rev. Lett. **96**, 081803 (2006).

"Top Quark Mass Measurement from Dilepton Events at CDF II," A. Abulencia et al., The CDF Collaboration, Phys. Rev. Lett. **96**, 152002 (2006).

"A Search for Scalar Bottom Quarks from Gluino Decays in $\bar{p}p$ Collisions at $\sqrt{s}$ = 1.96 TeV," A. Abulencia et al., The CDF Collaboration, Phys. Rev. Lett. **96**, 171802 (2006).

"Measurement of Mass and Width of the Excited Charmed Meson States D_1^0 and D_2^{*0} at CDF," A. Abulencia et al., The CDF Collaboration, Phys. Rev. D**73**, 051104 (2006).

"Measurement of the Inclusive Jet Cross Section using the K_T Algorithm in $p\bar{p}$ Collisions at $\sqrt{s}$ = 1.96 TeV," A. Abulencia et al., The CDF Collaboration, Phys. Rev. Lett. **96**, 122001 (2006).

"Search for Anomalous Semileptonic Decay of Heavy Flavor Hadrons Produced in Association with a W Boson at CDF II," A. Abulencia et al., The CDF Collaboration, Phys. Rev. D**73**, 0511101 (2006).

"Measurement of the Top Quark Mass using Template Methods on Dilepton Events in $p\bar{p}$ Collisions at $\sqrt{s}$ = 1.96 TeV," A. Abulencia et al., The CDF Collaboration, Phys. Rev. D**73**, 112006 (2006).

"Observation of $B_s^0 \to \psi(2S)\phi$ and Measurement of Ratio of Branching Fractions $\mathcal{B}(B_s^0 \to \psi(2S)\phi)/\mathcal{B}(B_s^0 \to J/\psi\phi)$," A. Abulencia et al., The CDF Collaboration, Phys. Rev. Lett. **96**, 231801 (2006).

"Search for $Z' e^+e^-$ Using Dielectron Mass and Angular Distribution," A. Abulencia et al., The CDF Collaboration, Phys. Rev. Lett. **96**, 211801 (2006).

"Search for High-Mass Resonances Decaying to $e\mu$ in $p\bar{p}$ Collisions at $\sqrt{s}$ = 1.96 TeV," A. Abulencia et al., The CDF Collaboration, Phys. Rev. Lett. **96**, 211802 (2006).

"Measurement of the B_c^+ Meson Lifetime Using $B_c^+ \to J/\psi e^+ \nu_e$," A. Abulencia et al., The CDF Collaboration, Phys. Rev. Lett. **97**, 012002 (2006).

"Measurement of the $t\bar{t}$ Production Cross Section in $p\bar{p}$ Collisions at $\sqrt{s}$ = 1.96 TeV using Missing E_T+jets Events with Secondary Vertex b-Tagging," A. Abulencia et al., The CDF Collaboration, Phys. Rev. Lett. **96**, 202002 (2006).

"Search for Large Extra Dimensions in the Production of Jets and Missing Transverse Energy in $p\bar{p}$ Collisions at $\sqrt{s}$ = 1.96 TeV," A. Abulencia et al., The CDF Collaboration, Phys. Rev. Lett. **97**, 171802 (2006).

"Measurement of the Ratio of Branching Fractions B($D^0 \to K^+\pi^-$)/$D^0 \to K^-\pi^+$) using the CDF II Detector," A. Abulencia et al., The CDF Collaboration, Phys. Rev. **D74**, 031109 (2006).

"Search for New Physics in Lepton + Photon + X Events with 305 pb^{-1} of $p\bar{p}$ Collisions at $\sqrt{s}$ = 1.96 TeV," A. Abulencia et al., The CDF Collaboration, Phys. Rev. Lett. **97**, 031801 (2006).

"Measurement of the b Jet Cross Section in Events with a Z Boson in $p\bar{p}$ Collisions at $\sqrt{s}$ = 1.96 TeV," A. Abulencia et al., The CDF Collaboration, Phys. Rev. **D74**, 032008 (2006).

"Search for a Neutral Higgs Boson Decaying to a W Boson Pair in $p\bar{p}$ Collisions at $\sqrt{s}$ = 1.96 TeV," A. Abulencia et al., The CDF Collaboration, Phys. Rev. Lett. **97**, 081802 (2006).

"Top Quark Mass Measurement from Dilepton Events at CDF II with the Matrix-Element Method," A. Abulencia et al., The CDF Collaboration, Phys. Rev. **D74**, 032009 (2006).

"Measurement of the $t\bar{t}$ Production Cross Section in $p\bar{p}$ Collisions at $\sqrt{s}$ = 1.96 TeV," A. Abulencia et al., The CDF Collaboration, Phys. Rev. Lett. **97**, 082004 (2006).

"Measurement of the $B_s^0 - \bar{B}_s^0$ Oscillation Frequency," A. Abulencia et al., The CDF Collaboration, Phys. Rev. Lett. **97**, 062003 (2006).

"Search for Excited and Exotic Muons in the $\mu\gamma$ Decay Channel in $p\bar{p}$ Collisions at $\sqrt{s}$ = 1.96 TeV," A. Abulencia et al., The CDF Collaboration, Phys. Rev. Lett. **97**, 191802 (2006).

"Observation of $B_s^0 \to K^+K^-$ and Measurements of Branching Fractions of Charmless Two-body Decays of B^0 and B_s^0 Mesons in $\bar{p}p$ Collisions at $\sqrt{s}$ = 1.96 TeV," A. Abulencia et al., The CDF Collaboration, Phys. Rev. Lett. **97**, 211802 (2006).

"Measurement of the $t\bar{t}$ Production Cross Section in $p\bar{p}$ Collisions at $\sqrt{s}$ = 1.96 TeV using Lepton + Jets Events with Jet Probability b-Tagging," A. Abulencia et al., The CDF Collaboration, Phys. Rev. **D74**, 072006 (2006).

"Measurement of the $t\bar{t}$ Production Cross Section in $p\bar{p}$ Collisions at $\sqrt{s}$ = 1.96 TeV in the All Hadronic Decay Mode," A. Abulencia et al., The CDF Collaboration, Phys. Rev. **D74**, 072005 (2006).

"Observation of $B_s^0 - \bar{B}_s^0$ Oscillations," A. Abulencia et al., The CDF Collaboration, Phys. Rev. Lett. **97**, 242003 (2006).

"Search for V + A Current in Top Quark Decay in $p\bar{p}$ Collisions at $\sqrt{s}$ = 1.96 TeV," A. Abulencia et al., The CDF Collaboration, Phys. Rev. Lett. **98**, 072001 (2007).

"Measurement of the Λ_b^0 Lifetime in $\Lambda_b^0 \to J/\psi\Lambda^0$ in $p\bar{p}$ Collisions at $\sqrt{s}$ = 1.96 TeV," A. Abulencia et al., The CDF Collaboration, Phys. Rev. Lett. **98**, 122001 (2007).

"Measurement of the Ratios of Branching Fractions $B(B_s^0 \to D_s^-\pi^+\pi^+\pi^-)/B(B^0 \to D^-\pi^+\pi^+\pi^-)$ and $B(B_s^0 \to D_s^-\pi^+)/B(B^0 \to D^-\pi^+)$," A. Abulencia et al., The CDF Collaboration, Phys. Rev. Lett. **98**, 061802 (2007).

"Search for W' Boson Decaying to Electron-Neutrino Pairs in $p\bar{p}$ Collisions at $\sqrt{s}$ = 1.96 TeV," A. Abulencia et al., The CDF Collaboration, Phys. Rev. **D75**, 091101 (2007).

"Measurements of Inclusive W and Z Cross Sections in $p\bar{p}$ Collisions at $\sqrt{s}$ = 1.96 TeV," A. Abulencia et al., The CDF Collaboration, J. Phys. G: Nucl. Part. Phys. 34 (2007) 2457-2544.

"Observation of Exclusive Electron-Positron Production in Hadron-Hadron Collisions," A. Abulencia et al., The CDF Collaboration, Phys. Rev. Lett. **98**, 112001 (2007).

"Measurement of the Helicity Fractions of W Bosons from Top Quark Decays using Fully Reconstructed $t\bar{t}$ Events with CDF II," A. Abulencia et al., The CDF Collaboration, Phys. Rev. D**75**, 052001 (2007).

"Measurement of the B^+ Production Cross Section in $p\bar{p}$ Collisions at $\sqrt{s}$ = 1960 GeV," A. Abulencia et al., The CDF Collaboration, Phys. Rev. D**75**, 012010 (2007).

"Search for Exotic S = -2 Baryons in $p\bar{p}$ Collisions at $\sqrt{s}$ = 1.96 TeV," A. Abulencia et al., The CDF Collaboration, Phys. Rev. D**75**, 032003 (2007).

"Measurement of the Top-Quark Mass in All-Hadronic Decays in $p\bar{p}$ Collisions at CDF II," A. Abulencia et al., The CDF Collaboration, Phys. Rev. Lett. **98**, 142001 (2007).

"Search for Anomalous Production of Multilepton Events in $p\bar{p}$ Collisions at $\sqrt{s}$ = 1.96 TeV," A. Abulencia et al., The CDF Collaboration, Phys. Rev. Lett. **98**, 131804 (2007).

"Analysis of the Quantum Numbers J^{PC} of the X(3872)," A. Abulencia et al., The CDF Collaboration, Phys. Rev. Lett. **98**, 132002 (2007).

"Measurement of the Top Quark Mass in $p\bar{p}$ Collisions at $\sqrt{s}$ = 1.96 TeV using the Decay Length Technique," A. Abulencia et al., The CDF Collaboration, Phys. Rev. D**75**, 071102 (2007).

"Precision Measurement of the Top Quark Mass from Dilepton Events at CDF II," A. Abulencia et al., The CDF Collaboration, Phys. Rev. D**75**, 031105 (2007).

"Measurement of the Inclusive Jet Cross Section using the k_T Algorithm in $p\bar{p}$ Collisions at $\sqrt{s}$ = 1.96 TeV with the CDF II Detector," A. Abulencia et al., The CDF Collaboration, Phys. Rev. D**75**, 092006 (2007).

"First Measurement of the Ratio of Central-Electron to Forward-Electron W Partial Cross Sections in $p\bar{p}$ Collisions at $\sqrt{s} = 1.96$ TeV," A. Abulencia et al., The CDF Collaboration, Phys. Rev. Lett. **98**, 251801 (2007).

"Observation of WZ Production," A. Abulencia et al., The CDF Collaboration, Phys. Rev. Lett. **98**, 161801 (2007).

"Search for New Physics in Lepton + Photon + X Events with $929 pb^{-}1$ **of** $p\bar{p}$ **Collisions at $\sqrt{s} = 1.96$ TeV,"** A. Abulencia et al., The CDF Collaboration, Phys. Rev. D **75**, 112001 (2007).

"Measurement of $\sigma(p\bar{p} \rightarrow Z) \cdot \mathcal{B}(Z \rightarrow \tau\tau)$ in $p\bar{p}$ Collisions at $\sqrt{s} = 1.96$ TeV," A. Abulencia et al., The CDF Collaboration, Phys. Rev. D**75**, 092004 (2007).

"Inclusive Search for New Physics with Like-Sign Dilepton Events in $p\bar{p}$ Collisions at $\sqrt{s} = 1.96$ TeV," A. Abulencia et al., The CDF Collaboration, Phys. Rev. Lett. **98**, 221803 (2007).

"Measurement of $\sigma\chi_{c2}\,\mathcal{B}(\chi_{c2} \rightarrow J/\psi\gamma)/\sigma\chi_{c1}\,\mathcal{B}(\chi_{c1} \rightarrow J/\psi\gamma)$ in $p\bar{p}$ Collisions at $\sqrt{s} = 1.96$ TeV," A. Abulencia et al., The CDF Collaboration, Phys. Rev. Lett. **98**, 232001 (2007).

"Measurement of the Top-Quark Mass Using Missing E_T + Jets Events with Secondary Vertex b-tagging at CDF II," T. Aaltonen et al., The CDF Collaboration, Phys. Rev. D**75**, 111103 (2007).

"Search for New Particles Leading to Z+jets Final States in $p\bar{p}$ Collisions at $\sqrt{s} = 1.96$ TeV," T. Aaltonen et al., The CDF Collaboration, Phys. Rev. D**76**, 072006 (2007).

"Limits on Anomalous Triple Gauge Couplings in $p\bar{p}$ Collisions at $\sqrt{s} = 1.96$ TeV," T. Aaltonen et al., The CDF Collaboration, Phys. Rev. D**76**, 111103 (2007).

"Measurement of the $p\bar{p} \rightarrow t\bar{t}$ Production Cross Section and the Top Quark Mass at $\sqrt{s} = 1.96$ TeV in the All-Hadronic Decay Mode," T. Aaltonen et al., The CDF Collaboration, Phys. Rev. D**76**, 072009 (2007).

"Observation and Mass Measurement of the Baryon Ξ_b^-," T. Aaltonen et al., The CDF Collaboration, Phys. Rev. Lett. **99**, 052002 (2007).

"Search for Heavy, Long-Lived Particles that Decay to Photons at CDF II," A. Abulencia et al., The CDF Collaboration, Phys. Rev. Lett. **99**, 121801 (2007).

"Polarization of J/ψ and ψ(2S) Mesons Produced in $p\bar{p}$ Collisions at $\sqrt{s}$ = 1.96 TeV," A. Abulencia et al., The CDF Collaboration, Phys. Rev. Lett. **99**, 132001 (2007).

"First Measurement of the W Boson Mass in Run II of the Tevatron," T. Aaltonen et al., The CDF Collaboration, Phys. Rev. Lett. **99**, 151801 (2007).

"Search for a High-Mass Diphoton State and Limits on Randall-Sundrum Gravitons at CDF," T. Aaltonen et al., The CDF Collaboration, Phys. Rev. Lett. **99**, 171801 (2007).

"Search for New Physics in High Mass Electron-Positron Events in $p\bar{p}$ Collisions at $\sqrt{s}$ = 1.96 TeV," T. Aaltonen et al., The CDF Collaboration, Phys. Rev. Lett. **99**, 171802 (2007).

"Search for Direct Pair Production of Supersymmetric Top and Supersymmetric Bottom Quarks in $p\bar{p}$ Collisions at $\sqrt{s}$ = 1.96 TeV," T. Aaltonen et al., The CDF Collaboration, Phys. Rev. D**76**, 072010 (2007).

"Precise Measurement of the Top Quark Mass in the Lepton+Jets Topology at CDF II," A. Abulencia et al., The CDF Collaboration, Phys. Rev. Lett. **99**, 182002 (2007).

"Search for Chargino-Neutralino Production in $p\bar{p}$ Collisions at $\sqrt{s}$ = 1.96 TeV," T. Aaltonen et al., The CDF Collaboration, Phys. Rev. lett. **99**, 191806 (2007).

"First Observation of Heavy Baryons Σ_b and Σ_b^*," T. Aaltonen et al., The CDF Collaboration, Phys. Rev. Lett. **99**, 202001 (2007).

"Search for Exclusive $\gamma\gamma$ Production in Hadron-Hadron Collisions," T. Aaltonen et al., The CDF Collaboration, Phys. Rev. Lett. **99**, 242002 (2007).

"Measurement of the Cross Section for W-boson Production in Association with Jets in $p\bar{p}$ Collisions at $\sqrt{s}$ = 1.96 TeV," T. Aaltonen et al., The CDF Collaboration, Phys. Rev. D**77**, 011108 (2008).

"First Observation of the Decay $B_s^0 \to D_s^- D_s^+$ and Measurement of Its Branching Ratio," T. Aaltonen et al., The CDF Collaboration, Phys. Rev. Lett. **100**, 021803 (2008).

"Search for Standard Model Higgs Bosons Produced in Association with W Bosons," T. Aaltonen et al., The CDF Collaboration, Phys. Rev. Lett. **100**, 041801 (2008).

"Cross Section Constrained Top Quark Mass Measurement from Dilepton Events at the Tevatron," T. Aaltonen et al., The CDF Collaboration, Phys. Rev. Lett. **100**, 062005 (2008). arXiv:0710.4037.

"Direct Measurement of the W Boson Width in $p\bar{p}$ Collisions at $\sqrt{s} = 1.96$ TeV," T. Aaltonen et al., The CDF Collaboration, Phys. Rev. Lett. **100**, 071801 (2008). arXiv:0710.4112.

"Observation of Orbitally Excited B_s Mesons," T. Aaltonen et al., The CDF Collaboration, Phys. Rev. Lett. **100**, 082001 (2008).

"Measurement of Inclusive Jet Cross Sections in $Z/\gamma^*(\to e^+e^-)$+Jets Production in $p\bar{p}$ Collisions at $\sqrt{s} = 1.96$ TeV," T. Aaltonen et al., The CDF Collaboration, Phys. Rev. Lett. **100**, 102001 (2008).

"Search for Chargino-Neutralino Production in $p\bar{p}$ Collisions at $\sqrt{s} = 1.96$ TeV with high-p_T Leptons," T. Aaltonen et al., The CDF Collaboration, Phys. Rev. D**77**, 052002 (2008).

"First Measurement of the Production of a W Boson in Association with a Single Charm Quark in $p\bar{p}$ Collisions at $\sqrt{s} = 1.96$ TeV," T. Aaltonen et al., The CDF Collaboration, Phys. Rev. Lett. **100**, 091803 (2008).

"Measurement of Lifetime and Decay Width Difference in $B_s^0 \to J/\psi\phi$ Decays," T. Aaltonen et al., The CDF Collaboration, Phys. Rev. Lett. **100**, 121803 (2008). arXiv:0712.2348.

"Limits on the Production of Narrow $t\bar{t}$ Resonances in $p\bar{p}$ Collisions at $\sqrt{s} = 1.96$ TeV," T. Aaltonen et al., The CDF Collaboration, Phys. Rev. D**77**, 051102 (2008).

"Observation of Exclusive Dijet Production at the Fermilab Tevatron $\bar{p}p$ Collider," T. Aaltonen et al., The CDF Collaboration, Phys. Rev. D**77**, 052004 (2008).

"Search for $B_s^0 \to \mu^+\mu^-$ and $B^0 \to \mu^+\mu^-$ Decays with 2 fb^-1 of $p\bar{p}$ Collisions," T. Aaltonen et al., The CDF Collaboration, Phys. Rev. Lett. **100**, 101802 (2008).

"Evidence for $D^0 - \overline{D}^0$ Mixing Using the CDF II Detector," T. Aaltonen et al., The CDF Collaboration, Phys. Rev. Lett. **100**, 121802 (2008).

"First Flavor-Tagged Determination of Bounds on Mixing-Induced CP Violation in $B_s^0 \to J/\psi\phi$ Decays," T. Aaltonen et al., The CDF Collaboration, Phys. Rev. Lett. **100**, 161802 (2008). arXiv:0712.2397.

"Search for Heavy Top-like Quarks Using Lepton Plus Jets Events in 1.96 TeV $p\bar{p}$ Collisions," T. Aaltonen et al., The CDF Collaboration, Phys. Rev. Lett. **100**, 161803 (2008). arXiv:0801.3877.

"Measurement of Ratios of Fragmentation Fractions for Bottom Hadrons in $p\bar{p}$ Collisions at $\sqrt{s} = 1.96$ TeV," T. Aaltonen et al., The CDF Collaboration, Phys. Rev. D**77**, 072003 (2008). arXiv:0801.3877.

"Measurement of Correlated $b\bar{b}$ Production in $p\bar{p}$ Collisions at $\sqrt{s} = 1960$ GeV," T. Aaltonen et al., The CDF Collaboration, Phys. Rev. D**77**, 072004 (2008).

"Search for Third Generation Vector Leptoquarks in $p\bar{p}$ Collisions at $\sqrt{s} =$ 1.96 TeV," T. Aaltonen et al., The CDF Collaboration, Phys. Rev. D**77**, 091105 (2008).

"Two-particle Momentum Correlations in Jets Produced in $p\bar{p}$ Collisions at $\sqrt{s} = 1.96$ TeV," T. Aaltonen et al., The CDF Collaboration, Phys. Rev. D**77**, 092001 (2008). arXiv:0802.3182.

"First Run II Measurement of the W Boson Mass," T. Aaltonen et al., The CDF Collaboration, Phys. Rev. D**77**, 112001 (2008).

"Observation of the Decay $B_c^\pm \to J/\psi\pi^\pm$ and Measurement of the $B_c^\pm$ Mass," T. Aaltonen et al., The CDF Collaboration, Phys. Rev. Lett. **100**, 182002 (2008).

"Strong Evidence for ZZ Production in $p\bar{p}$ Collisions at $\sqrt{s} = 1.96$ TeV," T. Aaltonen et al., The CDF Collaboration, Phys. Rev. Lett. **100**, 201801 (2008). arXiv:0801.4806.

"Search for the Higgs Boson in Events with Missing Transverse Energy and b Quark Jets Produced in $p\bar{p}$ Collisions at $\sqrt{s} = 1.96$ TeV," T. Aaltonen et al., The CDF Collaboration, Phys. Rev. Lett. **100**, 211801 (2008).

"Search for Resonant $t\bar{t}$ Production in $p\bar{p}$ Collisions at $\sqrt{s} = 1.96$ TeV," T. Aaltonen et al., The CDF Collaboration, Phys. Rev. Lett. **100**, 231801 (2008).

"Cross Section Measurements of High-p_T Dilepton Final-State Processes Using a Global Fitting Method," A. Abulencia et al., The CDF Collaboration, submitted to Phys. Rev. D Rapid Communications December 22, 2006. Fermilab-Pub-06-486-E.

"Measurement of the Ratio of Branching Fractions $B(B^+ \to J/\psi\pi^+)/B(B^+ \to J/\psi K^+)$**,"** A. Abulencia et al., The CDF Collaboration, submitted to Phys. Rev. D Rapid Communications, January 25, 2007. Fermilab-Pub-07-170-E.

"Search for Doubly Charged Higgs Bosons with Lepton-Flavor-Violating Decays involving Tau Leptons," T. Aaltonen et al., The CDF Collaboration, submitted to Phys. Rev. Lett. December 10, 2007. Fermilab-Pub-07-709-E.

"Model-Independent and Quasi-Model-Independent Search for New Physics at CDF," T. Aaltonen et al., The CDF Collaboration, submitted to Phys, Rev. D December 11, 2007. Fermilab-Pub-07-657-E. arXiv:0712.1311.

"Model-Independent Global Search for New High-p_T Physics at CDF," T. Aaltonen et al., The CDF Collaboration, submitted to Phys. Rev. Lett. December 18, 2007. Fermilab-Pub-07-667-E.

"First Measurement of the Fraction of Top Quark Pair Production Through Gluon-Gluon Fusion," T. Aaltonen et al., The CDF Collaboration, submitted to Phys. Rev. Lett. December 19, 2007. Fermilab-Pub-07-665-E.

"Search for New Heavy Particles Decaying to $Z^0Z^0 \to eeee$ in $p\bar{p}$ Collisions at $\sqrt{s} = 1.96$ TeV," T. Aaltonen et al., The CDF Collaboration, submitted to Phys. Rev. D January 7, 2008. Fermilab-Pub-08-008-E.

"Search for Pair Production of Scalar Top Quarks Decaying to a τ Lepton and a b Quark in $p\bar{p}$ Collisions at $\sqrt{s}$ = 1.96 TeV," T. Aaltonen et al., The CDF Collaboration, submitted to Phys. Rev. Lett. February 27, 2008. Fermilab-Pub-08-045-E. arXiv: 0802.3887.

"Search for Standard Model Higgs Boson Production in Association with a W Boson at CDF," T. Aaltonen et al., The CDF Collaboration, submitted to Phys. Rev. D March 24, 2008. Fermilab-Pub-08-070-E.

"Search for Hadronic Decays of W and Z Bosons in Photon Events in ppbar Collisions at sqrt s = 1.96 GeV," T. Aaltonen et al., The CDF Collaboration, submitted to Phys. Rev. D March 28, 2008. Fermilab-Pub-08-071-E.

"Search for Heavy, Long-Lived Neutralinos that Decay to Photons at CDF II Using Photon Timing," T. Aaltonen et al., The CDF Collaboration, submitted to Phys. Rev. D April 8, 2008. Fermilab-Pub-08-078-E. arXiv:0804.1043.

"Search for the Rare Decays $B^+ \rightarrow \mu^+\mu^- K^+$, $B^0 \rightarrow \mu^+\mu^- K^*(892)^0$, and $B_s^0 \rightarrow \mu^+\mu^-\phi$ **at CDF,"** T. Aaltonon et al., The CDF Collaboration, submitted to Phys. Rev. D Rapid Communications April 21, 2008. Fermilab-Pub-08-094-E.

"Search for the Flavor Changing Neutral Current Decay $t \rightarrow Z_q$ **in** $p\bar{p}$ **Collisions at** $\sqrt{s}$ **= 1.96 TeV,"** T. Aaltonen et al., The CDF Collaboration, submitted to Phys. Rev. Lett. May 15, 2008. Fermilab-Pub-08-128-E.

"Measurement of b-jet Shapes in Inclusive Jet Production in $p\bar{p}$ **Collisions at** $\sqrt{s}$ **= 1.96 TeV,"** T. Aaltonen et al., The CDF Collaboraton, submitted to Phys. Rev. D June 10, 2008. Fermilab-Pub-08-162-E.

FIELDS OF STUDY

Major Field: Physics

TABLE OF CONTENTS

Page

Abstract ii

Dedication iii

Acknowledgments iv

Vita vii

List of Tables xxii

List of Figures xxiv

Chapters:

1. Introduction 1

2. ElectroWeak Unification and the Higgs Mechanism 5

   2.1 ElectroWeak Unification 6
      2.1.1 Massive Bosons and the Higgs Mechanism 9
      2.1.2 SU(2) Symmetry Breaking and Standard Model Implications 12
   2.2 Grand Unification and Supersymmetry 14
   2.3 Experimental Limits and Theoretical Constraints 16
      2.3.1 Experimental Limits 17
      2.3.2 Theoretical Constraints 20
   2.4 Higgs Physics at the Tevatron 22
      2.4.1 Associative Higgs Production 23
      2.4.2 Moderate Mass Higgs Production 24
      2.4.3 Light Higgs Production 26

3. Experimental Apparatus . . . 29

3.1 The Tevatron . . . 29
3.2 The Collider Detector at Fermilab . . . 34
3.2.1 Solenoid . . . 35
3.2.2 Silicon Tracking . . . 36
3.2.3 Central Outer Tracker . . . 38
3.2.4 Calorimeters . . . 40
3.2.5 Muon Detectors . . . 42
3.2.6 Cherenkov Luminosity Counter . . . 44
3.3 Data Acquisition . . . 45
3.3.1 Level One Trigger . . . 45
3.3.2 Level Two Trigger . . . 47
3.3.3 Level Three Trigger . . . 47

4. Analysis Overview . . . 50

4.1 Event Reconstruction . . . 51
4.1.1 Electrons . . . 51
4.1.2 Muons . . . 52
4.1.3 Jets . . . 53
4.1.4 Missing Transverse Energy . . . 57
4.1.5 Secondary Vertex Identification . . . 58
4.2 Properties of Signal Processes . . . 60

5. Data Sample and Event Selection . . . 63

5.1 Event Triggers . . . 63
5.2 Cleanup of Missing E_T Data Sample . . . 64
5.3 Event Selection . . . 66
5.4 b-Tagging . . . 67

6. Modeling of Physical Processes . . . 70

6.1 Higgs Signal . . . 70

7. Backgrounds . . . 73

7.1 Monte Carlo Models . . . 73
7.1.1 Top pair production . . . 73
7.1.2 Single Top . . . 74
7.1.3 Diboson . . . 75

7.1.4 W/Z + Heavy Flavor 75
7.2 Data Driven Models 77
7.2.1 QCD Model 77
7.2.2 Mistags 78
7.3 Event Expectations 80

8. Control Regions 82

8.1 QCD Control Region and Data-Based Modeling 82
8.1.1 Shape Subtraction and Event Weighting 83
8.1.2 Estimation of Light Flavor QCD 85
8.1.3 Heavy Flavor QCD Systematic Uncertainties 87
8.2 Electroweak MC control regions 91

9. Artificial Neural Networks 96

9.1 Track Met and Track-based Neural Network 97
9.2 Artificial Neural Network Discriminant 103

10. Systematic Uncertainties 112

11. 95% Confidence Level Limits on Standard Model Higgs Production . . . 115

12. Conclusion 122

Appendices:

A. Additional Distributions 125

B. Most signal-like Higgs events 140

Bibliography 147

LIST OF TABLES

Table **Page**

1.1 *The three generations of quarks and leptons* 3

1.2 *Properties of gauge bosons in the Standard Model* 4

2.1 *Terms in the SU(2) Lagrangian representing the mass of the bosons.* 13

4.1 *Requirements for identifying electron candidates. Events with identified electrons are vetoed.* 53

4.2 *Requirements for identifying muon candidates. Additional matching requirements are imposed depending on which muon type the candidate is.* 54

5.1 *Triggers used to collect data in different periods of data acquisition* . 64

6.1 *Signal events produced in 1.7* fb^{-1} *prior to event selection or trigger efficiencies* 71

6.2 *Mean Signal event expectations in 1.7* fb^{-1} *after event selection and trigger parametrization* 71

6.3 *Selection efficiency for Higgs events in the signal region.* 72

7.1 *Quantities utilized by the Mistag Matrix* 79

7.2 *Event expectations for background processes after event selection. The difference between the total expectation and data is due to heavy flavor multi-jet QCD, which is fit to data.* 80

7.3 *Selection efficiency for various background processes.* 81

8.1 *Events accepted as well as mistag predictions in the region in which Missing E_T is aligned with the second jet.* 85

8.2 *Amount of negative tags observed in region where missing E_T is aligned with second jet. Table displays both the number events with 2 negative tags, and single tight SECVTX events in which the other jet was negatively tagged.* 87

8.3 *Electroweak MC control region defined as data passing all our cuts but also containing a high P_T muon. The uncertainties quoted on normalizations do not include JES and trigger systematics.* 93

10.1 *Change in signal efficiency for initial and final state radiation systematic samples.* 114

11.1 *Fit for QCD fraction. This shows the input backgrounds and uncertainties, and the fit values obtained from mclimit.* 116

11.2 The 95% CL limits as calculated by *mcLimit*. The numerical values give the ratio of the limit divided by the Standard Model prediction. Systematic errors are included in the calculation. The right-hand column gives the observed limit with CDF's 1.7 fb^{-1} data sample. 119

B.1 *Most signal-like events with NN output > 0.75.* 140

B.2 *Background composition of bin (bin 14) where we have our most signal-like event in tight+jet prob sample in data (run=200536, event=4538872).* 141

B.3 *Background composition of bin containing most signal-like event in Vtx+Vtx output distribution (bin 13).* 141

LIST OF FIGURES

Figure **Page**

2.1 Feynman Diagrams representing the interaction of elementary particles through the exchange of force carrying bosons 6

2.2 Examples of symmetric potentials 10

2.3 Energy Scale at which the Standard Model breaks down for particular Higgs masses 15

2.4 WW Production 18

2.5 ZH Production 19

2.6 The significance of event excess at LEP as data was collected in 2000 20

2.7 Theoretical constraints on the Higgs mass 21

2.8 Loop Diagrams involving the W boson 22

2.9 The expected production cross sections of Higgs events at the Tevatron 24

2.10 Log scale of Higgs branching ratios vs. Higgs mass 25

2.11 Example Dijet Mass distribution from a CDF $WH \rightarrow l\nu b\overline{b}$ analysis . 27

3.1 Tevatron accelerator chain 30

3.2 Side-view schematic of the CDF detector. 35

3.3 A simplistic portrayal of how particles behave within the CDF detector. 36

3.4 The CDF Run II silicon detectors 37

3.5 CDF tracking. 38

3.6 Equipotential lines in a COT cell. 39

3.7 An illustration of the electromagnetic and hadronic calorimetry in CDF. 41

3.8 Details of the CDF muon detectors 43

3.9 Graphical representation of the flow of CDF data through the trigger and DAQ system. 49

4.1 Figure illustrating a displace vertex typical of b jet decay. 60

4.2 The $ZH \rightarrow \nu\nu b\bar{b}$ and $WH \rightarrow l\nu b\bar{b}$ processes 61

7.1 Feynman diagram of top pair production at the Tevatron 73

7.2 The s-channel and t-channel single top production mechanisms. The s-channel process is more relevant in the double tag sample, as it has the same final state as WH. 74

7.3 Examples of diboson production at the Tevatron. 75

7.4 Examples of processes resulting in a vector boson plus heavy flavor quarks 76

8.1 η vs. ϕ in region where $\not\!\!E_T$ is aligned with the second jet. Instrumental regions such as the chimney and 90 degree crack show large excesses of events in the Pretag data. 83

8.2 Tagging efficiency as a function of E_T, η and number of vertices. . . . 84

8.3 Event variables in region where missing E_T is aligned with second jet. Black hashes represent the total systematic and statistical error of background model. Data consists of events with 1 tight SECVTX and 1 Jet Probability tagged jet. Upper left: Missing E_T; upper right: ΔR Lead-2nd Jet; lower left: Dot product of track and calorimeter MET; lower right: Dijet mass. 89

8.4 Event variables in region where missing E_T is aligned with second jet. Black hashes represent the total systematic and statistical error of background model. Data consists of events with 2 tight SECVTX tagged jets. Upper left: Missing E_T; upper right: ΔR Lead-2nd Jet; lower left: Dot product of track and calorimeter Met; lower right: Dijet mass. 90

8.5 Event variables in events with an identified tight muon and at least one SecVtx tagged jet.. Black Hashes represent the normalization uncertainty on all backgrounds. Upper left: Missing E_T; upper right: Dijet Mass; lower left: Dot product of track and calorimeter Met; lower right: ΔR Lead-2nd Jet 94

8.6 Agreement for pretagged electroweak MC control region. Expected background is W+l.f. and is normalized to data. Upper left: lead jet E_T; upper right: second jet E_T; lower : MET. 95

9.1 Track Met Neural Network Output from training NN to separate ZH signal from QCD background. 99

9.2 Track Met Neural Network Output for 2 different data sets. Top: Trackmet NN output for events in electroweak control region with 1 tight SecVtx tag. Bottom: Trackmet NN output for events with no leptons but with one loose SecVtx tag, and no tight tags. 100

9.3 Track Met Neural Network Output in QCD control regions for both tagging categories. Black hashes represent the total systematic and statistical error of background model. On the left is the SECVTX + Jet Prob double-tagged category, shown on the bottom with a log scale. On the right is the SecVtx + SecVtx double-tagged category, shown on a log scale on the bottom. 101

9.4 Track Met Neural Network Output for our two double-tagged signal regions. Top: SecVtx + SecVtx; bottom: SecVtx + Jet Prob. 102

9.5 Neural network shapes for Monte Carlo background processes. The x-axis represents the output of the network, with events close to 1.0 categorized as signal-like and events close to 0.0 being background-like. 105

9.6 Neural network shapes for signal and data-based background processes. The x-axis represents the output of the network, with events close to 1.0 categorized as signal-like and events close to 0.0 being background-like. 106

9.7 Figures for 1 loose tag in signal region. Error bands represent uncertainty on QCD model plus mistag uncertainty. Upper left: Missing E_T; upper right: ΔR Lead-2nd Jet; lower left: Dot product of track and calorimeter Met; lower right: Dijet Mass. 107

9.8 Figures for tight SecVtx + Jet Probability events in signal region. Error bands represent uncertainty on QCD model plus symmeterized JES uncertainty on Monte Carl backgrounds. Upper left: Missing E_T; upper right: ΔR Lead-2nd Jet; lower left: Dot product of track and calorimeter Met; lower right: Dijet Mass. 108

9.9 Figures for double tight SecVtx events in signal region. Error bands represent uncertainty on QCD model plus symmeterized JES uncertainty on Monte Carl backgrounds. Upper left: Missing E_T; upper right: ΔR Lead-2nd Jet; lower left: Dot product of track and calorimeter Met; lower right: Dijet Mass. 109

9.10 Neural Network Output in QCD control region. Black hashes represent the total systematic and statistical error of background model. Left: Double tight SecVtx tagged NN in QCD control region; Right: Tight SecVtx plus Jet Probability NN in QCD control region ; 109

9.11 Neural Network Output on log scale in QCD control region. Left: Double tight SecVtx tagged NN in QCD control region; Right: Tight SecVtx plus Jet Probability NN in QCD control region ; 110

9.12 Neural Network Output for events with tight muon. Left: NN for inclusive single tagged events with identified muon ; Right: NN for inclusive Pretag events with identified muon ; 110

9.13 NN for single loose SecVtx tagged events in signal region. 111

11.1 The N.N.D. output for Tight SecVtx plus Jet Probability tagged events. 120

11.2 The N.N.D. output for double Tight SecVtx tagged events. 120

11.3 The expected and observed limits after combining the two double tag categories. 121

12.1 The combined sensitivity to a Standard Model Higgs for both the CDF and DØ collaborations. The sensivity is displayed as the expected and observed limits over the Standard Model expectation as a function of Higgs mass. 123

A.1 Figures for 1 tight SECVTX + JP tags in region where Missing E_T is aligned with second jet. Upper left: $\Delta\phi LeadJet - MET$; upper right: $\Delta\phi SecondJet - MET$; lower left: Lead Jet η; lower right: Second Jet η.126

A.2 Figures for tight + JP tags in region where Missing E_T is aligned with second jet. Upper left: Lead Jet E_t; upper right: Second Jet E_t; lower left: Fox Wolfram Moment 1; lower right: Fox Wolfram Moment 2. . . 127

A.3 Figures for 2 tight SECVTX tags in region where Missing E_T is aligned with second jet. Upper left: $\Delta\phi LeadJet - MET$; upper right: $\Delta\phi SecondJet - MET$; lower left: Lead Jet η; lower right: Second Jet η. 128

A.4 Figures for 2 tight SECVTX tags in region where Missing E_T is aligned with second jet. Upper left: Lead Jet E_t; upper right: Second Jet E_t.; lower left: Fox Wolfram Moment 1; lower right: Fox Wolfram Moment 2.129

A.5 Figures for single tag muon data. Upper left: $\Delta\phi(MET, jet1)$; upper right: $\Delta\phi(MET, jet2)$; lower left: Lead Jet eta; lower right: Second Jet eta. 130

A.6 Figures for single tag muon data. Upper left: Lead Jet E_t; upper right: Second Jet E_t; lower left: Fox Wolfram Moment 1; lower right: Fox Wolfram Moment 2; 131

A.7 Figures for 1 loose tag in signal region. Upper left: $\Delta\phi LeadJet - MET$; upper right: $\Delta\phi SecondJet - MET$; lower left: Lead Jet η; lower right: Second Jet η. 132

A.8 Figures for 1 loose tag in signal region. Upper left: Lead Jet E_t; upper right: Second Jet E_t; lower left: Fox Wolfram Moment 1; lower right: Fox Wolfram Moment 2; 133

A.9 Figures for 1 tight SECVTX plus Jet Probability tag in signal region. Upper left: $\Delta\phi LeadJet - MET$; upper right: $\Delta\phi SecondJet - MET$; lower left: Lead Jet η; lower right: Second Jet η. 134

A.10 Figures for 1 tight SECVTX tag + Jet Probability tag in signal region. Upper left: Lead Jet E_t; upper right: Second Jet E_t; lower left: Fox Wolfram Moment 1; lower right: Fox Wolfram Moment 2; 135

A.11 Figures for 2 tight SECVTX in signal region. Upper left: $\Delta\phi LeadJet-MET$; upper right: $\Delta\phi SecondJet-MET$; lower left: Lead Jet η; lower right: Second Jet η. 136

A.12 Figures for 2 tight SECVTX tags in signal region. Upper left: Lead Jet E_t; upper right: Second Jet E_t; lower left: Fox Wolfram Moment 1; lower right: Fox Wolfram Moment 2. 137

A.13 Additional Neural Network Discriminants. Upper left: 110 GeV/c^2 2 tight SECVTX tags; upper right: 110 GeV/c^2 Tight SECVTX + Jet Probability tag; lower left: 120 GeV/c^2 2 tight SECVTX tags; lower right: 120 GeV/c^2 Tight SECVTX + Jet Probability tag. 138

A.14 Additional Neural Network Discriminants. Upper left: 130 GeV/c^2 2 tight SECVTX tags; upper right: 130 GeV/c^2 Tight SECVTX + Jet Probability tag; lower left: 140 GeV/c^2 2 tight SECVTX tags; lower right: 140 GeV/c^2 Tight SECVTX + Jet Probability tag. 139

A.15 Additional Neural Network Discriminants. Left: 150 GeV/c^2 2 tight SECVTX tags; Right: 150 GeV/c^2 Tight SECVTX + Jet Probability tag. 139

B.1 Lego display of most signal-like event. 142

B.2 COT display of most signal-like event. 143

B.3 RZ display of most signal-like event. 144

B.4 Calorimeter display of most signal-like event. 145

B.5 Trigger display of most signal-like event. 146

CHAPTER 1

INTRODUCTION

The study of science, and physics in particular, has been largely motivated by a fascination with the most extreme conditions in our universe. The motion of planetary objects were studied in detail by very early civilizations, eventually giving birth to the laws of gravitation developed by Newton. However, on a minute scale, the composition of matter was still very hazy. Philosophers in early Greece developed the idea of reducing matter until a single indivisible object was obtained. This concept was slow to develop scientifically, as a lack of technology and knowledge prevented a probing of matter on the atomic scale. Much study of the properties and classification of matter was performed in subsequent centuries, but it wasn't until Mendeleev's periodic table was formally presented in 1869 that a clear description of atoms and their basic attributes took form. However, the discovery of the electron by J.J. Thompson in 1897, and the probing of the atomic nucleus by Ernest Rutherford's gold foil experiment clearly demonstrated that matter consists of more than just the elements. Additional experimental discoveries and the mathematical formulation of theories throughout the years have given us a much more sophisticated view of the universe on the smallest of scales.

The field of particle physics is dedicated to the study of the fundamental building blocks of matter and the laws that govern them. In this field, there is nothing more sacred than the Standard Model. The Standard Model is the culmination of all research concerning the most basic structure of matter, and the current (although incomplete) answer to one of the oldest intellectual questions, "What makes up the world around us?". Immense progress in physics has been made in the last century. Each monumental experimental and theoretical discovery has helped to replace mystery with understanding, shaping the landscape of elementary particles and the ways in which they interact.

The universe as we know it consists of two types of particles called fermions and bosons, which are categorized by the intrinsic quantum property known as spin. Fermions possess a spin of 1/2, and are the elementary constituents of all matter. Fermions are further separated into objects known as quarks and leptons. There are six types of leptons, including the electrically charged electron, muon and tau particles which increase in mass respectively. Each is separated into its own generation with an electrically neutral and nearly massless neutrino as displayed in Table 1.1. While all leptons can interact through what is known as the Weak force, only those with electric charge experience the Electromagnetic force for obvious reasons. These interactions will be described in detail later in the next chapter.

Quarks, the other type of fermion, are the constituents of nuclei in atoms (protons and neutrons), as well as a vast array of shorter lived bound states known as mesons (2 quark state) and baryons (3 quark state). Like the leptons, there are six types of quarks placed into three generations of increasing mass. Additionally like the leptons, the two quarks in each generation have different charges, but consist of

Charge	Leptons		
-1	$\begin{pmatrix} electron(e) \\ \nu_e \end{pmatrix}$	$\begin{pmatrix} muon(\mu) \\ \nu_\mu \end{pmatrix}$	$\begin{pmatrix} tau(\tau) \\ \nu_\tau \end{pmatrix}$
0			
	Quarks		
$+2/3$	$\begin{pmatrix} up(u) \\ down(d) \end{pmatrix}$	$\begin{pmatrix} charm(c) \\ strange(s) \end{pmatrix}$	$\begin{pmatrix} top(t) \\ bottom(b) \end{pmatrix}$
$-1/3$			

Table 1.1: *The three generations of quarks and leptons*

the fractional charges $+\frac{2}{3}$ and $-\frac{1}{3}$. While this concept of a fractional charge seems strange initially, protons, neutrons and electrons were originally considered to all be fundamental particles with charges +1, 0, and -1 respectively. It was only later that the theory of quarks was developed, in which the proton and neutron consist of three quark bound states in which the charges add up to +1(uud) or 0(udd). Quarks can interact both Weakly and Electromagnetically like the leptons, but in addition to electric charge, quarks possess a unique charge called color. This additional charge imposes a force between quarks so great that they can only exist in bound states with other quarks, as seen in the nuclei of atoms previously referenced. This is known as the Strong interaction.

The final building block of the Standard Model are the integer spin bosons. They govern the physics of interactions between fermions, as well as themselves. The Electromagnetic, Weak and Strong force experienced by quarks and leptons are mediated by the "force-carrying" photon, W and Z particles, and gluon. The bosons generate phenomena in our universe through their interactions with matter in a number of ways. The electromagnetic force propagated by the photon produces visible light,

electricity, and radio waves to name a few. While the massless photon can travel an infinite distance, the Weak force, mediated by the W and Z bosons, is a very short range force, due to the large masses of it's mediators. The Weak force fuels the sun through nuclear fusion, producing energy in the conversion of up quarks to down quarks through the radiation of a W boson. The effects of the Weak force are seen in radioactive decay as well. The Strong force is responsible for the "particle zoo" you will come across in any particle physics book. The five lightest quarks combine with one another into a vast number of mesons and baryons, with varying degrees of lifetime. On the other hand, the top quark, a single particle with a mass nearly as great as a gold atom, decays so quickly into a bottom quark that there is no time for hadronization via the strong force. The gravitational force, the first to be understood from a classical physics perspective, has not been incorporated into the Standard Model.

Force	Bosons	Mass
Electromagnetic	photon (γ)	$0\ \frac{GeV}{c^2}$
Strong	gluons (g)	$0\ \frac{GeV}{c^2}$
Weak	$W^{\pm}$	$80.4\ \frac{GeV}{c^2}$
	Z^0	$91.2\ \frac{GeV}{c^2}$

Table 1.2: *Properties of gauge bosons in the Standard Model*

CHAPTER 2

ELECTROWEAK UNIFICATION AND THE HIGGS MECHANISM

The Standard Model and its treatment of physics in terms of elementary particles has enjoyed major success in its ability to yield an intuitive picture of fundamental processes and produce experimentally verifiable predictions. The 19th century gave rise to Maxwell's equations, which successfully unified electricity and magnetism into a single force, and the first hints of the Weak force through nuclear β-decay. However, the power and potential of these developments were truly realized when the physics of interactions began to be understood solely through the exchange of particles. These interactions are described by the construction of Feynman diagrams and the Feynman rules associated with them. For example, an interaction between an electron and a muon is mediated by the exchange of a neutral boson, also known as a neutral current. This process has both electromagnetic and weak contributions through the exchange of a γ or Z^0. Charged currents are also possible via the exchange of the weak W boson, as in the case of a muon decaying into an electron and two neutrinos. These processes are represented by their respective Feynman diagrams in Figure 2.1. It should be noted that these diagrams do not represent the kinematic motion of the particles involved, but the flow of the process. Each line and vertex yield a mathematical

contribution to the process, which can be utilized to calculate useful experimentally verifiable quantities.

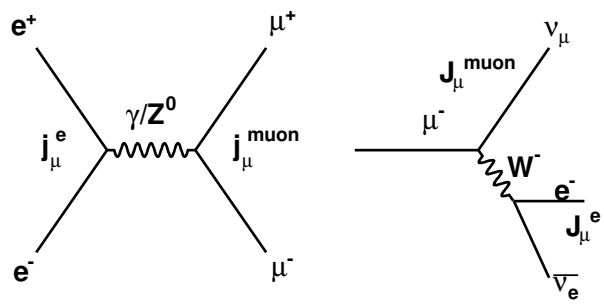

Figure 2.1: Feynman Diagrams representing the interaction of elementary particles through the exchange of force carrying bosons

2.1 ElectroWeak Unification

Quite possibly the greatest theoretical triumph of the Standard Model of particle physics has been ElectroWeak unification [1] [2]. The development of particle physics and the Standard Model led to the understanding of symmetries in weak and electromagnetic interactions. These are referred to as gauge symmetries, and utilize the currents of the interactions coupled with group theory. The foundation of the theory of Weak interactions is strongly related to that of quantum electrodynamics. The current of an electron interacting electrodynamically is constructed from it's incoming and outgoing wavefunctions, according to

$$j_\mu^{fi} = -e\overline{\Psi}_f \gamma_\mu \Psi_i \tag{2.1}$$

where $\Psi = u(p)e^{-p\cdot x}$, describing an electron with energy E and momentum p, while γ represents the Dirac γ-matrices. The invariant amplitude of an interaction mediated by the photon, such as electron-muon scattering would be given by

$$\mathcal{M} = \frac{e^2}{q^2}(j_\mu)^{e_1}(j^\mu)^{e_2} \tag{2.2}$$

from the electromagnetic currents present in the left-hand Feynman diagram of Fig 2.1, with $q = p_f - p_i$.

The theoretical construction of the Weak interaction was first devised as a way of interpreting nuclear β-decay. A number of similarities were observed between itself and muon interactions, prompting Enrico Fermi to define a new coupling constant G_F, analogous to the $\frac{e^2}{q^2}$ in the previously referenced electromagnetic interaction. The construction of the invariant amplitude in a Weak interaction proceeds in a similar fashion, with Weak currents representing the flow of particles as in the case of muon decay, illustrated in the right-hand Feynman diagram of Fig 2.1. The similarities between electromagnetic and weak interactions prove to be much more than a mere coincidence, and careful analysis of the lepton species is a starting point to ultimately unifying these interactions.

An important feature of neutrinos is the orientation of the spin quantum number in relation to its direction of motion. This is known as handedness, and only left-handed (spin angular momentum vector pointing opposite the direction of motion) neutrinos have been observed. The electron and electron neutrino can therefore be split up into a left-handed doublet and a right-handed singlet.

$$\begin{pmatrix} \nu_e \\ e^- \end{pmatrix}_L \begin{pmatrix} e^- \end{pmatrix}_R \tag{2.3}$$

Focusing on Weak currents in left-handed electron neutrino interactions, an isospin triplet consisting of the positive, negative and neutral currents (J^i_μ) can be constructed to generate an $SU(2)_L$ group

$$[T^a, T^b] = i\epsilon_{abc}T^c \tag{2.4}$$

where $T^i = \int J^i_0(x)d^3x$. While in the current form, the weak neutral current still has a right-handed component, this is avoided by including the electromagnetic current, and enlarging the group. If Q is the charge operator, generating the $U(1)_{EM}$ group, a weak hypercharge current can be introduced such that

$$Q = T^{3(NC)} + \frac{Y}{2} \qquad j^{em}_\mu = J^{3(NC)}_\mu + \frac{1}{2}j^Y_\mu \tag{2.5}$$

where Y is the weak hypercharge. There now exists an $SU(2)_L$ X $U(1)_Y$ group in which the weak and electromagnetic interactions have been unified. [1] However, just as the electromagnetic interaction is propagated by the photon, the electroweak interaction must contain couplings to vector bosons. Introducing electroweak fields W^a_μ and B_μ with isospin coupling g and hypercharge coupling $\frac{g'}{2}$, the form of the electroweak interaction is produced.

$$-ig(J^a)^\mu W^a_\mu - i\frac{g'}{2}(j^Y)^\mu B_\mu \tag{2.6}$$

The fields W^a_μ representing weak isospin and B_μ representing weak hypercharge combine to yield physically observable mass eigenstates.

$$W^\pm_\mu = \frac{W^1_\mu \pm W^2_\mu}{\sqrt{2}} \tag{2.7}$$

$$Z_\mu = -B_\mu sin\theta_W + W^3_\mu cos\theta_W \tag{2.8}$$

$$A_\mu = B_\mu cos\theta_W + W^3_\mu sin\theta_W \tag{2.9}$$

The Weinberg angle, represented by θ_W, relates the weak coupling strengths, the measurement of which by experiments at Fermilab and CERN would predict the masses of the W and Z bosons, later verified by the direct production of W and Z particles by the UA1 and UA2 experiments at CERN in 1983. The experimental validation of the predictions produced by electroweak theory make it one of the greatest triumphs in the history of physics, but there is another prediction made by the theory that has yet to be discovered experimentally. The Higgs boson has been the subject of multiple searches for over 30 years, eluding observation in every experimental effort. This new particle is a manifestation of the theories need to explain the existence of massive W and Z bosons, discussed in the following section.

2.1.1 Massive Bosons and the Higgs Mechanism

This group structure is the foundation of electroweak unification, but does not have a mechanism that can provide bosons with mass. The Standard Model requires massive Weak bosons, an experimentally verified fact. This problem was solved by Weinberg and Salaam, incorporating a spontaneous breaking of the gauge symmetry to give mass to the W and Z while leaving the photon massless. [2] The Lagrangian ($L = T - V$) formulation of the theory is invariant with respect to local gauge transformations, preserving the symmetry of the isospin and hypercharge groups. Introducing the Lagrangian [3]

$$L = (\partial_\mu \phi)^\dagger (\partial^\mu \phi) - \mu^2 \phi^\dagger \phi - \lambda (\phi^\dagger \phi)^2 \tag{2.10}$$

with complex scalar field $\phi = \frac{\phi_1 + \imath \phi_2}{\sqrt{2}}$ results in local minima for the potential at $\phi_1^2 + \phi_2^2 = \nu^2 = \frac{-\mu^2}{\lambda}$. The ν term represents the vacuum expectation value which under a the simple symmetric potential illustrated in Fig 2.2(a) has a minima at zero, which

one might naively expect. However, Fig 2.2(b) is also a symmetric potential, but with non-zero minima. The ground state is not obvious, and in fact, it is arbitrary. At this

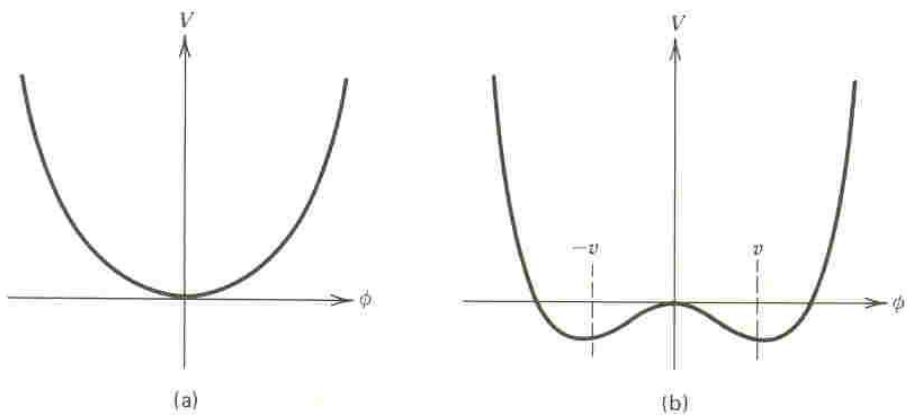

Figure 2.2: Examples of symmetric potentials

point, a spontaneous choice of ϕ is made, providing a non-zero vacuum expectation value, and the symmetry is "spontaneously broken" by the choice of a ground state. The 2-dimensional scalar field follows the same principle. Making the global gauge transformations, $\phi_1(x^\mu) = \nu + \eta(x^\mu)$ and $\phi_2(x^\mu) = \alpha(x^\mu)$, we receive the following form of the Lagrangian.

$$L = \frac{1}{2}(\partial_\mu \eta)^2 + \frac{1}{2}(\partial_\mu \alpha)^2 - \frac{1}{2}(2\lambda\nu^2)\eta^2 - \lambda\nu\eta(\eta^2 + \alpha^2) - \frac{1}{4}\lambda(\eta^2 + \alpha^2)^2 + \frac{1}{4}\lambda\nu^2 \quad (2.11)$$

The 4 latter terms represent the potential, with the η^2 term and lack of an α^2 term having very exciting and intriguing implications. These are the mass terms, with $m_\eta = \sqrt{2\lambda\nu^2}$ and $m_\alpha = 0$. The spontaneous breaking of the global symmetry has provided a massive boson, and a massless scalar boson. The massless scalar is known as a Goldstone boson, which appears whenever a symmetry is spontaneously

broken according to Goldstone's theorem. This unobserved boson is undesirable, and the theory needs a mechanism to remove it.

The breaking of a global symmetry has been performed, and techniques from Quantum Electrodynamics can now be used to make local gauge transformations. The field undergoes a gauge transformation, and the covariant derivative is introduced.

$$A_\mu \rightarrow A_\mu + \frac{1}{e}\partial_\mu \beta \tag{2.12}$$

$$\phi(x) \rightarrow \phi(x) e^{\imath\beta(x)} \tag{2.13}$$

$$D_\mu = \partial_\mu - \imath e A_\mu \tag{2.14}$$

Additionally, we can rewrite ϕ, whose $\frac{\phi_1 + i\phi_2}{\sqrt{2}}$ form has an imaginary component, in polar coordinates such that $\phi(x) = H(x)e^{\beta(x)}$. Finally, defining H relative to the vacuum expectation ν, the gauge fields and covariant derivative can be plugged into the QED Lagrangian.

$$H(x) = \frac{\nu + h(x)}{\sqrt{2}} \tag{2.15}$$

$$L = \frac{1}{2}(\partial_\mu h)^2 - \lambda\nu^2 h^2 + \frac{1}{2}e^2\nu^2 A_\mu^2 - \lambda\nu h^3 - \frac{1}{4}\lambda h^4 + \frac{1}{2}e^2 A_\mu^2 h^2 + \nu e^2 A_\mu^2 h - \frac{1}{4}F_{\mu\nu}F^{\mu\nu} \tag{2.16}$$

The breaking of the U(1) gauge symmetry is complete and studying the final Lagrangian, both an h^2 and A_μ^2 term are present. In other words, there are mass terms corresponding to a vector boson A_μ and scalar boson h of $m_A = e\nu$ and $m_h = \sqrt{2\lambda\nu^2}$. This technique is what is now known as the Higgs mechanism, introducing a new massive scalar boson into the theory. The mass terms are dependent on ν, and the non-zero value of the ground state is responsible for the massive bosons. This is not the full story however, as the process must be repeated for the SU(2) group as well.

2.1.2 SU(2) Symmetry Breaking and Standard Model Implications

The spontaneous symmetry breaking of the SU(2) isospin group follows a similar procedure, beginning with an isospin doublet of complex scalar fields where the hypercharge is +1.

$$\phi = \begin{pmatrix} \phi^+ \\ \phi^0 \end{pmatrix} = \begin{pmatrix} \phi_1 + \imath\phi_2 \\ \phi_3 + \imath\phi_4 \end{pmatrix} \tag{2.17}$$

Again, the partial derivative in the Lagrangian (eq 2.10) must be replaced by a covariant derivative. Studying the electroweak interaction in equation 2.6, the covariant derivative will take a similar form.

$$D_\mu = \partial_\mu - \imath\frac{g'}{2}YB_\mu - \imath\frac{g}{2}\tau_a W^a_\mu \tag{2.18}$$

Gauge transformations are subsequently performed as in the U(1) case, and upon adding in the familiar h(x) field, the isodoublet consists of a single neutral field.

$$\phi(x) = \begin{pmatrix} \phi^+ \\ \phi^0 \end{pmatrix} = \begin{pmatrix} 0 \\ \frac{\nu + h(x)}{\sqrt{2}} \end{pmatrix} \tag{2.19}$$

Substitution of the covariant derivative and gauge transformed potential into the Lagrangian yields a large number of terms which correspond to different interactions of the fields (i.e vertices in the Feynman formulation). However, the most striking terms represent the W and Z vector bosons.

By requiring that the photon be massless, it can be shown that the spontaneous breaking of the symmetry yields massive vector bosons as well as a massive Higgs scalar boson.

In fact, the Higgs field can be utilized within Standard Model theory to provide mass to all fermions as well. The Higgs field couples to mass, and it can be shown that the mass of all fundamental particles is related to the vacuum expectation value.

Boson	Mass Term	Mass
$W^{\pm}$	$\frac{1}{8}(\nu g)^2(W_1^{\mu}+\imath W_2^{\mu})(W_{1\mu}-\imath W_{2\mu})=(\frac{\nu g}{2})^2 W^{+\mu}W_{\mu}^{-}$	$m_W=\frac{\nu g}{2}$
Z^0	$\frac{\nu^2}{8}(g'B^{\mu}-gW_3^{\mu})(g'B_{\mu}-gW_{3\mu})=\frac{1}{2}(\frac{\nu}{2}\sqrt{g^2+g'^2})^2 Z^{\mu}Z_{\mu}$	$m_Z=\frac{\nu}{2}\sqrt{g^2+g'^2}$
γ^0	None!	$m_{\gamma}=0$

Table 2.1: *Terms in the SU(2) Lagrangian representing the mass of the bosons.*

However, this cannot be used to predict the masses of the fermions, because the magnitude of the coupling term is unique and arbitrary for each fermion in the context of the Standard Model theory.

$$m_e=\frac{1}{\sqrt{2}}g_e\nu \qquad m_u=\frac{1}{\sqrt{2}}g_u\nu \qquad m_d=\frac{1}{\sqrt{2}}g_d\nu \tag{2.20}$$

However, this is not the case with the W and Z bosons. The couplings in electroweak theory are related by the Weinberg angle mentioned in section 2.1, which is an experimentally observable quantity. Measurements have yielded a value of ν=246 GeV.

$$tan\theta_W=\frac{g'}{g} \qquad cos\theta_W=\frac{m_W}{m_Z} \tag{2.21}$$

High-energy neutrino beam experiments at CERN and Fermilab first determined the Weinberg angle, which was used to calculate both the mass of the Z and the W. These Weak bosons were later directly produced by colliding beam experiments, verifying the predictions of the Standard Model. There is, however, one piece of Electroweak theory that has eluded experimental observation. The Higgs boson, which was introduced as a result of the broken symmetry, should exist as an observable if

the Higgs mechanism is correct. However, the mass of the Higgs cannot be determined theoretically. Its mass is determined by its self-coupling to the Higgs field, and therefore can only be measured.

2.2 Grand Unification and Supersymmetry

Electroweak unification and the Standard Model have had great success in predicting future physics and in describing the subatomic world. However, it is far from a complete description of all physics. There is no mechanism with which to unify the electroweak and strong forces, and gravity is excluded entirely. Theories which propose to unify the electroweak and strong forces are called Grand Unified Theories (GUT). While many of the ideas and details of these theories are outside the scope of this discussion, it is worthwhile to discuss how Grand Unification affects the Higgs mechanism. In the simplest example of a GUT, the $SU(3)_{color} \times SU(2) \times U(1)$ group structure is unified into a single SU(5) group. Below some large energy scale, this SU(5) symmetry is broken, leaving us with the Standard Model group structure. In the Standard Model, there are couplings associated with each group that determine the strength of interactions. Grand Unification proposes to merge these couplings at energies of the order 10^{16} GeV. This concept, while enticing, brings about problems of it's own. For the Standard Model to be valid, certain constraints are implemented on the possible range of Higgs masses. These constraints are calculated from theory, using the experimentally determined masses of electroweak force carriers as inputs, as well as the mass of the top quark. Assuming a top mass of 175 GeV/c^2, Figure 2.3 [4], displays a range of possible cutoff energies where the Standard Model breaks down and other physical theories must take its place for a particular Higgs mass.

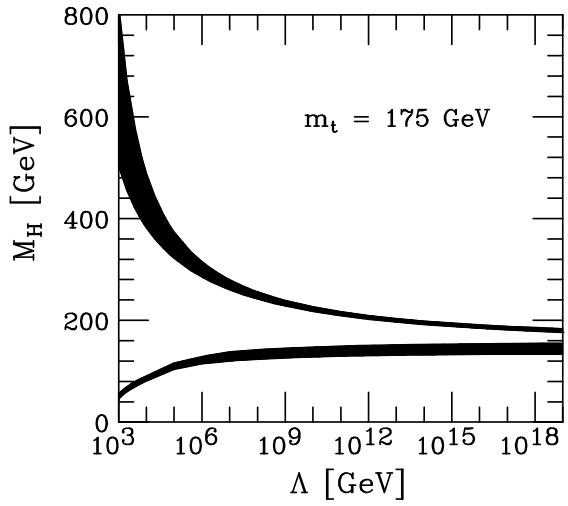

Figure 2.3: Energy Scale at which the Standard Model breaks down for particular Higgs masses

In order for a theory to make physical sense, it must be renormalizable. Since virtually all theories cannot be constructed exactly, perturbation theory is relied upon to add higher order corrections to theories. If a theory is not renormalizable, infinities are introduced and it becomes invalid. As Figure 2.3 demonstrates, the value of the Higgs mass in the context of the Standard Model must be much less than the energy region proposed in a GUT. In fact, any Higgs mass larger than about 1 TeV leads to the violation of unitarity with probabilities exceeding 1, which clearly cannot be the case in any true physical model. For the Standard Model to remain renormalizable, and to be valid at the energy scale of Grand Unification, the theory begins to become impossible to maintain, as the calculation of radiative corrections become increasingly difficult and unlikely to be able to salvage the model. This is what is known as the gauge hierarchy problem, and is one of the primary reasons

to believe that the Standard Model is just a low-energy sub-set of a larger theory. One of the most discussed of these larger theories is referred to as Supersymmetry. Supersymmetry attempts to unify the Strong and Electroweak forces by introducing a superpartner for every Standard Model fermion and boson. These new particles are much more massive than their standard model partners. The partner of a fermion will be a supersymmetric boson and vice-versa. [5] These new particles are introduced in order to expand on the experimentally verified low-energy Standard Model and allow for Grand Unification of the Electroweak and Strong couplings at an extremely large energy scale. A necessity in supersymmetry, in addition to the new superpartners, is the introduction of multiple Higgs scalars. [6] Focusing on the Minimal SuperSymmetric Model(MSSM), there are predicted to be five Higgs particles. These include the charged H^+ and H^- as well as the neutral scalars H, A and h. The Higgs scalar h is expected to be of lower mass than the others, and behaves in a similar fashion to that of the Standard Model Higgs boson.

2.3 Experimental Limits and Theoretical Constraints

Much work has been put into the search for the Higgs boson. While all previous attempts to detect the signature of a physical process involving the Higgs have been unsuccessful, the results of these experiments are invaluable to all future searches. In the early 1970's, electroweak theory was still in need of experimental validation. While interactions involving the W had been indirectly observed, the predicted Z neutral current had not. The Gargamelle bubble chamber at CERN first observed the Weak neutral current in 1973, giving experimental validation to the theorized Z. Soon thereafter, measurements of the Weinberg angle at CERN and Fermilab predicted the

W mass to be about 80 GeV/c^2 and the Z to be slightly higher, at about 90 GeV/c^2. They were later directly produced at CERN in the SPS proton anti-proton collider, being detected and measured by the UA1 and UA2 experiments. The next generation of colliding beam accelerators were being built at this time, hoping to to uncover the final pieces of the Standard Model and anything beyond. Hope was high that the Higgs boson would be discovered, offering yet another experimental validation of electroweak unification.

2.3.1 Experimental Limits

The construction and operation of the Large Electron Positron Collider(LEP) at CERN [7] and of the Tevatron at Fermilab [8] have produced many measurements of electroweak phenomena as well as other physical processes. Measurements of the Z mass, as well as increasingly precise measurements of the top quark and W mass are used within Standard Model theory to predict the most probable mass region for the Higgs. LEP began colliding electrons and positrons in 1989 at a center of mass energy equal to that of the Z boson. The beams were accelerated around a large circular ring, colliding at 4 specific locations where the products of the collisions could be measured by the L3, OPAL, DELPHI and ALEPH detectors. The first run, known as LEP1, ran from 1989-1995 and directly produced millions of Z events. It should be noted that the SLD experiment at the SLAC linear e^+e^- collider has also played a significant role in the measurement of the Z mass, as well as the Weak mixing angle $\sin^2\theta_W$. These results have been combined to form an incredibly precise current value of m_Z=91.1875 $\pm$ .0021 GeV/c^2. [9] In the meantime the CDF and D0 collaborations at the Tevatron had collected enough data from proton anti-proton

collisions to announce the discovery of the top quark in 1995 at an unprecedented mass of about 175 GeV/c^2 [10] [11]. LEP began operation again in 1995 with enhanced energy capabilities. LEP2 as it is called, started collecting data at $\sqrt{s} = 2M_W$, producing a highly accurate measurement of the W mass, utilizing the mechanisms shown in Figure 2.4.

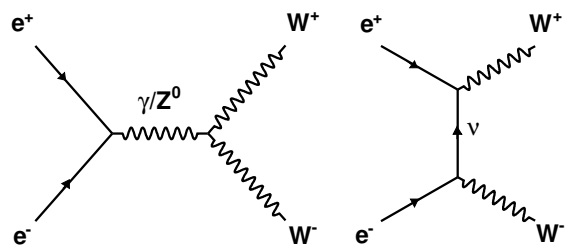

Figure 2.4: WW Production

With the latest measurements of the Z, W and top, it became increasingly probable that the Standard Model preferred a low mass Higgs. Since the Higgs mass is unknown due to it's self-coupling, LEP2 had large mass regions to cover. The production channel with the most likely chance of success was believed to be the production of an off-mass shell Z, immediately radiating a Higgs as shown in Figure 2.5.

If $\sqrt{s} = M_Z + M_h$, an excess of events consistent with the production of Higgs would be seen. While the Z may decay a number of ways including a quark anti-quark pair, a di-lepton pair (e$^+$e$^-$,$\mu^+\mu^-$,$\tau^+\tau^-$), or two neutrinos, a low-mass Higgs ($<$ 135 GeV/c^2) is expected to decay to a $b\bar{b}$ pair most of the time. [12] LEP2 scanned across energy regions above the Z mass in the hope that a signal would be observed. For example, one of the most powerful channels involves the Z$\rightarrow$ $\nu\nu$ process. This

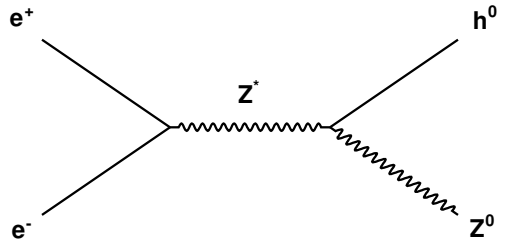

Figure 2.5: ZH Production

process has a distinctive feature of two boosted b-jets and a large energy imbalance from the invisible neutrinos. The energy and momentum of the b-jets can then be used to reconstruct the Higgs boson from which they decayed. Physicists at all 4 LEP experiments analyzed data using novel techniques, continuing to place more strict limits on the mass of the Higgs. In mid-2000, no evidence of Higgs production had been observed and construction of the Large Hadron Collider(LHC) was scheduled to begin later that year.

In the final energy region explored by LEP, an excess of events began to develop consistent with ZH production at $M_H \approx 115$ GeV/c^2 [13]. Unfortunately, time had run out for LEP, and despite pleas for extended running times to study the excess in detail, LEP was permanently shut down and construction of the LHC begun. Analysis of data from ALEPH, DELPHI, L3, and OPAL led to a final lower mass limit of 114.4 GeV/c^2. In fact, the expected limit in the absence of a signal was calculated to be 115.3 GeV/c^2, but was lowered by the excess of events observed, mostly by the ALEPH collaboration. [14] No firm experimental limit had been placed on the Higgs mass before LEP, and none has been placed since then. Using LEP as a guide, it is up

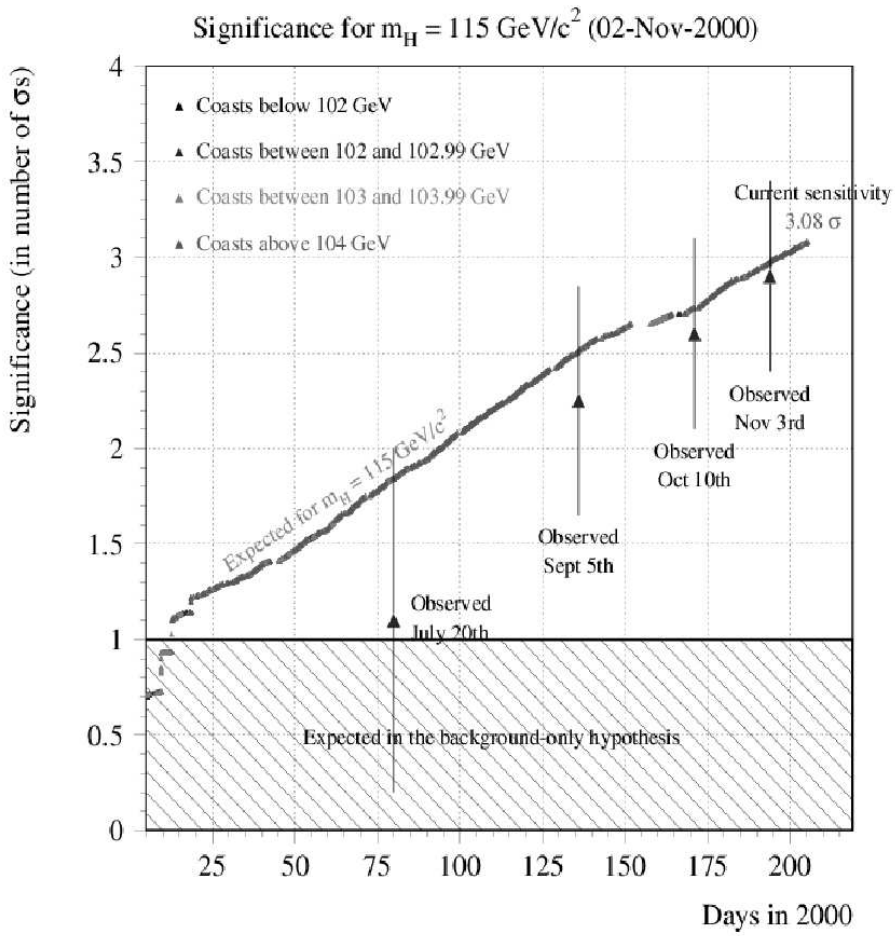

Figure 2.6: The significance of event excess at LEP as data was collected in 2000

to the current and future generation of accelerators, detectors and particle physicists to continue the search, and finally find or eliminate the elusive Higgs boson.

2.3.2 Theoretical Constraints

While LEP has placed an lower limit on the Higgs mass, no experiment as of now has been able to collect the data required to place an upper limit. However, measurements of the W and top mass continue to decrease in uncertainty through

the use of increased statistics and refined analysis techniques by the D0 and CDF collaborations. These latest results as seen in Figure 2.7, have increasingly constrained the most likely mass region of a Standard Model Higgs boson. The masses of Weak bosons receive corrections in the form of loop diagrams. A W or Z can momentarily break into a fermion anti-fermion pair. The top quark, being the most massive fermion by far, dominates these corrections. In addition, a weak boson can break into a loop with itself and a Higgs. The loop diagram indicates that the less massive the W is, the

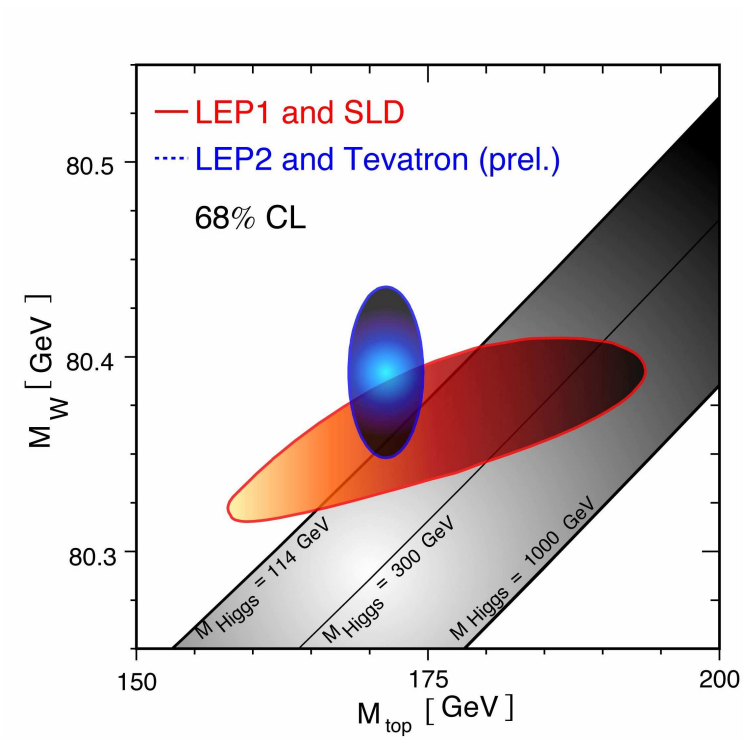

Figure 2.7: Theoretical constraints on the Higgs mass

more likely it is that the Higgs has large mass. Therefore, more precise measurements of the W and top lead to tighter constraints on the probable mass of the Higgs in

the context of the Standard Model. Recent measurements of the W and top have pulled theoretical constraints lower in mass with increased probability, enhancing the intriguing thought that perhaps the excess of events at LEP was more than an aberration. With the Tevatron running better than ever and the construction and commissioning of the LHC nearing completion, we can look to the near future of particle physics with optimism and excitement.

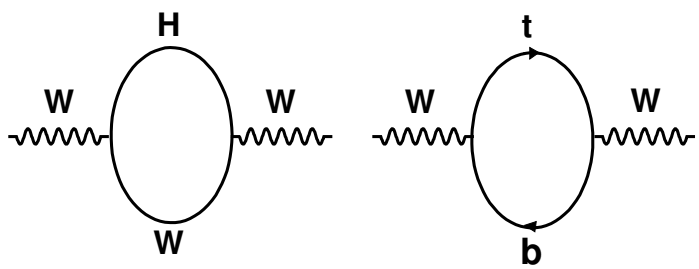

Figure 2.8: Loop Diagrams involving the W boson

2.4 Higgs Physics at the Tevatron

While most of the physics community looks to the LHC as the future of Higgs physics, and deservedly so, members of the D0 and CDF community are attempting to catch everyone off-guard by discovering a Standard Model Higgs. Although the amount of data projected to be collected at the LHC will dwarf that of the Tevatron, there are some advantages to be had at a $p\overline{p}$ collider like the Tevatron, particularly for a low-mass Higgs scalar. The quality of data accumulated has been excellent, and physicists are developing new analysis techniques based on the actual performance

of the detectors and past experience with Higgs physics at CDF and D0. The LHC is scheduled to begin operation in late 2008, so the time is now for the Tevatron to make enough improvements as to become sensitive to the Higgs.

2.4.1 Associative Higgs Production

Higgs production at the Tevatron is expected to occur a number of ways as displayed in Figure 2.9. This figure displays the production cross-section of the three primary Higgs production mechanisms at the Tevatron as a function of the Higgs mass. The cross-section is a measure of the probability that a particular physical process will occur, given the center of mass energy of the interacting particles. Although gluon fusion(gg→H) produces Higgs events at a substantially larger rate than all other processes, the amount of QCD background in this particular channel is much too great for there to be any hope of isolating a signal for low Higgs masses. Backgrounds are events that look very similar to a process of interest(signal) making it more difficult, or in some cases impossible, to study. Therefore, Higgs physics at the Tevatron utilizes the production of a vector boson in association with a Higgs. While the expected number of events is much less than that of gluon fusion, vector bosons decay leptonically a certain fraction of the time, leaving behind unique features such as isolated high-energy tracks and/or large deposits of energy in the calorimeters or muon chambers. In addition neutrinos, which are invisible to the detector, can be produced. Under this scenario, there will be a large energy imbalance in the direction transverse to the beamline. These features are used to define datasets of events consistent with the leptonic decay of a W or Z, which largely reduces the number of uninteresting events that can easily overwhelm a signal.

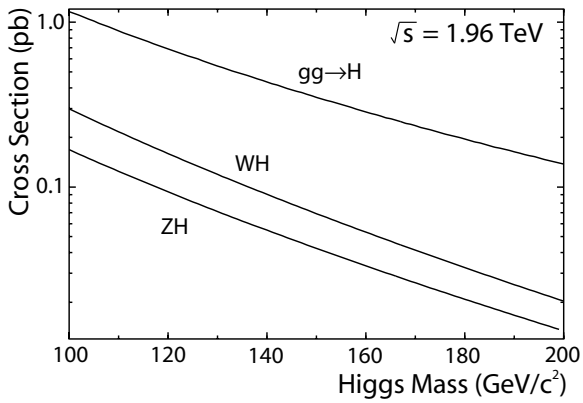

Figure 2.9: The expected production cross sections of Higgs events at the Tevatron

In addition to the primary production mechanism, Higgs analysis is also defined by the manner in which the Higgs is expected to decay. Figure 2.10 displays the decay rates as a function of the Higgs mass. For Higgs masses less than about 135 GeV/c^2, the primary decay products will be a $b\bar{b}$ pair. Above this mass, WW decay begins to dominate. Regions above 200 GeV/c^2 suffer from extremely low production rates and are not considered in Higgs analysis at the Tevatron at this time.

2.4.2 Moderate Mass Higgs Production

A Higgs boson above $\approx$ 135 GeV/c^2 will decay primarily to a pair of W's. Higgs bosons produced by gluon fusion, unable to be used in a $H \rightarrow b\bar{b}$ analysis due to enormous irreducible backgrounds, can be utilized in a higher mass analysis when both W's are required to decay leptonically. In this analysis, 2 oppositely charged leptons are required, in addition to missing energy from the neutrinos. The major background is diboson WW production because it is difficult to select a set of cuts that remove these events without losing signal. Other backgrounds such as Drell-Yan $\gamma \rightarrow l^+l^-$

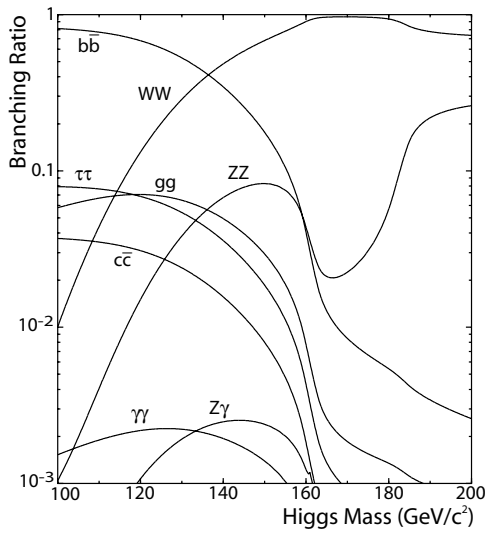

Figure 2.10: Log scale of Higgs branching ratios vs. Higgs mass

production and $t\bar{t}$ events play a smaller role in this analysis. Another analysis that can play a smaller role for a moderately massive Higgs boson involves WH production where the Higgs decays to WW. If all W's are required to decay leptonically, the final state of $l^+l^-l^\pm\nu\nu\nu$ is a very distinct signal with small backgrounds. However, this process only occurs a small fraction of the time, and will be difficult to identify with the amount of data that the Tevatron is projected to collect. Another option involves requiring two leptons with identical charge in addition to two jets. W bosons decay to quarks more often than they do leptonically, and requiring like-signed leptons removes many backgrounds that must decay to oppositely charged leptons. This will occur more often than the tri-lepton process, but still suffers from a very low event rate. In the mass region around 160 GeV/c^2, where the $H \rightarrow WW$ branching ratio peaks, there is a large sensitivity to a Higgs signal. Through the combination of these analyses from both experiments, the Tevatron should be able to exclude Higgs masses

in this mass range at the 95% CL if there is no signal present. It is believed that this can be done with less than the entire projected dataset of 8 fb^{-1} per experiment.

2.4.3 Light Higgs Production

A Standard Model Higgs boson with mass less than 135 GeV/c^2 is expected to decay to a $b\bar{b}$ pair a majority of the time. The b-quark decay products will proceed to fragment into a spray of particles called a jet, which is then measured by the detector. However, there are many other processes that could yield a similar final state. Higgs analyses are difficult in the absence of large integrated luminosity (amount of data accumulated) due to the number of processes that mimic a Higgs signal. In this mass region, Higgs studies are split into three main analyses. All require two jets that can be reconstructed to form the mass of the Higgs.

- The $ZH \rightarrow llb\bar{b}$ analysis requires either an e^+e^- pair or a $\mu^+\mu^-$ pair that form the mass of the Z. While this is a particularly "clean" search region with no high-energy neutrinos in the signal final state and many distinguishing features, it suffers from a low cross section times branching ratio when compared to other Higgs search channels.

- The $WH \rightarrow l\nu b\bar{b}$ channel searches for events with an e or μ lepton and an imbalance in transverse energy from the neutrino. WH production has a larger cross section than ZH, but the signal to background ratio is worse in this channel.

- The $ZH \rightarrow \nu\nu b\bar{b}$ analysis studies events with a large imbalance of energy in the transverse direction due to unmeasurable neutrinos and no identifiable leptons. In addition, there is a significant enhancement in signal from WH production where the lepton in the event fails to be detected.

The event selection for all of these analyses are orthogonal and results can be combined to produce an overall sensitivity to a Higgs signal at masses between 110-150 GeV/c^2. In addition, due to the limited amount of data projected to be collected by each experiment at the Tevatron, CDF and D0 have proposed to combine results, essentially doubling the statistical power of each analysis. However, even with all of these enhancements to signal sensitivity, extracting the Higgs amongst large backgrounds will be difficult. The standard technique used bu analyses such as these involves cutting out events by requiring certain thresholds in kinematic and topological variables, optimizing the number of expected signal events over the square root of background events ($\frac{S}{\sqrt{B}}$). A dijet mass is then reconstructed from two jets in the event, and that distribution is fitted in an attempt to isolate a signal. This

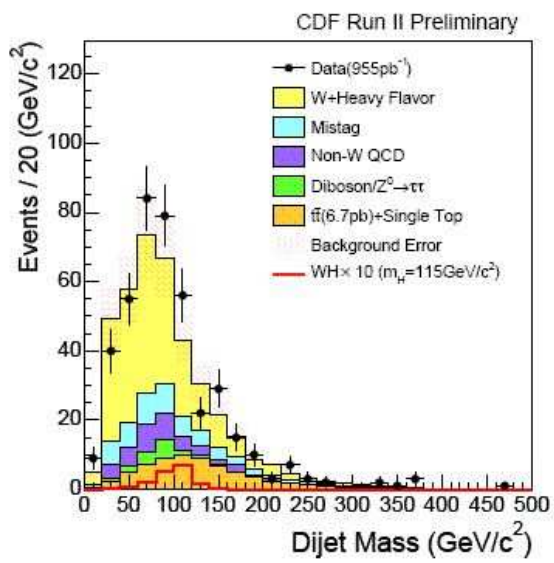

Figure 2.11: Example Dijet Mass distribution from a CDF $WH \rightarrow l\nu b\overline{b}$ analysis

method is beneficial in that a well understood quantity with a strong intuitive appeal is being fit. However, the current reconstructed dijet mass resolution of the Higgs is inferior to what physicists at the Tevatron had hoped to achieve. This, in addition to the need for increased b-tagging efficiencies and other factors, have led CDF and D0 to design new analysis techniques that hope to improve signal acceptance and background rejection. The development of such techniques is a primary focus of this dissertation, and are described in detail in chapter 9.

CHAPTER 3

EXPERIMENTAL APPARATUS

As of today, experimental study of physics concerned with the Higgs Boson is restricted to the CDF and DØ collaborations at Fermilab. Assuming the experimental lower limit of 114.4 GeV/c^2 set by LEP, only the proton-antiproton beams provided by the Tevatron can provide enough center of mass energy to produce the Higgs Boson. The Collider Detector at Fermilab consists of many subdetectors, each with components specifically engineered to provide useful information pertaining to the physics of proton-antiproton collisions. The beams provided by the Tevatron in conjunction with CDF have provided an astounding environment to probe new and exciting physics at its most fundamental level.

3.1 The Tevatron

Until the first collisions take place in the Large Hadron Collider at CERN, the Tevatron [8] at Fermilab remains the most energetic particle accelerator in the world. Two beams are accelerated to a final energy of 0.98 TeV, one of which consists of entirely of protons, the other of its antimatter twin the antiproton. These beams circulate around the Tevatron in opposite directions, colliding with a center of mass

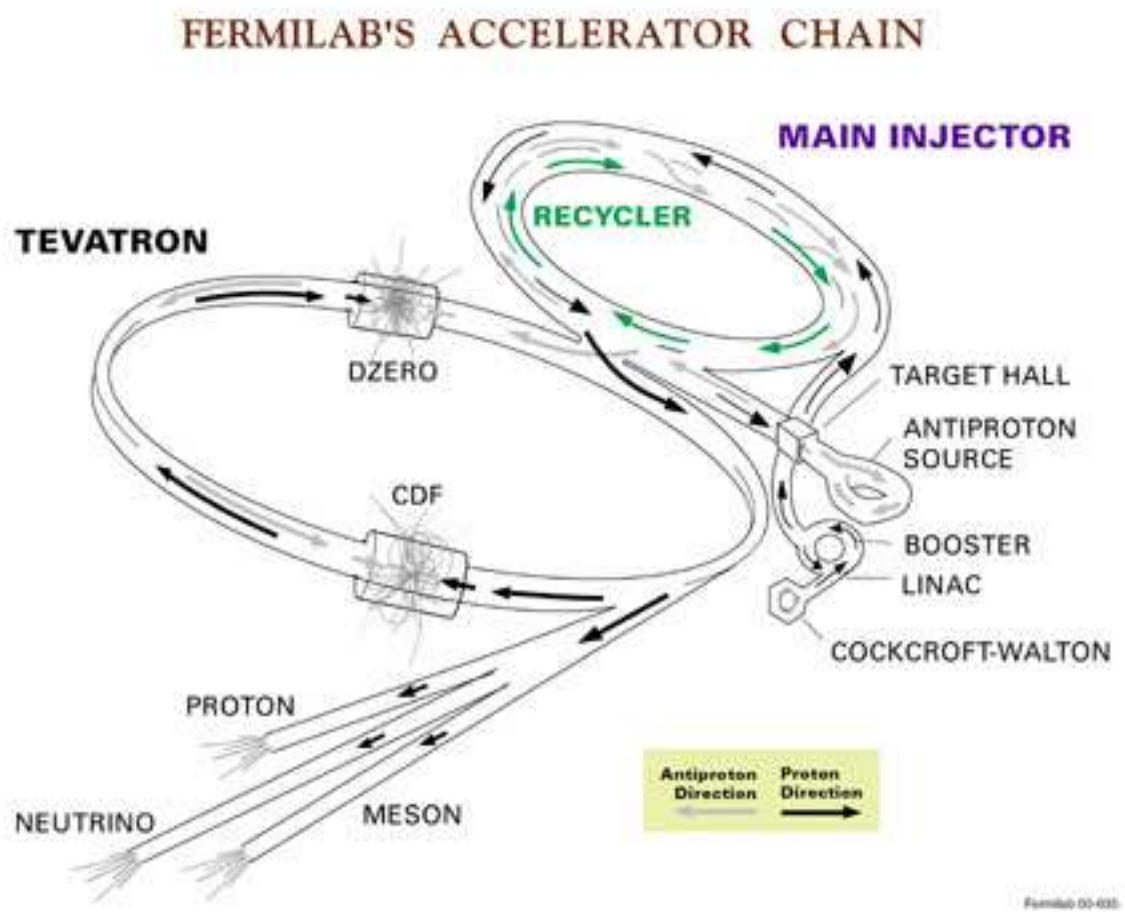

Figure 3.1: Tevatron accelerator chain. A sketch of the accelerator chain used at the Fermi National Accelerator Laboratory. Contained is the chain that leads to collisions at CDF.

energy of 1.96 TeV at two interaction points, surrounded by the CDF and DØ detectors. The process of generating the highly energetic beams of the Tevatron is a multi-stage process, encompassing the creation of a focused proton beam, the production of antiprotons, and 5 separate accelerators.

The process of producing beams in the Tevatron begins by creating Hydrogen ions. H^- is created from H_2 gas, by attracting the nucleus towards a metal surface

with an electric field. The hydrogen then picks up electrons from plasma near the surface of the metal. The now negatively charged ions are brought to 750 keV by traveling through an electrically static Cockroft-Walton accelerator, and are guided to the Linac for further acceleration.

The Linac is a linear accelerator, which utilizes a radio frequency (RF) electromagnetic field, as static electromagnetic fields cannot be sustained and will break down when attempting to accelerate the ions to high energies. The RF electromagnetic field generated by alternating current will provide the ions with a series of accelerating boosts while traveling the length of the 150 meter Linac, reaching an energy of 400 MeV. While a RF field provides a solution to the problems cited for static direct current fields, the ions must now be guarded from the RF field as they enter a region in phase that would provide a counteractive force. Drift tubes are utilized to accomplish this, and must be spaced appropriately to accommodate increases in velocity. The oscillating field will not only pump energy into the ions, but group them into bunches separated by the stable phase region in the field called a bucket. Before being transferred to the third link in the accelerator chain, the ions are passed through carbon foil, which strips the Hydrogen of its electrons producing the bare protons needed for the final three apparatuses.

While the previous increases in energy have been administered via linear acceleration, a different approach is more suitable for creating the enormous energies the Tevatron will ultimately possess. Continuing to provide more and more energy to protons linearly would require an unrealistically long accelerator. To address this problem, all latter stages use circular synchotrons to accelerate the proton nuclei.

Therefore, the same path can be used continuously as protons travel the circumference of a ring. Synchotrons must synchronize the electric field accelerating the protons with a magnetic field which curve the trajectory of the protons around a ring. The Booster is such an accelerator, which brings the protons up to an energy of 8 GeV during a series of thousands of rotations. The oscillation frequency of the electric field is continually increased to coincide with the accelerating velocity of the protons, which results in the ability to reuse the same beam pipe multiple times. This design is also utilized by the final two accelerating rings, but with even greater energies.

Increasing the proton energy even further requires the use of a larger ring. Therefore, the 8 GeV protons are sent to the Main Injector which at 3.3 km, is about 7 times the circumference of the Booster. Here the protons are brought up at an energy of 120 GeV for the purpose of manufacturing antiprotons. The beam is sent to the antiproton source, producing a number of byproducts which result from the high energy collision of protons with a nickel target, including antiprotons. Antiprotons are separated from other particles by a magnetic field, which bend the negatively charged baryons, selecting those with 8 GeV of energy. This process is easily the limiting factor in the production of beams for use in the Tevatron, as approximately 1 or 2 antiprotons will be collected for every 100,000 protons sent to the target. The antiprotons which are collected are sent to the Debuncher for cooling and to reduce momentum spread, then to the Accumulator to stack multiple pulses from the Debuncher, and finally, when a sufficient amount of antiprotons have been stored, the bunch proceeds to the Main Injector where the original incoming protons were sent

from. Here both protons and antiprotons are brought to an energy of 150 GeV, taking advantage of the same accelerating system but traveling in opposite directions, a convenient property of their identical mass and opposite charge.

Proton and antiproton bunches are then injected into the Tevatron. The Tevatron is larger than the Main Injector with a circumference of 6.3 kilometers, and makes use of a system of superconducting magnets to maintain the enormous energies provided. The magnets in the Tevatron are a niobium/titanium alloy kept at extremely cold temperatures ($\approx 4K$) required for superconductivity. A dipole setup is utilized to steer beam around the ring of the Tevatron, while a magnetic quadrupole structure focuses the beam to prevent a degrade in luminosity or loss of the beam entirely. The final energy of each beam in the Tevatron is 980 GeV, corresponding to a center of mass energy of 1.96 TeV. Once a fully prepared beam is ready, the Tevatron initiates collisions at two points where the CDF and DØ detectors are located. The beams are steered towards one another at these two points, and cross paths at the center of a detector where the collision(s) is analyzed by the detector in question.

While much of the long acceleration chain is geared towards ramping up beam energy, of great importance is the ability to produce large luminosities. Major upgrades were designed and implemented with respect to Run I of the Tevatron, greatly increasing the ability to produce large datasets. Run II of the Tevatron boasts greater collision frequency and more proton-antiproton bunches in addition to the increase in energy. The Tevatron operates with 3 trains of protons and antiprotons, each containing 12 bunches spaced by 396 ns intervals. Gaps between the trains allow for ample time to abort a beam without causing damage to the Tevatron or the detectors. Greater instantaneous luminosities enhance the probability of a proton-antiproton

collision, and increase the potential datasets for the detectors when integrated over time. Over the course of Run II, more and more protons and antiprotons have been successfully packed into bunches, continually increasing the rate of data acquisition for the experiments with record luminosities for a hadron collider.

3.2 The Collider Detector at Fermilab

The Collider Detector at Fermilab [15] is a collection of many sub-detectors working together to extract as much information as possible from the collisions occurring at the interaction point it surrounds. Each component of CDF is designed and located so as to maximize the ability to measure specific properties of interesting physics in high quality collisions. For instance, the silicon detectors are located closest to the beamline, and is placed directly on the beampipe to extract high-precision tracking measurements needed to understand physics occurring shortly after the primary interaction. The Muon detectors on the other hand are placed outside of the calorimeters so as to only measure long-lived, weakly interacting charged particles escaping the rest of CDF, and only require lower precision tracking. They need only to locate a single short track which points back to more sophisticated tracking, and are designed accordingly. All pieces of CDF are utilized in locating and reconstructing the most interesting proton-antiproton collisions, allowing the analyzers to probe new physics and produce high quality measurements of physical phenomena. All components are essentially symmetric in the plane transverse to the beamline, but change with respect to how central (closest to primary point of interaction) or forward they are located.

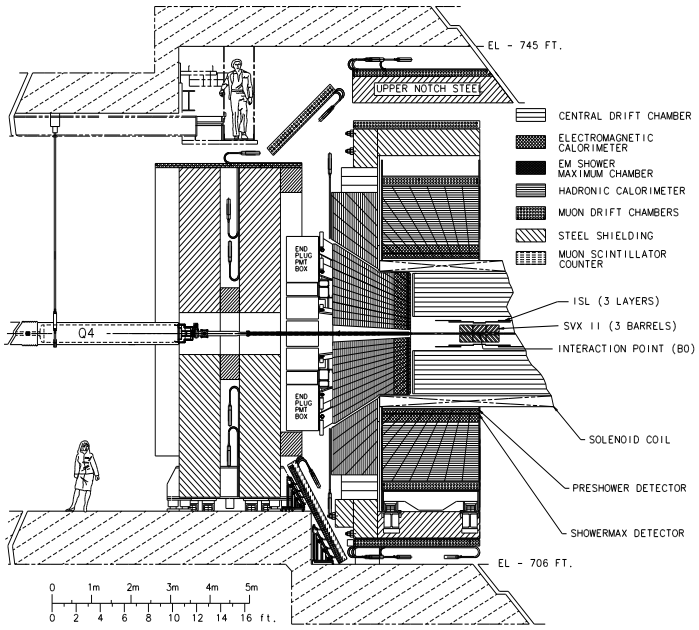

Figure 3.2: Side-view schematic of the CDF detector.

3.2.1 Solenoid

To accurately reconstruct the momenta of charged particles with CDF's tracking, it is necessary to apply a strong magnetic field to bend the trajectory of the high energy particles expected. This is accomplished with a 5m long superconducting solenoid positioned outside of the CDF tracking detectors. Wrapping around the radius of the outer tracking chamber, the solenoid produces a uniform 1.4 Tesla magnetic field parallel to the beamline. Charged particles produced in a proton-antiproton collision will bend orthogonally to the field as they traverse CDF's tracking, producing a curvature to their trajectory which is directly related to the momentum of the reconstructed track. Additionally, it is possible to determine the charge of the particle by the direction of the curvature in the magnetic field.

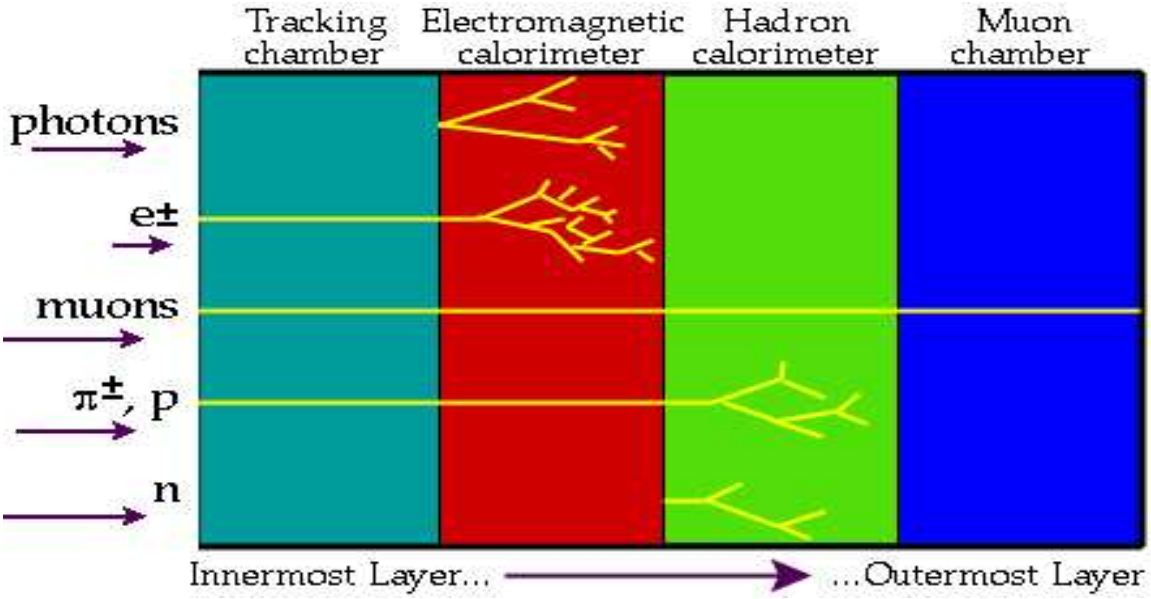

Figure 3.3: A simplistic portrayal of how particles behave within the CDF detector.

3.2.2 Silicon Tracking

Placed directly on the beam pipe, closest to the aftermath of a proton-antiproton collision are the silicon detectors. The silicon detector [16] is divided into three layered sub-systems. Layer00 is the first sub-system, with the innermost layer positioned at a radial distance of 1.35 cm around the beampipe. This layer must withstand the greatest amount of radiation of any part of the detector, and is comprised of single sided silicon wafers designed to tolerate the large bias voltages necessary. Layer 00 allows for enhanced resolution on the impact parameter associated with collisions, and offers a layer of protection for the second silicon sub-system.

The SVX II is comprised of 5 layers of double-sided silicon. In each layer, one side is axial, aligned to offer radial and transverse tracking information (r-ϕ), while the

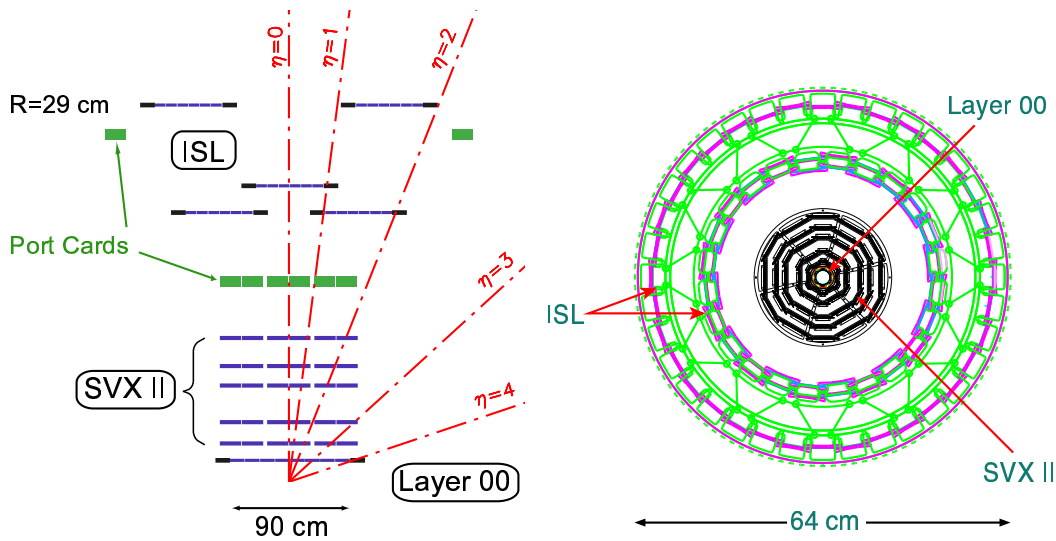

Figure 3.4: The CDF Run II silicon detectors. On the left is a side view of half of the CDF Run II silicon detectors on a scale in which the z coordinate is highly compressed. On the right is an end view.

other side is stereo, aligned to offer additional information related to the momentum of tracks in the z-direction (parallel to the beam). This is accomplished by positioning the silicon at a 90 deg angle to the axial side for layers 1,2 and 4, and at a 2 deg stereo angle for layers 3 and 5. The 5 layers extend from 2.4 cm away from the beam, out to 10.7 cm, and offer lengthwise tracking out to $|\eta| < 2.4$

The outermost silicon detector is the Intermediate Silicon Layer (ISL) [17], providing additional tracking between the SVX II and the Central Outer Tracker (COT). The ISL occupies the radial area of 20 to 28 cm from the beamline, and consists of two double-sided layers of silicon. The first layer extends out to $|\eta| < 1.0$, while the second offers tracking out to $|\eta| < 2.0$. The entire silicon system offers precise

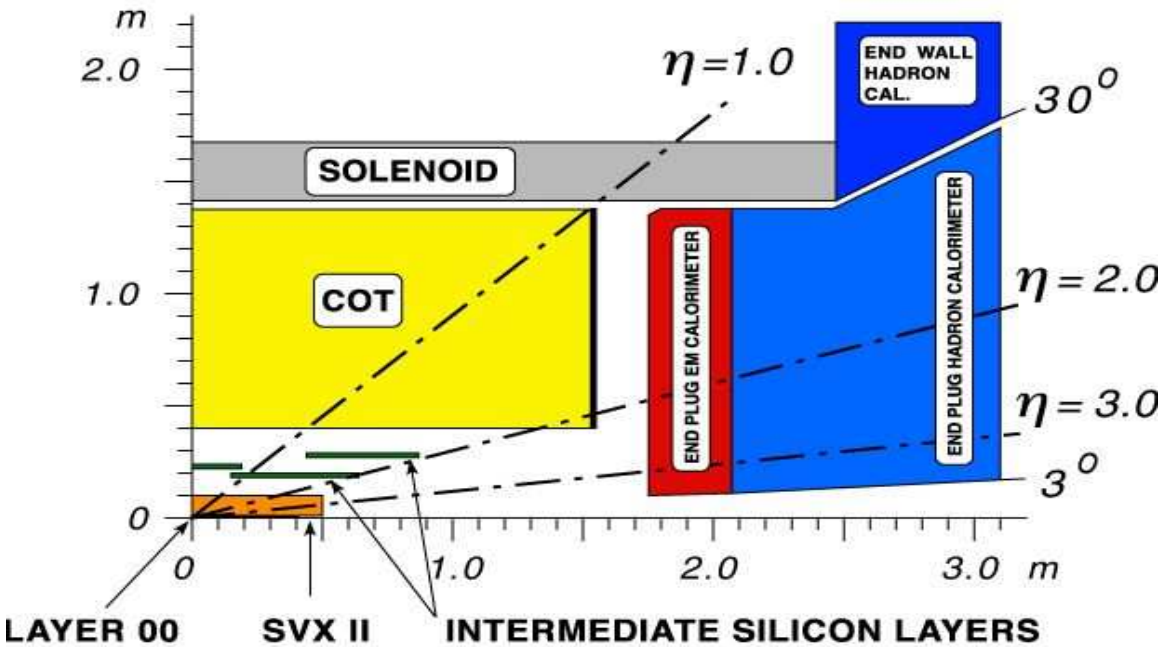

Figure 3.5: CDF tracking.

3-dimensional tracking close to the point of interaction. The impact parameter resolution is on order 40 μm, and is essential in locating the secondary vertices often associated with long-lived particle decay, such as with b mesons.

3.2.3 Central Outer Tracker

Surrounding the silicon system is a large cylindrical drift chamber, composed of thousands of drift wires. The COT [18] [19] extends radially from 40 to 132 cm relative to the beamline and is 3.1 m in length. The chamber is filled with an Argon/Ethane 'fast' gas, and many layers of wires, subdivided into 8 superlayers. Each layer consists of a number of cells, containing sense wires with a positive voltage of $\approx 3kV$ acting as an anode, potential wires outside and in between each layer with a lower positive

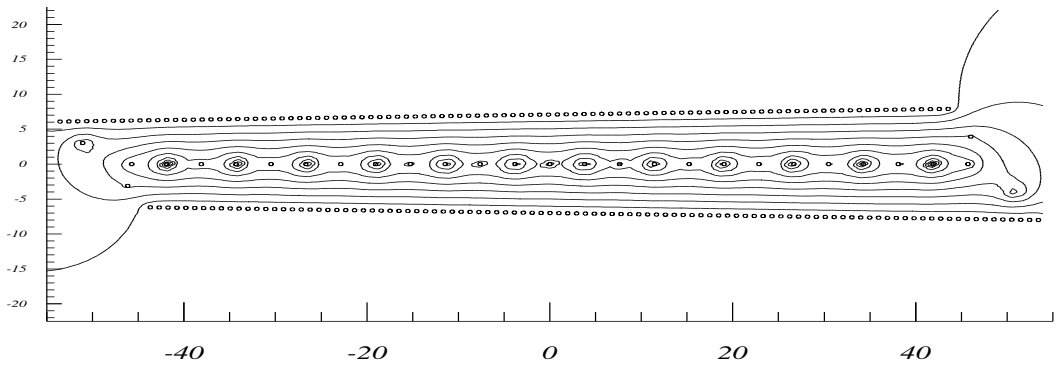

Figure 3.6: Equipotential lines in a COT cell.

voltage ($\approx 2kV$), and are divided by cathode field panels. There are variable voltages ($< 400V$) among the sense and potential wires in order to create a uniform drift field in each cell. As a charged particle passes through any given cell, it leaves a trail of e^--ion pairs. The ions drift towards the sense wires, igniting an avalanche of charge within a few radii of the wire. A pulse of current is sent down the wire, signaling a hit on that particular wire. The amount of time between the initial collision and the signal pulse is related to the charged particles distance from the wire, offering spatial information more resolute than the distance between sense wires. The trajectory of a charged particle is mapped out by a series of hits on the wires in the COT. Bending due to the magnetic field, the transverse momentum of the track is calculated as $p_T = qBr$, where $B = 1.4T$, q is the charge of the particle, and r is the radius of curvature. Momentum resolution of tracks in the COT changes as a function of p_T, and is calculated as $\sigma_{p_T}/p_T^2 = 1.7 \times 10^{-3}$.

3.2.4 Calorimeters

Momenta measurements from CDF tracking are often used to measure objects such as high P_T charged leptons, but cannot measure neutral particles such as neutrons which are often associated with jet activity. Once particles have traversed the COT, their energy can be collected and measured with detectors called calorimeters. Calorimetry at CDF is located outside of the solenoid and is divided into central and plug (forward) regions. The central region stretches from the center of the detector out to $|\eta| < 1.1$, while the plug calorimetry forms the bookends of the detector, collecting the energy of particles at high pseudo-rapidity ($3.6 > |\eta| > 1.1$). The composition of the calorimetry creates a grid of calorimeter 'towers', with each tower occupying approximately 15 degrees in ϕ and 0.11 in η in the central region. The plug towers are more variable in size, growing from $\phi \approx 7.5 - 15$ degrees and $|\eta| \approx 0.1 - 0.2$ as $|\eta|$ increases from 1.1 to 3.6.

Two types of calorimeters exist for the collection of energy from different particle types. Electromagnetic and hadronic calorimeters are designed specifically to collect energy from photons and electrons or hadronic particles such as pions and neutrons respectively. Electromagnetic (EM) calorimeters [20] are located in front of the hadronic calorimeters, and are composed of layers of lead, separated by scintillator designed to collect light and focus it towards photomultiplier tubes. Electrons undergo bremsstrahlung radiation, while photons typically convert into an e^+e^- pair when entering EM calorimeters. A cascade effect manifests as photons pair convert and $e^\pm$ radiate until the vast majority of scintillation light has been collected and residual electrons and positrons have lost sufficient energy and ionize. The radiation length (X_0) is the average distance an electron travels in a given material before only

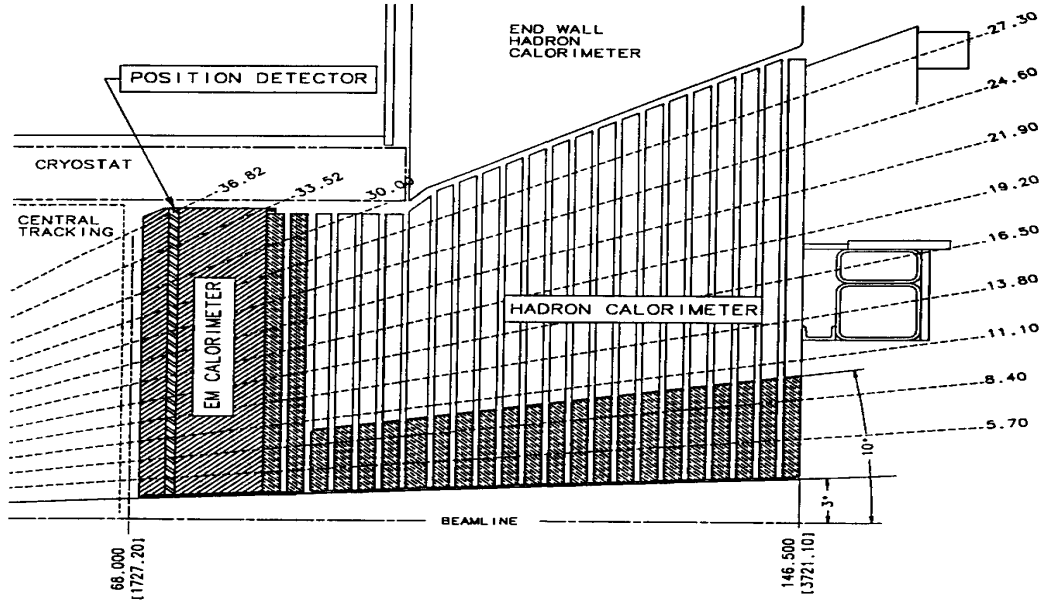

Figure 3.7: An illustration of the electromagnetic and hadronic calorimetry in CDF.

1/e of its energy remains. The total EM calorimeter extends to nearly 20 radiation lengths so as to contain all energy from an EM shower. An additional Shower Maximum Detector is located at slightly less than one third the total depth of an EM tower, which is the expected maximum of the EM showers spread. Its purpose is to improve the spatial resolution on the position of the shower, and to profile its shape.

While electrons and photons will tend to deposit a majority of their energy in the EM, hadronic particles have different properties and undergo a showering process which takes much longer to evolve. Hadronic energy loss will occur primarily through nuclear collisions with the absorbing medium and ionization. This type of cascade will often begin in the EM calorimeter, but extend into the hadronic calorimeter [21] for the majority of a showers energy deposition. Iron is utilized as the absorbing

material in these calorimeters, with scintillator placed in between layers as before. The longer showering process motivates a larger amount of material, and longer length of layers between scintillator. The length of a hadronic shower is characterized by its interaction length, the average distance traveled for a hadron to experience a nuclear interaction with surrounding material. Interaction lengths are much longer than radiation lengths, and although the hadronic calorimetry is composed of much more material, it is only 4.5 interaction lengths deep in the central region and 7 in the plug. Energy resolution of particles and showers is vital to data analysis at CDF. The resolution of the calorimetry was measured with a test beam, and is different for EM, HAD, central and plug [22] calorimeters. The measured energy resolution of the EM is $14\%\sqrt{E_T} \oplus 2\%$ in the central region and $16\%\sqrt{E} \oplus 1\%$ in the plug, while the hadronic energy resolution is $75\%\sqrt{E}$ in the central region and $80\%\sqrt{E} \oplus 5\%$ in the plug.

3.2.5 Muon Detectors

The outermost detectors in CDF are the muon systems [23]. Muons do not interact strongly with the calorimeters like electrons due to their much larger mass, and will typically only deposit a small amount of minimum ionizing energy. Passing through the inner portions of the detector, muons can be identified by leaving a short trail in small tracking chambers outside of the bulk of the detector. The muon detectors consist of four rectangular gas chambers, positioned parallel to the beamline, recording the ϕ position of a particle exiting the detector. Additionally, due to large drift time in the muon chambers, there are layers of scintillator which provide more accurate timing information. Since all other particles produced in a given event

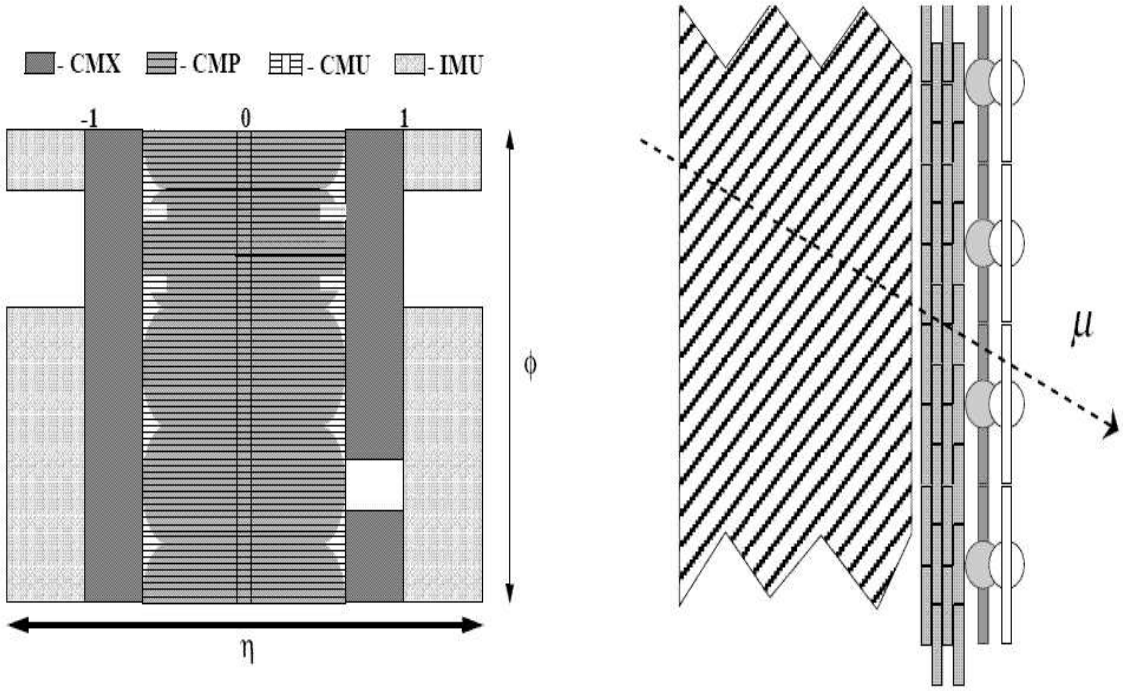

Figure 3.8: CDF Muon detectors.

will likely be stopped in the calorimetry, it is highly efficient to locate a muon by requiring that a short muon 'stub' from a muon chamber point to a high P_T track in the COT. The Muon system is divided into subdetectors which provide coverage for particular $|\eta|$ regions. The most central region ($0.0 < |\eta| < 0.6$) is covered by the Central Muon detector (CMU) and Central Muon Upgrade (CMP). The Central Muon Extension (CMX) adds additional measurement capabilities for moderately central muons at ($0.6 < |\eta| < 1.0$), and the Barrel Muon Upgrade (BMU) extends from $1.0 < |\eta| < 1.5$.

3.2.6 Cherenkov Luminosity Counter

The goal of the Tevatron accelerator is not only to provide high energy beams to the detector experiments, but to pack as many protons and antiprotons as possible into the 36 bunches circulating the ring. Luminosity in proton-antiproton colliders is defined as

$$\mathcal{L} = \frac{n_{bunches} N_p N_{\overline{p}} f}{2\pi(\sigma_p^2 + \sigma_{\overline{p}}^2)} F\left(\frac{\sigma_l}{\beta}\right)$$

Greater luminosity in the beams enhances the probability of producing more high quality collisions, providing larger datasets for analysis. As stated in the definition, luminosity depends of many quantities, some of which are constant at the Tevatron. The number of bunches (n=36) and revolution frequency (f$\approx 48kHz$) are constant, while N_p and $N_{\overline{p}}$ vary depending on how many protons and antiprotons are packed into the initial beams, and will continually decrease for the duration of the lifetime of the beams. The Form factor $F\left(\frac{\sigma_l}{\beta}\right)$ is about 0.7, and σ_p and $\sigma_{\overline{p}}$ represent the spatial standard deviation of the beams at the interaction point in the detector.

Measuring the instantaneous luminosity of beams at the Tevatron is of vital importance, as it must be integrated over time to calculate the total amount of data in a sample. This is a crucial component in making accurate predictions and measurements in analysis of the data. The CLC (Cherenkov Luminosity Counter) [24] are cone-shaped detectors filled with isobutane positioned near the beamline. Cherenkov light is collected by the detector from inelastic proton-antiproton scattering, measuring the average number of interactions for each bunch crossing (μ). The luminosity can be calculated directly from this quantity, since the inelastic cross section (σ_{in})

and bunch crossing frequency (f_{BC}) are known constants.

$$\mathcal{L} = \frac{\mu f_{BC}}{\sigma_{in}}$$

3.3 Data Acquisition

The Tevatron has produced trillions of $p\overline{p}$ collisions for analysis by the CDF and DØ collaborations. While the large luminosities provide enormous amounts of data for analysis, the rate of recorded data must be controlled due to limited resources and practicality. Bunch crossings occur at a rate of 2.5 MHz, and with each event amounting to approximately 250 kB of data, over a terabyte of disk space would be required every 2 seconds. However, the probability that a proton-antiproton collision will result in truly interesting physics is small, hence the need for large luminosities, making the majority of events useless to record. A 'trigger system' is utilized by CDF to identify useful physics events and control the rate of data recorded. The trigger system at CDF is broken into 3 separate levels, with the processing time increasing by orders of magnitude in each phase. The overall system reduces the flow of data to a rate of about 50 Hz, making the data actually written to tape much easier to manage and analyze.

3.3.1 Level One Trigger

Data from each crossing of the proton-antiproton bunches first passes through fast hardware designed specifically to identify particular aspects of a physics event. With bunch crossings occurring every 396 ns, the hardware must process information from components of the detector in this amount of time. Specific hardware is designed to identify interesting activity in different parts of the detector. For instance, the

eXtrememly Fast Tracker (XFT) searches for high P_T tracks by utilizing information from the COT. Electronic pulses on the wires in the gas chamber are analyzed by 'finder' hardware, which search for hit patterns in one of the COT's superlayers and proceed to forward this information to the Linker system. The Linker hardware collects hit information from multiple finders, searching for patterns consistent with a single track traveling through multiple layers of the tracking chamber. Tracks at the linker level are characterized by their P_T, directly related to a track's curvature in the magnetic field, and its ϕ position in the detector. The information at this point is restricted solely to propagation in the transverse direction, only utilizing data from the axial layers of the COT. The upgraded XFT improves upon this design by incorporating tracking from the stereo layers, which yield additional information in the direction of the beamline. High luminosities at the Tevatron have motivated this upgrade, as the number of tracks in any given event greatly increases with the number of proton-antiproton interactions per bunch crossing. Multiple low momenta overlapping tracks can fake the signature of a single high momenta track, which raises the trigger rate by accepting unwanted events. Hardware designed to find hit patterns in the stereo layers is sent to electronics which associate tracks identified by the Linker system to stereo layer hits. Good tracks will not only be identified by the linker, but will also have a set of hits from the stereo finders that are consistent with a true charged particle traversing the detector with some momentum parallel to the beamline. The tracking information is finally combined with data from additional trigger hardware associated with electromagnetic calorimetry and muon systems for the purpose of electron or muon identification.

There are many other triggers which each look for different characteristics of an event, such as large energy deposition in a number of calorimeters or a large imbalance in energy. Overall, the level one trigger system reduces the rate of data dramatically by accepting events at a rate of about 50 kHz.

3.3.2 Level Two Trigger

Events accepted by the level one trigger proceed to the second stage of the trigger system for further analysis. Hardware is utilized at this stage as well, but more time is allocated for detailed analysis of the event due to the reduced event rate. Analysis of events can include silicon information, calorimeter clustering for jet and electron identification and more complex tracking reconstruction. A 20 μs time window is available at level 2 to analyze the data and decide whether an event should be passed to the final trigger level. Events pass the second trigger level at a rate of about 300 Hz.

3.3.3 Level Three Trigger

The level three trigger is software-based, consisting of 300 dual-processor computers which fully reconstruct an event for analysis. These triggers are optimized to efficiently accept physics of interest while reducing the rate of background. In this analysis, the level three trigger searches for missing energy greater than 35 GeV, and two jets greater than 10 GeV, with one of the jets required to be central in the detector. This event signature accepts a large portion of the signal, while rejecting the largest backgrounds at a much higher rate. Level 3 triggers for other CDF analyses may search for different event characteristics, depending on the physics analysis which will ultimately be performed. The data for events passing this trigger level

are written to tape and permanently recorded. The final data rate is about 50 Hz, a factor of 50,000 less than the frequency of bunch crossings at the Tevatron.

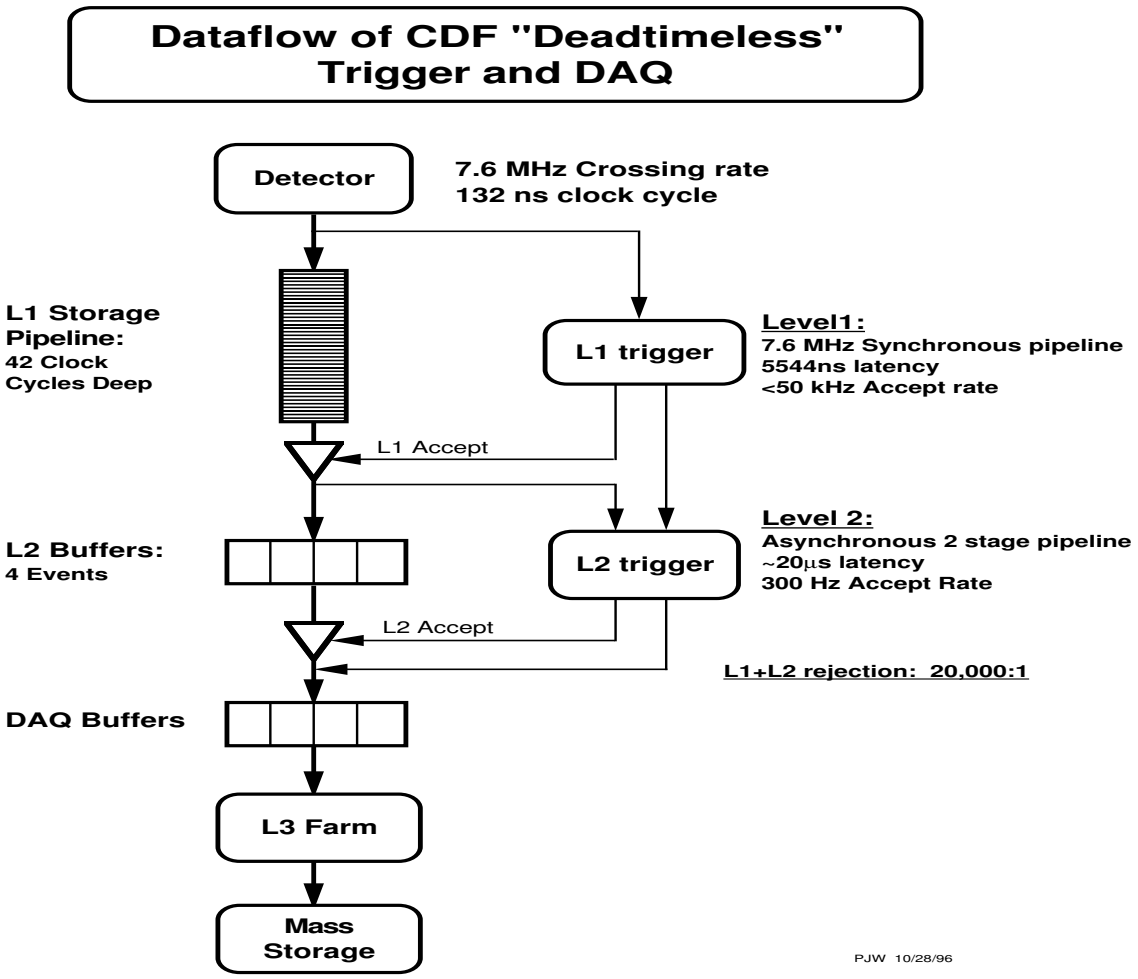

Figure 3.9: Graphical representation of the flow of CDF data through the trigger and DAQ system.

CHAPTER 4

ANALYSIS OVERVIEW

The subject of this dissertation is a search for the Standard Model Higgs boson in the $ZH \rightarrow \nu\nu b\bar{b}$ channel. The $Z \rightarrow \nu\nu$ decay makes this a fairly unique high-energy physics analysis, as half of the final state products escape the detector, and can only be roughly reconstructed by an imbalance in energy of measurable objects. Even in this case only the Z-system is being inferred, and any information on the individual neutrinos is completely lost. While certain aspects of this mode are undesirable and problematic, there are also advantages that make this particular channel a very exciting prospect for the observation of Higgs at CDF. The $Z \rightarrow \nu\nu$ decay mode has a branching ratio approximately 3 times as high as $Z \rightarrow e^+e^-$ and $Z \rightarrow \mu^+\mu^-$ decays combined, which is extremely valuable in the case of Higgs analysis where the cross section is so small. Additionally, a contribution from the $WH \rightarrow l\nu b\bar{b}$ channel also adds to the signal expectation for the event selection utilized by this analysis. The dedicated WH analysis at CDF requires an identified electron or muon candidate plus a moderate amount of missing transverse energy from the neutrino (typically about 20 GeV) to reconstruct the W. However, lepton identification is not a fully efficient process, and a reasonably large amount of WH events do not pass event selection when a lepton (electron or muon) is required. However, this analysis has a

method to recover some of these events, since the only requirement with respect to vector boson identification is a large amount of missing transverse energy. A lepton veto is implemented to keep the two Higgs analyses orthogonal. Thus this analysis becomes not just a search for ZH, but for WH as well, boosting the potential for large sensitivity to a Standard Model Higgs processes.

4.1 Event Reconstruction

The main decay products relevant to Higgs analysis at CDF all leave unique signatures in the detector which are used to characterize an event. Different components of CDF specifically designed for the purpose of identifying interesting physics objects work together to characterize the aftermath of a proton-antiproton collision. The measurements produced by all of these components are absolutely essential to wade through the trillions of collisions and produce analyses which are reasonably sensitive to signals which can be on the order of a single event.

4.1.1 Electrons

High energy electrons play a crucial role in a large number of analyses at CDF, as leptons are the single most important identifier of W and Z bosons. Electrons can be produced in other ways, but yield unique signatures when they are a decay product of a W or Z. These electrons often appear as a single track in the COT pointing towards a large amount of energy deposition in the electromagnetic calorimeters. Electrons identified by the CEM (Central Electromagnetic) calorimetry tend to be better measured and are able to take advantage of better tracking due to it's low pseudorapidity of $|\eta| < 1.1$. The PEM (Plug Electromagnetic) calorimetry can identify more forward electrons in the range of $(2.0 \gtrsim |\eta| > 1.1)$

A number of quality requirements are made for identifying good electron candidates. These are different depending on whether the electron candidate is in the central or plug region of the detector. The main difference is driven by the loss of tracking efficiency in the COT at large η. Instead of making tracking requirements related to the COT as in the CEM, PEM electrons are required to have a track in the silicon detectors. Electron ID for this analysis follows the guidelines outlined for top quark analysis at CDF. The main requirements are an $E_T \geq 20$ GeV in the electromagnetic calorimeter, a track that originates within 60 cm of the center of the detector, an isolation[1] less than 0.1, and the Had/EM energy being less the about 0.055, although this cut changes for CEM electrons as a function or energy. A number of additional quality cuts are made, but these are different for central and plug electrons. The full set of cuts are listed in table 4.1.

4.1.2 Muons

While both muons and electrons are unique physics objects which are crucial to identifying electroweak physics, they behave quite differently in the detector. While both are charged particles that can be identified with tracking, muons will typically only deposit some minimum ionizing energy in the calorimeters unlike electrons. The muon detectors discussed in section 3.2.5 are utilized by extrapolating a track in COT to the muon "stub". As is the case with electrons, an isolation requirement (Iso $\leq$ 0.1) is made, and additional quality cuts are implemented to improve purity. These cuts are listed in table **??**. Cuts below the line are specific to certain muon detectors. Tight muons are defined as those identified by the CMUP or CMX muon chambers.

[1]isolation is the energy around the main electron cluster in a cone of $\Delta R < 0.4$ divided by the total energy in the electromagnetic cluster associated with the electron candidate

Selection	Central (CEM)	Plug (Phoenix)
E_T	$\geq 20GeV$	$\geq 20GeV$
HAD/EM	$\leq (0.055 + (0.00045 \times E))$	≤ 0.05
Isolation	≤ 0.1	≤ 0.1
Track Z_0	$\leq 60cm$	$\leq 60cm$
Track P_T	$\geq 10GeV/c$	
COT Axial Segments	≥ 3	
COT Stereo Segments	≥ 2	
Silicon Hits		≥ 3
L_shr	≤ 0.2	
E/P	$\leq 2.0 for P_T \leq 50GeV/c$	
χ^2	≤ 10.0	≤ 10.0
$Q \times \Delta x$ CES	$-3.0 \leq Q \times \Delta x \leq 1.5$	
Δz CES	$\leq 3.0cm$	
ΔR PES		$\leq 3.0cm$
Phoenix Match		TRUE

Table 4.1: *Requirements for identifying electron candidates. Events with identified electrons are vetoed.*

Loose muons include the 'fill in the gap' muon detectors, including the BMU detector. Also included are CMIO muons, which are candidates with a central COT track and minimum ionizing calorimeter deposition, but no muon stub. Muon selection with both the tight and loose classification are used in this analysis for different purposes, which are discussed in detail in sections 5.3 and 8.2.

4.1.3 Jets

These are the most common physics objects identified at CDF, as they are the easiest to produce. Jets are the measurable by-products of many different processes. High energy quarks can be produced in a number of ways, including direct pair production, decay of a vector boson or higher order QCD diagrams. Additionally, high energy gluons can be produced directly from the main $p\overline{p}$ physics or gluon radiation by the final state quarks. These individual quarks and gluons begin a fragmentation

Selection	Cut
P_T	$> 20GeV/c$
E_HAD	$< 6 + max(0, (p - 100) \cdot 0.028)$ GeV
E_EM	$< 2 + max(0, (p - 100) \cdot 0.0115)$ GeV
E_T^{Iso}/P_T	< 0.1
Track Z_0	$< 60cm$
COT Axial Segments	≥ 3
COT Stereo Segments	≥ 2
Impact Parameter d_0	$< 0.2cm(0.02w/siliconhits)$
χ^2	< 2.3
CMU Δx	$< 7cm$
CMP Δx	$< 5cm$
CMX Δx	$< 6cm$
CMX $\rho_C OT$	$> 140cm$
BMU Δx	$< 9cm$
CMIO $E_{EM} + E_{HAD}$	$> 0.1GeV$

Table 4.2: *Requirements for identifying muon candidates. Additional matching requirements are imposed depending on which muon type the candidate is.*

process fueled by the strong force. The strong force between colored particles grows with distance unlike forces such as gravity and electromagnetism. A free quark will almost immediately proceed to rip a quark out of the vacuum through pair production, forming a hadron and leaving another free quark as a catalyst for the same effect. This process continues, forming a spray of mesons and baryons containing the overall energy and momentum vector of the original parton (quark or gluon). On average, jets are more poorly measured than electrons and muons, as the energy of the original parton is spread amongst multiple particles, and the showering and energy loss of hadronic particles in the calorimeters is primarily due to atomic collisions rather than ionization as in an electromagnetic shower. However, while not as well measured, jets are extremely important in characterizing events, and jets resulting from b quark

production in particular have special properties that are valuable to low mass Higgs searches.

Jets are measured in the calorimeter by utilizing a clustering algorithm called JetClu. [25] First, all calorimeter towers with a measured energy above 1 GeV are listed as seed towers. Preclusters are subsequently formed with groups of 3 towers in ϕ by adding adjacent seed towers with decreasing E_T with respect to the central towers in the precluster. The preclusters are then utilized as the base for forming clusters, by producing a cone around the center in ΔR ($\sqrt{\Delta\phi^2 + \Delta\eta^2}$). A cone size of 0.4 in ΔR is used in this analysis. All towers in the cone with energy greater than 100 MeV are then added to the cluster. The cluster centroid is then recomputed and reclustering occurs iteratively until a stable cluster is formed. If overlapping clusters share greater than 50% of their energy, they are merged together. Once the algorithm reaches a point where there are well separated clusters, they are defined as jets for analysis.

The "Raw" energy measured for a jet by the clustering algorithm must be corrected for a number of effects inherent to detector response and the overall physics of an event producing a jet. Data produced by test beams and monte carlo studies have determined a number of effects which are corrected for to improve the reconstruction of physics produced in $p\overline{p}$ collisions. [26] The effects compensated for by corrections in this analysis are as follows.

- η-dependence: The CDF calorimetry, while essentially homogeneous in the transverse plane other than cracks between calorimeter towers, responds differently to jets depending on their pseudorapidity. Corrections to jets are applied with respect to their η position in the detector to remove variations caused by

instrumental effects. Studies were performed utilizing dijet balancing methods with one jet in the best understood region of calorimetry ($(0.6 > |\eta| > 0.2)$) being used to scale jets in other regions of the detector.

- Multiple Interactions: While it is extremely unlikely that two $p\overline{p}$ interactions in the same event will both result in interesting physics, it is common for there to be multiple minimum bias $p\overline{p}$ collisions separate from the main interaction of interest. Multiple interactions can be identified by additional primary vertices located away from the main vertex associated with high energy jets or leptons. These minimum bias interactions can result in additional energy being deposited in the calorimeters, motivating a correction for jets according to the number of primary vertices in an event. This effect is greater for jets with larger cone sizes.

- Absolute Jet Energy Scale: These corrections are designed to relate the response of particles in the calorimeter back to the momenta of the original hadrons in the jet. Jets can consist of many different types of particles such as π^0's which primarily interact electromagnetically (CEM, PEM), and particles which interact hadronically such as neutrons, protons and $\pi^{\pm}$'s. Detailed studies have generated mapping functions between calorimeter response and hadron-level jets to provide the absolute jet energy scale corrections used in this analysis. Correcting jets for these effects are extremely important, as accurate Monte Carlo models are essential for making predictions and characterizing the reconstructed objects from the main physics processes produced in collisions.

4.1.4 Missing Transverse Energy

The missing transverse energy or $\not\!\!E_T$ is an extremely important quantity in all electroweak analyses. The momentum of the main interacting particles in a $p\overline{p}$ collision should be essentially zero in the direction transverse to the beamline. Conservation of momentum places powerful constraints on the kinematics of the fundamental partons involved in a reconstructed event. The $\not\!\!E_T$ in an event is calculated by summing the energy deposition vectors of all calorimeter towers in the detector. Taking into consideration the z position of the primary interaction vertex, the x and y, or transverse components of the sum are used the calculate the $\not\!\!E_T$ in an event. In a scenario in which all objects were perfectly measured in the detector, this quantity would sum to zero due to momentum conservation. The most useful application of this quantity however, is the case in which one of the particles in the underlying physics process is undetectable by CDF. Neutrino's very rarely interact with matter, and the probability of them leaving a detectable signature in a calorimeter is extremely small. Therefore, the $\not\!\!E_T$ is an excellent way to infer the presence of a neutrino in a physics event. After summing the energy deposition from measurable objects, there often is an imbalance which is characteristic of some of the event momentum being lost due to a neutrino. After full event reconstruction and the $\not\!\!E_T$ being corrected for the z position of the primary vertex, the corrections applied to identified jets are considered as well. Corrections to the jet energy scale better reconstruct an event, and applying these correction to the $\not\!\!E_T$ as well will improve it's resolution relative to the true neutrino P_T. The $\not\!\!E_T$ is solely a transverse vector, so the transverse components of the corrections to jet E_T are subtracted from the $\not\!\!E_T$ vector.

$$\overrightarrow{\not{E}_T}^{Corr} = \overrightarrow{\not{E}_T}^{Raw} - \sum_{i=1}^{N_{jet}} \overrightarrow{E_T}_i^{JetCorr}$$

The $\not{E}_T$ is a critical quantity in this analysis for many reasons. The signal processes involve one or two final state neutrinos, so the experimental expectation is that most events of this type will produce a very large amount of missing energy. Therefore, it is crucial to have an accurate measurement of this quantity, as it holds a large amount of the kinematic information present in the event. In addition, the data for this analysis is collected on a $\not{E}_T$ trigger, making the understanding of its magnitude, direction and relation to other event quantities crucial.

4.1.5 Secondary Vertex Identification

The production of Higgs in association with a vector boson has a very small cross section with respect to all major backgrounds. However, the branching ratio of $H \rightarrow b\overline{b}$ is large for low Higgs masses, which is an extremely beneficial feature due to the special properties of b hadrons. The silicon tracker described in section 3.2.2 is the closest component of CDF to the beamline, and has the ability to identify and reconstruct secondary vertices (vertex displaced from the primary vertex) which are characteristic of hadron decay. Specifically, hadrons created from b quark production are ideal candidates for these measurements. The particle states formed with b quarks travel a finite distance, often decaying within the resolution of the silicon detector. Hadrons formed with charm quarks decay more quickly (travel shorter distances) than bottom hadrons, and hadrons consisting of only strange, up or down quarks typically decay quickly through an electromagnetic process or have much longer lifetimes and escape the silicon before decaying. Therefore, secondary vertices reconstructed by the

silicon detectors provide invaluable information for analyses attempting to create a purified data sample consisting primarily of processes involving b quarks.

Two separate algorithms are utilized in this analysis to identify secondary vertices. The first, labeled "SecVtx", requires at least 2 good silicon tracks within the cone of a jet [27]. The algorithm searches for a significant displaced vertex with respect the primary interaction point. This vertex is characteristic of a b hadron decaying into particles consisting of lighter quarks. Once a secondary vertex has been identified, the distance from the primary vertex can be calculated (L_{xy} or L_{xyz}), as well as a number of other useful quantities such as the vertex mass. These quantities can be used to determine the quality of the vertex, or how likely it is that the secondary vertex is, in fact, associated with the decay of a b hadron. This analysis utilizes the "Tight" SecVtx requirements, for reasons discussed in the analysis section.

The second tagging algorithm used for bottom identification is "Jet Probability" [28]. This method uses a different strategy for identifying displaced vertices. Silicon tracks are evaluated by the closest point of spatial approach to the primary vertex, which is known as the impact parameter (d0), along the trajectory of the jet momentum. The probability of a track being inconsistent with originating from the primary vertex is calculated. The probabilities of multiple tracks are combined to from an overall probability, which is interpreted as the likelihood that a jet does not contain secondary vertices from a long-lived hadron. Therefore, a low value of the jet probability variable is of interest when attempting to purify a data sample for physics involving b quarks. The"loose" convention is adopted for studies and analysis, which corresponds to a jet probability of less than 5%.

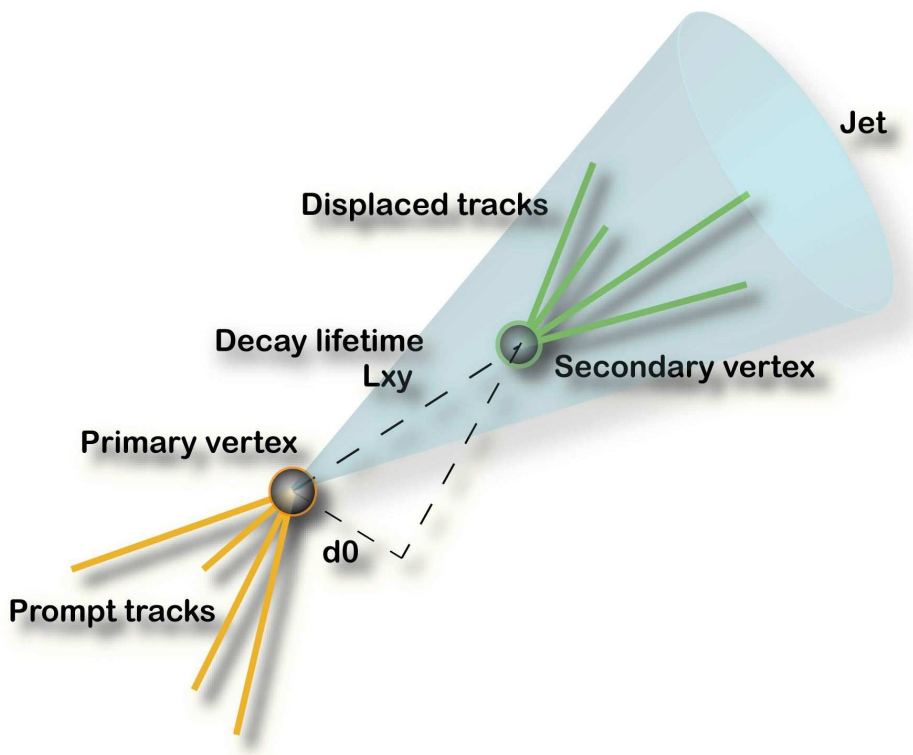

Figure 4.1: Figure illustrating a displace vertex typical of b jet decay.

4.2 Properties of Signal Processes

This analysis attempts to provide a probe into the massive amounts of data CDF has collected, with the purpose of extracting as sensitive a measure of the Standard Model Higgs boson as possible. As mentioned previously in this chapter, the specific decay channel considered is the $ZH \rightarrow \nu\nu b\bar{b}$ process, with a significant boost in signal from $WH \rightarrow l\nu b\bar{b}$ in which the lepton is unidentified. Therefore, the ideal Higgs candidate will be measured as two high E_T jets with measured secondary vertices,

which should reconstruct to form the Higgs mass.

$$M_H = M_{bb} = \sqrt{(\sum_{i=1}^{2} E_i)^2 - (\sum_{j=1}^{2} P_j^x)^2 - (\sum_{j=1}^{2} P_j^y)^2 - (\sum_{j=1}^{2} P_j^z)^2}$$

In addition, an ideal event will produce a large amount of $\not{E}_T$, recoiling such that the momentum vector of the dijet system is pointed away from the $Z \rightarrow \nu\nu$ momenta. This analysis is constructed to take advantage of the specific physics involves in $ZH \rightarrow \nu\nu b\bar{b}$ events, and by developing an event selection in which these properties are considered, a large amount of background can be rejected while keeping a good portion of the signal available for the possibility of measurement.

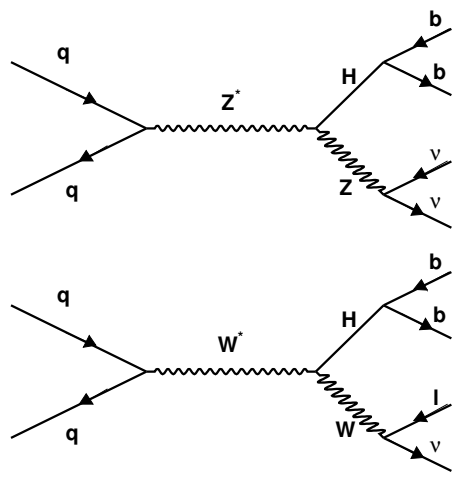

Figure 4.2: The $ZH \rightarrow \nu\nu b\bar{b}$ and $WH \rightarrow l\nu b\bar{b}$ processes

The WH process has many similar qualities to the main ZH signal. While an event selection optimized for ZH will have a lower selection efficiency for WH, this process has a larger cross section at the Tevatron so that a substantial portion of the total signal yield will consist of this particular process. Not surprisingly, the feature

of accepting both W and Z physics for the purpose of signal measurement means that both W and Z background processes must be considered, as well as others.

CHAPTER 5

DATA SAMPLE AND EVENT SELECTION

5.1 Event Triggers

The data for this analysis is collected on triggers designed to search for events with properties similar to that of the main signal process. The CDF trigger system, as described in chapter 3, is split into three levels which calculate event quantities in increasing detail with the third trigger level representing a fully reconstructed event similar to those at the analysis level. The level one trigger is designed to accept events with a $\not\!\!E_T$ greater than 25 GeV. This is performed by summing the energy in calorimeter towers to get a reasonable estimate of the $\not\!\!E_T$. Due to the extremely small time window in which this L1 $\not\!\!E_T$ must be calculated, the calorimeter sum has limited resolution and is not fully efficient until the fully reconstructed 'offline' $\not\!\!E_T$ reaches values much larger than 25 GeV. The level 2 trigger searches for clusters of energy in the calorimeters representative of jets. The level 2 algorithm will accept events in which two clusters of energy are reconstructed above an E_T threshold of 10 GeV. An additional requirement for this particular trigger was introduced for later runs at CDF to decrease the trigger rate. One of the reconstructed clusters must be at an $|\eta| < 1.1$, which reduces the rate while remaining highly efficient for signal. The event

selection in this analysis places a slightly tighter cut on at least one of the jets, so that no trigger bias is introduced.

The level three trigger can take advantage of a full event reconstruction to more accurately measure the $\not\!\!E_T$ in an event. A threshold of $\not\!\!E_T > 35GeV$ is applied to events passing the L1 and L2 triggers. Therefore, the final event selection reflects the trigger requirements imposed on the collected data. Overall, events selected by the trigger are required to have a missing transverse energy of at least 35 GeV as well as at least two jets, which is an event signature similar to what one might expect from a typical ZH event. Table 5.1 displays the specific level 3 trigger used for events in a particular run range.

RunRange	Trigger Description
141544-195805	Met > 35 GeV and at least 2 10 GeV Jets
195809-223177	In addition, at least 1 Jet with $\|\eta\| < 1.1$
223233-235232	Trigger turned off if Inst. Lumi. > 190
235389-236255	Dynamically Prescaled
236256-237795	Trigger turned off if Inst. Lumi. > 190

Table 5.1: *Triggers used to collect data in different periods of data acquisition*

5.2 Cleanup of Missing E_T Data Sample

Due to the nature of events collected by Missing E_T triggers, it is advisable to remove a large portion of the dataset that do not contain interesting physics. Studies of data collected at CDF have shown that these type of events are largely caused by effects such as beam halo, muon bremsstrahlung, cosmic rays and detector

inefficiencies[29]. A series of quality cuts motivated by these studies are implemented in data and Monte Carlo to cleanup unwanted events collected by the MET35 triggers.

- At least one Z-Vertex with class > 11
- At least one track in the central tracking system with COT hits and $P_T > 0.5$
- Require that at least 10% of the sum of all jet E_T is deposited in the electromagnetic calorimetry.
- Require that the total track P_T over E_T of all jets divided by the number of jets is greater than 0.1.

$$\frac{1}{N_{jet}} \sum_{j=1}^{N_{jet}} \frac{\sum P_T}{E_T} > 0.1 \tag{5.1}$$

- Jets that fall within $0.5 < \eta < 1.0$ and $1.04 < \phi < 1.74$ are often mismeasured. This region, known as the chimney, contain a large of instrumentation and often produces a second jet measured low, as can be seen in figure 8.1. Events with jets falling in this region are vetoed.
- Tests of QCD modeling are performed in a region in which the $\not\!\!E_T$ is aligned with the second jet. A large number of jets passing selection in this region are located at $|\eta| < 0.1$. These events are removed in this region since the $\not\!\!E_T$ is likely due to the instrumental effect of a large crack at $\eta = 0$. Studies of Pretag data (data prior to tagging requirements) show that this effect is not present in the signal region.

In addition to removing events with fake $\not\!\!E_T$, some event cuts are utilized to account for the efficiency turn-on of the triggers[30].

- Jets in the event are required to be separated by a cone of ΔR > 1.0 to avoid cluster merging.

- A centrality requirement of $|\eta| < 0.9$ on at least one jet is applied due to the central jet trigger requirement.

- A cut is placed on the missing transverse energy in the event. The $\not\!\!E_T$ in the event must be recalculated after applying corrections to jets in the event. Only jets with a raw $E_T > 10.0$ GeV and $|\eta| < 2.0$ are corrected. The Missing E_T is then corrected by the difference between raw and corrected E_T for each jet. While the trigger threshold for the uncorrected $\not\!\!E_T$ is set at 35 GeV, the efficiency is low for events with this corrected $\not\!\!E_T$. Therefore, a threshold of 50 GeV in corrected MET is set for an event to be accepted.

The trigger study cited above has parameterized the efficiency curve as a function of the corrected missing E_T, and this is accounted for in all monte carlo signal and background. The efficiency at the $\not\!\!E_T$ threshold is calculated to be 83%, becoming about 94% efficient at 60 GeV and 99% efficient at 70 GeV.

5.3 Event Selection

In addition to trigger driven requirements, other cuts are placed on events to remove background. These are designed to isolate the kinematic region which is most likely to contain Higgs events, and least likely to be overwhelmed by background.

- Events with 2 and only 2 jets with $E_T > 20$ GeV and $|\eta| < 2.0$(Tight) are accepted.

- If a third jet is found at high $|\eta|$ ($2.0 < |\eta| < 2.4$) having a corrected $E_T > 20$ GeV, the event is vetoed.

- In Higgs events, the leading jet is expected to be more energetic than that of most backgrounds. A leading jet requirement of 45 GeV is placed on all events.

- Events with identified high-energy electrons and muons are not accepted, as these are potential candidates for orthogonal WH searches. We implement the standard high-P_T definition of tight or loose leptons as a veto. However, we define a control region to test trigger efficiencies and multivariate distributions as events with an identified high P_T muon. This is discussed in detail in section 8.2.

- A cut is placed on events in which $\Delta\phi(\not{E}_T$ -Lead Jet) < 0.8. This cut is highly efficient for signal, and removes a portion of QCD background.

- The final cut placed on events is determined by the displacement between the $\not{E}_T$ and the second jet. The region in which the $\not{E}_T$ is aligned with the second jet consists almost entirely of multijet QCD production and is defined by $\Delta\phi(\not{E}_T$ -2nd Jet) < 0.4. A separate kinematic region defined by a cut of $\Delta\phi(\not{E}_T$ -2nd Jet) > 0.8 is used for the final signal region and for studies of electroweak Monte Carlo backgrounds.

5.4 b-Tagging

The long lifetime of b hadrons producing the reconstructible secondary vertices described in section 4.1.5 is essential to low mass Higgs analysis. Tagging jets that

appear to have a secondary vertex is an excellent way to control light flavor backgrounds in an analysis in which the signal is expected to have b content. Utilizing silicon tracking information and the SecVtx algorithm, tight and loose tags are assigned to jets passing event selection, creating the heavy flavor enriched samples that we are interested in. We define four separate tagging categories to utilize in modeling, or data to model comparisons. The first category involves events in which both primary tight jets have tight SecVtx tags. This data should consist primarily of events with two b jets, consistent with what one would expect from a Higgs signal. This sample will provide the most sensitivity in this analysis, due to its high efficiency for signal events compared to the largest backgrounds. If events do not satisfy this tagging requirement, events with one tight SecVtx tag as well as a second jet with Jet Probability of less than 5% are placed in a second tagging category. The background rate is expected to be slightly larger in this sample, while the signal yield is slightly smaller. The third tagging category is defined as events with only one tight SecVtx tag. Data falling into this category will provide the base of our heavy flavor QCD model. The procedure for extracting models from this data sample is described in detail later. If events do not satisfy any of these requirements, a single loose SecVtx tag is searched for. The purpose of this sample is to provide validation for the modeling of light flavor data which have been mis-reconstructed as having a secondary vertex. The tight version of the SecVtx algorithm is used to remove the highest quality tagging information, so that the remaining data consists of physics which would only be tagged after loosening tagging requirements. These events are rich in events with false tags, and provide a good source of testing the modeling of various kinematic distributions. Finally, events satisfying no tagging requirement are

labeled as un-tagged, and are utilized in multivariate training, described in Section 9.2.

CHAPTER 6

MODELING OF PHYSICAL PROCESSES

6.1 Higgs Signal

While this analysis is primarily geared towards a search for $ZH \rightarrow \nu\nu b\overline{b}$, a significant boost in Higgs signal from $WH \rightarrow l\nu b\overline{b}$ events is expected in which the lepton is unidentified. The search for Higgs production in a $\not\!\!E_T$ +jets data sample is focused on a low mass Higgs boson. The theoretical production cross section of ZH and WH drops as the mass of the Higgs increases, as well as the theoretical branching ratio of $H \rightarrow b\overline{b}$ [31] [32]. We therefore focus on the limited mass range in which we expect to have some sensitivity. Table 6.1 displays the total expected number of signal events to be produced for all relevant masses.

The theoretical production rates for events in which a Higgs boson is produced is extremely small compared to the backgrounds passing trigger requirements. Monte Carlo VH samples were generated with PYTHIA [33] for masses ranging from 110-150 GeV/c^2. Event selection cuts greatly reduce the event yield, which is then further reduced by the requiring secondary vertex tags on both jets in an event. These event reduction techniques described in Section 5 are all much more efficient for the signal, increasing our ability to ultimately attempt to fit the physics process of interest.

Mass	$BR(H \to bb)$	$\sigma(ZH) * BR(Z \to \nu\nu)pb$	Events
110	.77	.025	33.4
115	.73	.022	27.9
120	.68	.019	22.4
130	.53	.014	12.9
140	.34	.011	7.1
150	.18	.008	2.4
Mass	$BR(H \to bb)$	$\sigma(WH) * BR(W \to l\nu)pb$	Events
110	.77	.069	92.4
115	.73	.059	74.9
120	.68	.051	60.3
130	.53	.038	35.0
140	.34	.029	16.8
150	.18	.019	5.8

Table 6.1: *Signal events produced in 1.7 fb^{-1} prior to event selection or trigger efficiencies*

Table 6.2 displays the number of ZH and WH events expected after all selection has been performed with respect to Standard Model cross sections and branching ratios.

	$ZH \to \nu\nu b\bar{b}$ (Events)		$WH \to l\nu b\bar{b}$ (Events)	
Mass	Vtx + Prob Tag	Double Vtx Tag	Vtx + Prob Tag	Double Vtx Tag
110	0.63	0.78	0.46	0.57
115	0.54	0.68	0.41	0.49
120	0.46	0.59	0.32	0.39
130	0.30	0.38	0.21	0.25
140	0.17	0.20	0.10	0.14
150	0.07	0.08	0.04	0.05

Table 6.2: *Mean Signal event expectations in 1.7 fb^{-1} after event selection and trigger parametrization*

	$ZH \rightarrow \nu\nu bb$ efficiency		$WH \rightarrow l\nu bb$ efficiency	
Mass	Prob+Vtx Tag	2 Vtx Tags	Prob+Vtx Tag	2 Vtx Tags
110	2.35%	2.56%	0.62%	0.69%
115	2.50%	2.75%	0.68%	0.72%
120	2.64%	2.96%	0.69%	0.76%
130	2.92%	3.22%	0.75%	0.80%
140	3.18%	3.43%	0.76%	0.91%
150	3.39%	3.59%	0.85%	0.91%

Table 6.3: *Selection efficiency for Higgs events in the signal region.*

CHAPTER 7

BACKGROUNDS

A $\not{E}_T$ +jets Higgs search contains the exciting prospect of accepting both ZH and WH events with the same selection criteria. However, this of course means that there are many different backgrounds that will be accepted in the data as well. A thorough understanding of background compositions and kinematic shapes is crucial, motivating rigorous attempts to develop the model of each background process using methods that will accurately represent data consisting of many different types of physics.

7.1 Monte Carlo Models

7.1.1 Top pair production

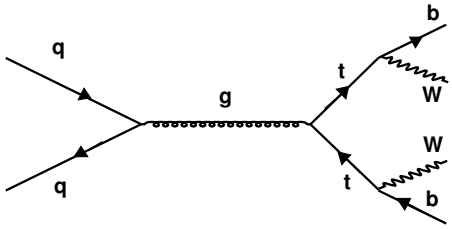

Figure 7.1: Feynman diagram of top pair production at the Tevatron

Top pair production provides one of largest contributions to the double tag categories in this analysis. The Monte Carlo based $t\bar{t}$ model includes all decay channels, and was generated with PYTHIA. Lepton+jets and dilepton $t\bar{t}$ events both provide energetic jets as well as Missing E_T, as both contain at least one neutrino. While multiple leptons or jets must be unidentified for $t\bar{t}$ events to pass selection and are accepted a much lower efficiency than signal events, the actual expected event yield is much higher due to the large production cross-section.

7.1.2 Single Top

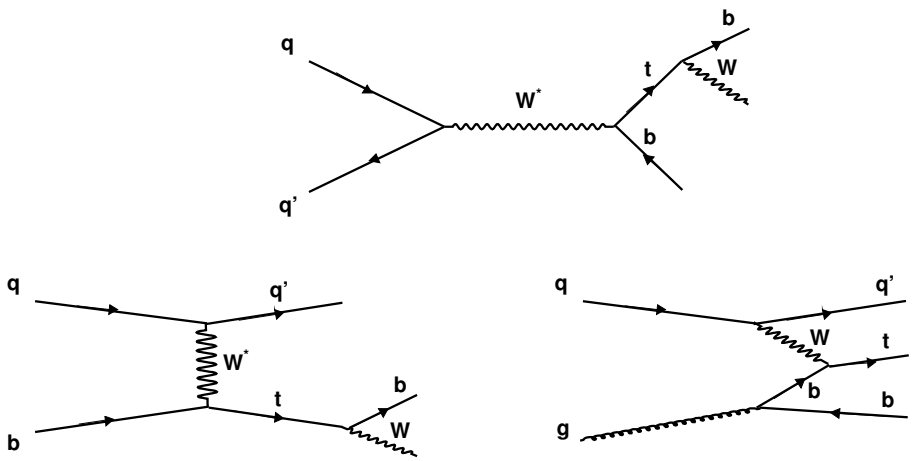

Figure 7.2: The s-channel and t-channel single top production mechanisms. The s-channel process is more relevant in the double tag sample, as it has the same final state as WH.

Single top Monte Carlo includes only events in which the W decays leptonically. Two single top processes, s-channel and t-channel, will contribute to the single tag data samples. Single top in the double tag samples is likely to consist mostly of s-channel, due to the fact that one of the b jets in t-channel events is typically at large

rapidity and not taggable. Monte Carlo for these processes were generated with with MadEvent [34] with PYTHIA [33] providing the showering.

7.1.3 Diboson

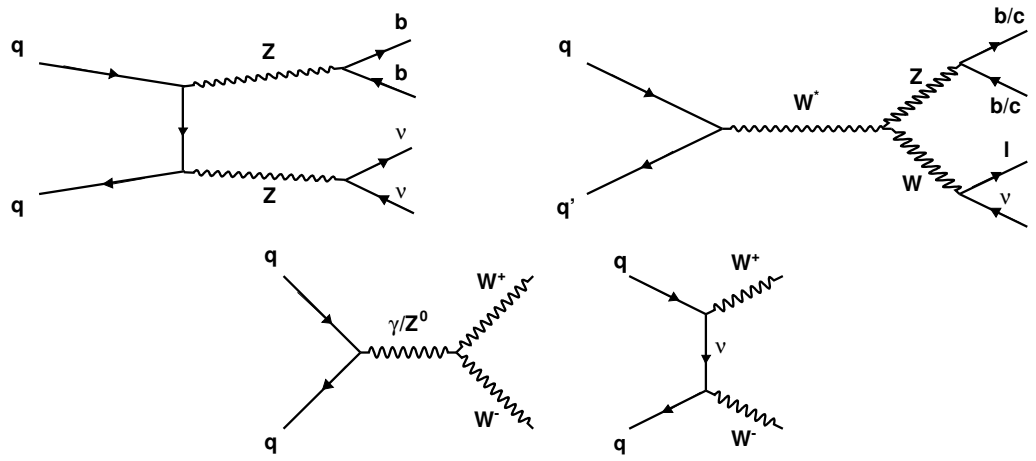

Figure 7.3: Examples of diboson production at the Tevatron.

Diboson events include ZZ,WZ and WW production. The physics of these events are very similar to the signal, as they both involve the decay products of bosons recoiling off of one another. The Monte Carlo diboson samples include all decay channels, although the majority of double tag events accepted involve WZ$\rightarrow l\nu b\bar{b}$ and ZZ$\rightarrow \nu\nu b\bar{b}$ events. These samples were generated with PYTHIA.

7.1.4 W/Z + Heavy Flavor

Events in which a W or Z boson is produced in association with heavy flavor partons are the largest background component next to heavy flavor QCD and mistags in

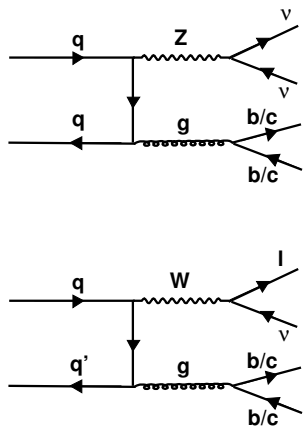

Figure 7.4: Examples of processes resulting in a vector boson plus heavy flavor quarks

the single tag sample. Models for these backgrounds are developed using a large number of different Monte Carlo samples, generated by ALPGEN [35] with PYTHIA [33] providing the showering. Z→ $\nu\nu$+bb/cc+np samples and W samples were generated for multiple processes containing different numbers of partons produced in the main physics process. Single and double tag shapes for these processes are developed by adding each parton sample weighted by its generated cross section and efficiency for passing event selection.

$$w_{np} = \sigma(gen) * \epsilon \tag{7.1}$$

Once the contributions from all parton samples have been normalized with respect to one another, an overall normalization is calculated for the total amount of integrated luminosity in the data. This normalization is scaled from the Method II predictions developed in CDF Run I [36]. Using the same W+bb+np Monte Carlo samples, the weighted acceptance calculations above are summed for the present selection criteria as well as the Method II selection criteria. The ratio of these provides a scaled

efficiency. Finally, the W+h.f. background is predicted by scaling the Method II prediction by the efficiency ratio as well as the ratio of integrated luminosity in the two analyses.

$$N_{MET+Jets} = \frac{Lum_{data}}{Lum_{MII}} * \frac{\epsilon_{MET+Jets}}{\epsilon_{MII}} * N_{MII} \tag{7.2}$$

The Z+bb/cc+np background is also scaled for the Method II expectation in a similar fashion, accounting for the differences in cross section and branching ratio.

7.2 Data Driven Models

7.2.1 QCD Model

The largest background to Higgs signal in this analysis is QCD multi-jet production. Mismeasured jets and semileptonic decay can produce large amounts of missing transverse energy in the detector, mimicking a Higgs-like signature. Previous studies have shown that hundreds of millions of heavy flavor events must be simulated in order to gather enough statistics to model this background with Monte Carlo events. Therefore, the background model for this process is produced directly from the data. After the standard event selection has been applied, the 1 tight tag data sample is used as the base of our QCD model. This data sample is comprised mostly of QCD jet production, but also includes contributions from other physics processes. In particular, light flavor processes which have been mistagged contribute approximately 30% to this data set in the signal region. Real heavy flavor top and electroweak processes also contribute to this data sample. The shapes of these other events must be subtracted from all relevant distributions at their expected normalizations, which are shown in Table 7.2. In addition, the untagged jet has been weighted to compensate for biases introduced by tagging. This procedure has been tested in the QCD dominated region

outlined in section 8.1. While the kinematics are different when the Missing E_T is not aligned with either jet, the procedure of developing a double tag QCD model from single tag data has been validated within the systematic uncertainties assigned to the model.

The normalization of our QCD model is allowed to float in all fits performed. The heavy flavor QCD in comparison plots between data and our background model is normalized to the data minus all other background expectations for the purpose of shape comparisons. It is critical that the shapes of our QCD model are accurate for the fitting procedure utilized to set limits in the double tagged data samples. Many comparisons are made in 3 separate tagging categories in the signal region, as well as in the QCD dominated region. We find that this data based model appropriately reconstructs the physics of heavy flavor QCD within the systematic uncertainties assigned to it. The details of this study are contained in section 8.1.

7.2.2 Mistags

In addition to the heavy flavor backgrounds expected in our signal samples, there is an additional contribution expected from light flavor jets that are mistagged. The shapes and normalization of these events are derived from the data before tagging requirements are implemented by applying the Mistag Matrix[37][38] to all relevant events. Negative tags, or jets in which the secondary vertex appears to travel toward the primary vertex, are used to make predictions regarding positive light flavor mistags. The Mistag Matrix utilizes several event and jet specific quantities to determine the probability that a light flavor taggable jet will be mistagged. The quantities utilized are displayed in Table 7.1.

1	Jet E_T
2	Jet η
3	# of silicon tracks in Jet
4	ΣE_T of all Jets
5	# of z vertices
6	Primary vertex z position

Table 7.1: *Quantities utilized by the Mistag Matrix*

After applying the Mistag Matrix, a weight is assigned to each taggable jet in a particular event. Therefore, our model is constructed from the Pretag data by weighting events according to their mistag probability. Single tag weights are the sum of taggable jet probabilities from the Mistag Matrix of both jets for a given event. Due to the probabilities calculated by SecVtx and Jet Probability mistag matrices being correlated, this is compensated for on an event-by-event basis for double tagged events. Since double SecVtx events are selected first, tight SecVtx mistag probabilities are multiplied for the lead and second jet to produce a double mistag probability. In tight SecVtx plus Jet Probability events, the event mistag weight is calculated as follows:

$$P_{event} = P_{Jet1}^{SECVTX} * P_{Jet2}^{JetProb} * (1 - P_{Jet2}^{SECVTX}) + P_{Jet2}^{SECVTX} * P_{Jet1}^{JetProb} * (1 - P_{Jet1}^{SECVTX}) \tag{7.3}$$

The mistag normalization is calculated as the sum of the respective probabilities in each tagging category.

7.3 Event Expectations

The total event yield in the data for different data samples is a mixture of the various backgrounds described in the previous section. Table 7.2 displays the expectations for these processes in 1.7 fb^{-1}. As previously stated, the heavy flavor QCD background is allowed to float when fitting for a Higgs signal. In addition to our final tagging categories, we include an additional data sample of exclusive single loose SecVtx tags for validation of the falsely b-tagged light flavor background.

Background	1 Loose Tag	1 Tight Tag	Vtx + Prob Tag	2 Vtx Tag
$t\bar{t}$	6.1 ± 0.8	21.6 ± 2.7	8.1 ± 1.5	8.2 ± 1.3
single top	4.3 ± 0.6	18.4 ± 2.5	4.5 ± 0.8	4.7 ± 0.8
WZ/WW	3.6 ± 0.5	6.6 ± 0.9	1.4 ± 0.3	1.2 ± 0.2
ZZ	1.8 ± 0.3	3.9 ± 0.5	2.0 ± 0.4	2.3 ± 0.44
W+h.f.	19.5 ± 8.0	53.7 ± 21.6	8.8 ± 3.8	6.9 ± 2.9
Z+h.f./Z$\rightarrow \tau\tau$	17.9 ± 7.3	44.4 ± 18.1	8.2 ± 3.6	8.0 ± 3.4
Mistags	294.3 ± 53.4	214.9 ± 24.5	8.3 ± 2.4	1.5 ± 0.3
Total non-QCD h.f.	343.8 ± 54.3	363.5 ± 37.0	41.3 ± 6.0	32.9 ± 4.8
Data	427	702	62	48

Table 7.2: *Event expectations for background processes after event selection. The difference between the total expectation and data is due to heavy flavor multi-jet QCD, which is fit to data.*

Background	1 Loose Tag	1 Tight Tag	Vtx+Prob Tag	2 Vtx Tag
$t\bar{t}$	0.053%	0.182%	0.081%	0.074%
s-chan top (W$\rightarrow l\nu$)	0.401%	1.230%	0.91%	0.099%
t-chan top (W$\rightarrow l\nu$)	0.231%	1.186%	0.10%	0.028%
WZ	0.044%	0.081%	0.024%	0.020%
WW	0.002%	0.004%	$> 0.001\%$	$> 0.001\%$
ZZ	0.032%	0.007%	0.031%	0.032%
W$\rightarrow \mu\nu$+bb	0.030%	0.120%	0.031%	0.027%
W$\rightarrow \tau\nu$+bb	0.046%	0.173%	0.048%	0.036%
W$\rightarrow e\nu$+bb	0.017%	0.069%	0.017%	0.014%
W$\rightarrow \mu\nu$+cc	0.023%	0.041%	0.006%	0.001%
W$\rightarrow \tau\nu$+cc	0.011%	0.053%	0.011%	0.002%
W$\rightarrow e\nu$+cc	0.010%	0.021%	0.003%	0.001%
W$\rightarrow \mu\nu$+c	0.040%	0.031%	$> 0.001\%$	$> 0.001\%$
W$\rightarrow \tau\nu$+c	0.011%	0.009%	$> 0.001\%$	$> 0.001\%$
W$\rightarrow e\nu$+c	0.010%	0.011%	$> 0.001\%$	$> 0.001\%$
Z+bb	0.071%	0.258%	0.082%	0.083%
Z+cc	0.032%	0.060%	0.009%	0.002%

Table 7.3: *Selection efficiency for various background processes.*

CHAPTER 8

CONTROL REGIONS

8.1 QCD Control Region and Data-Based Modeling

The largest class of events passing trigger requirements in the $\not\!\!E_T$ +Jets data sample involve dijet events in which the Missing E_T is aligned with the second jet. The missing energy in these events can be generated by severe mismeasurement of one of the jets, or by neutrinos and/or muons generated in semileptonic decays of heavy flavor hadrons. The $\not\!\!E_T$ is required to be within 0.4 radians ($\approx 23^o$) of the second jet, while all other event cuts which define the signal region remain the same. The motivation of this control region is to understand the ability to model heavy flavor QCD processes using data, and to apply appropriate systematic uncertainties on the shapes of kinematic and topological distributions which can be propagated into the signal region. Since 50 GeV of $\not\!\!E_T$ must be generated along the second jet, this particular region consists of highly energetic jets which are mostly back-to-back. In addition, light flavor QCD processes tend to be more energetic than heavy flavor, leading to shape differences between events with true heavy flavor tags and those which consist of mistags. We therefore use the single tight SecVtx data as the base of our heavy flavor QCD model. This particular data sample is highly susceptible to instrumental effects, such as cracks in the detector. Figure 8.1 displays the excess

of events caused by the chimney region and 90 degree crack. While the chimney region is removed for all data, events with $|\eta| < 0.1$ are removed only in the region in which the Missing E_T is aligned with the second jet. These cuts remove the two most obvious instrumental sources of $\not\!\!E_T$ when making data to model comparisons in the QCD dominated region.

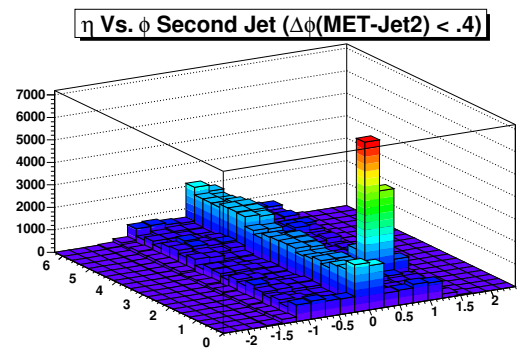

Figure 8.1: η vs. ϕ in region where $\not\!\!E_T$ is aligned with the second jet. Instrumental regions such as the chimney and 90 degree crack show large excesses of events in the Pretag data.

8.1.1 Shape Subtraction and Event Weighting

To model double tagged heavy flavor QCD using single tag data, there are some effects which must be accounted for to successfully reproduce relevant distributions. The efficiency of tagging a real heavy flavor jet changes as a function of jet E_T,η, and number of vertices, producing jets that tend to be more central than those in which no tagging requirements are made. The efficiencies for tagging a jet as a function of E_T, η and number of vertices is shown in figure **??**.

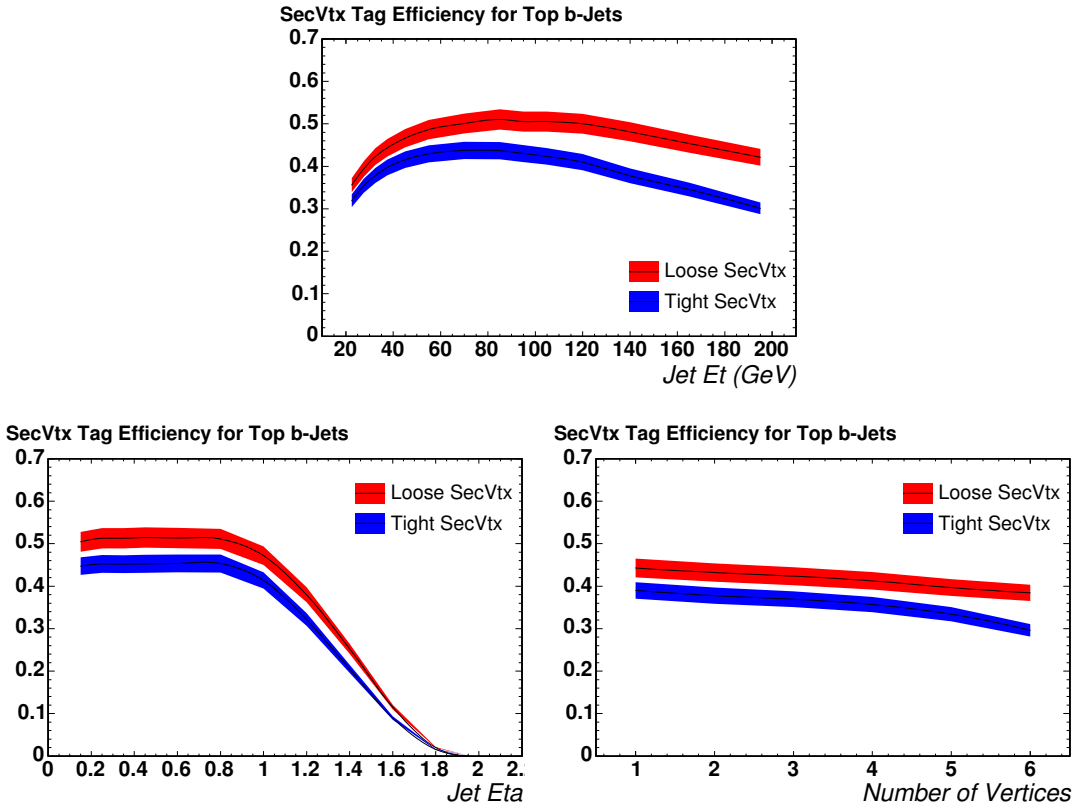

Figure 8.2: Tagging efficiency as a function of E_T, η and number of vertices.

The efficiency for tagging a jet peaks around a jet E_T of 60 GeV and is lower for less or more energetic jets. This can be compensated for by parameterizing these tagging efficiencies, and weighting single tag events appropriately. On an event-by-event basis, the jet E_T and η of the untagged jet in the single tag data sample is utilized to produce a weight which is the product of tagging efficiencies for that particular jet, as well as the number of vertices in the event. We apply this weighting scheme to produce a heavy flavor QCD model in the double tight SecVtx data. In the Tight SecVtx plus Jet Probability sample, we find that no weighting is necessary as a function of Jet E_T, as these distributions are well modeled within systematic uncertainties.

Therefore, a separate model is built for this data sample with only vertex and η efficiencies utilized. The parameterizations have been calculated from top quark b jets. The single tag data sample also contains a large amount of mistagged light flavor events which must be removed to produce pure heavy flavor shapes. Therefore, the shapes of mistagged light flavor events are subtracted out of the single tag data at their predicted normalization. The resultant shape is used to model double-tagged heavy flavor processes in the region where the $\not\!\!E_T$ is aligned with the second jet. A modified version of this technique is applied in the signal region, where contributions from heavy flavor top and electroweak processes must be subtracted from the data in addition to mistags.

Data Sample	Event Count	Mistag Prediction
2 Tight SECVTX Tags	1248	52.2 ± 12.0
1 Tight SECVTX Tag + 1 Loose Jet Prob	2113	254.6 ± 121.1
1 Tight SECVTX Tag	14035	4620.5 ± 779.5
PreTag	110018	N/A

Table 8.1: *Events accepted as well as mistag predictions in the region in which Missing E_T is aligned with the second jet.*

8.1.2 Estimation of Light Flavor QCD

While requiring two secondary vertex tags greatly reduces the amount of light flavor present in a data sample, some percentage of falsely tagged light flavor events remain. The mistag matrix, which uses jet and event information to determine a probability that a jet is a mistag, is utilized to determine the shape and normalization

of the light flavor contribution to a tagged sample. Past analyses have used two different methods to model light flavor background in a double tag sample.

- The first method uses a single tagged data sample and applies the mistag matrix to the untagged jet. This technique attempts to predict the shape and normalization of events with two mistagged jets, and events with one real heavy flavor tag and a mistagged light flavor jet. However, the enhancement of heavy flavor content due to starting with a previously tagged sample leads to an overestimation of the light flavor content, due to the fact that heavy flavor jets are more likely to produce negative tags. This can be compensated for by running the mistag matrix on heavy flavor Monte Carlo to predict the amount of heavy flavor falsely categorized as mistagged.

- The second method uses a pretagged data sample by applying the mistag matrix to both jets in each event. Multiplication of mistag weights is then used to predict the light flavor content in a double tag data sample. Pretag data is heavily dominated by light flavor physics processes, and any overestimation of double mistagged events due to heavy flavor is negligible.

Applying the mistag matrix to the untagged jet in a single tag sample increases the predicted light flavor content by a large amount. The effects of heavy flavor in the single tag sample on the mistag prediction cannot be quantified in a data based analysis, but it is expected to be a large effect given the differences in negative tag categories displayed in table 8.2. The effect of heavy flavor jets in data sample appears to greatly increase the number of negative tags, as the number of negative tags found after a positive vertex has been measured is much greater than when both jets are

negatively tagged. Studies of distributions in the region in which the $\not\!\!E_T$ is aligned with the second jet show the best agreement by utilizing the latter of the previously mentioned mistag techniques. This mistag convention is adopted for all remaining analysis.

Data Sample	2 Negative Tags	Positive Tag + Negative Tag
SecVtx Tag + Jet Probability	231	1426
Double SecVtx Tag	27	257

Table 8.2: *Amount of negative tags observed in region where missing E_T is aligned with second jet. Table displays both the number events with 2 negative tags, and single tight SECVTX events in which the other jet was negatively tagged.*

8.1.3 Heavy Flavor QCD Systematic Uncertainties

The utilization of a data-driven model requires the development of unique systematic uncertainties to properly ascertain the ability to model heavy flavor QCD shapes. After careful studies, the following systematics are found to be most appropriate.

- Separate systematic shapes are developed by varying the single mistag shape and normalization within its uncertainty. Two systematic QCD models are built with these shapes subtracted out of the single tag data varied by the uncertainty($\pm$) on the normalization.

- Tagging efficiencies as a function of η and P_T are varied within their uncertainties for untagged jets in the single-tagged data.

- Separate heavy flavor models are developed for single tag events in which only the lead jet is tagged, and when only the second jet is tagged. This systematic

is developed to compensate for any additional tagging efficiencies or differences in kinematics between single and double tag samples.

These sources of uncertainty are combined by calculating the deviation from the nominal model for all systematics bin-by-bin, and adding these values in quadrature. This error is then divided in half and symmeterized. In addition, due to the nature of data based systematics, which can be prone to statistical fluctuations and regions where errors are over or underestimated, we apply a smoothing technique to compensate for these effects. A running 3-bin algorithm is utilized. Starting from the first bin of a given histogram, the average systematic error of the first three bins is calculated. The error of the middle bin is set to this value. This process is continued by shifting over one bin and repeating the same process. This process is found to be sufficient in producing reliable systematic uncertainties. Figures 8.3 and 8.4 display data to model comparisons for useful kinematic quantities used relevant to this analysis. More event variables can be found in Appendix A The heavy flavor QCD is normalized to data in these plots for the purpose of shape comparisons. The black hashes represent the uncertainty on the background model.

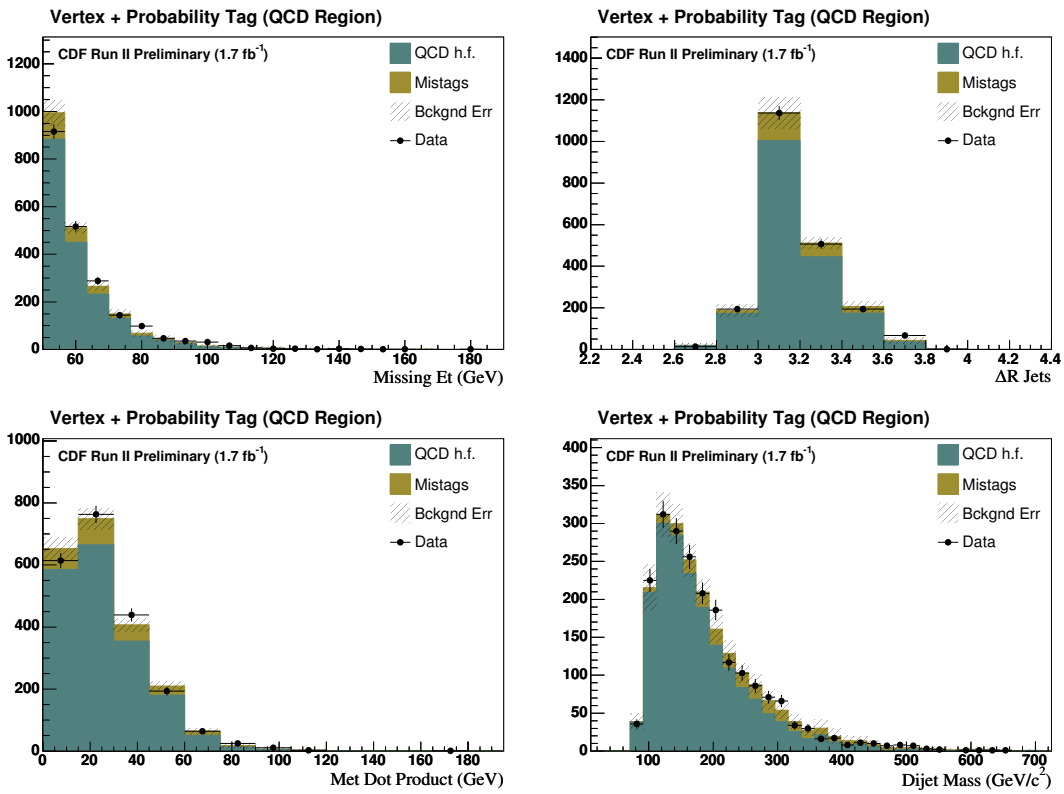

Figure 8.3: Event variables in region where missing E_T is aligned with second jet. Black hashes represent the total systematic and statistical error of background model. Data consists of events with 1 tight SECVTX and 1 Jet Probability tagged jet. Upper left: Missing E_T; upper right: ΔR Lead-2nd Jet; lower left: Dot product of track and calorimeter MET; lower right: Dijet mass.

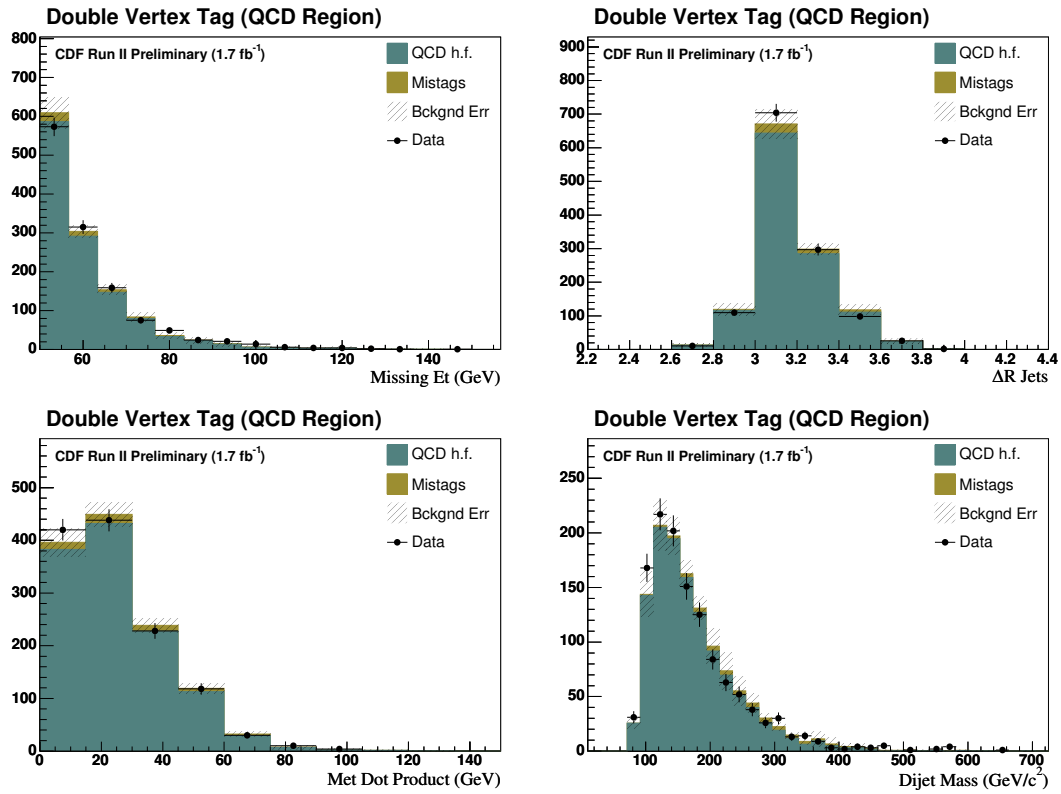

Figure 8.4: Event variables in region where missing E_T is aligned with second jet. Black hashes represent the total systematic and statistical error of background model. Data consists of events with 2 tight SECVTX tagged jets. Upper left: Missing E_T; upper right: ΔR Lead-2nd Jet; lower left: Dot product of track and calorimeter Met; lower right: Dijet mass.

8.2 Electroweak MC control regions

In the signal region where the $\not\!\!E_T$ is not aligned with either jet, backgrounds with high $\not\!\!E_T$ arising from W+jets, Z+jets, $t\bar{t}$, and diboson production are anticipated. The Missing E_T can arise due to unidentified leptons as well as real neutrinos from $W \to \ell\nu$ and $Z \to \nu\nu$. Processes with muons contribute especially since their minimum ionizing energy leaves a Missing E_T signature in the calorimeter, which would not be accounted for if the muon was not identified, and its muon P_T was not used to correct the $\not\!\!E_T$.

While we reject events with tight and loose leptons in order to minimize the background, some contribution of this background remains. Additionally, Z+ b-quark jets with $Z \to \nu\bar{\nu}$ and $ZZ \to \nu\bar{\nu}b\bar{b}$ will also be present.

Cross-checks of the modeling of these backgrounds in our signal region can be performed using an electroweak Monte Carlo control region. In this region, all of the same kinematic cuts are imposed as is done in the Higgs signal selection, however, the presence of at least one "tight" muon is required, where tight only includes CMUP and CMX muons. The P_T of the muon is not used to correct the $\not\!\!E_T$, which simulates the effect on the $\not\!\!E_T$ of not identifying the muon. In this control region, since the $\not\!\!E_T$ cut is 50 GeV, there is essentially no QCD background resulting from fake leptons. This QCD estimate has been calculated in previous WH analyses, which uses a similar event selection. Although there is about a 20% QCD contribution to the WH event selection for one or more b-tags, the event yield falls quickly as a function of $\not\!\!E_T$. Above 50 GeV, the QCD background is less than a few percent. In addition, approximately 75% of the QCD background involves electron events. Therefore, the region can be fully modeled using Monte Carlo (other than mistags). If there were a

significant amount of QCD in this region, it would likely appear as an excess in the low Missing E_T bins of the $\not\!\!E_T$ distribution, which is testable.

This control region makes several important crosschecks. It tests whether the $\not\!\!E_T$ trigger turn-on curve is modeled properly in Monte Carlo, and whether event event selection criteria avoid trigger inefficiencies due to the jet E_T trigger turn-on curves. It tests the normalization for Monto Carlo processes as well by making comparisons of the number of expected events with observed events. It tests our modeling of kinematic distributions used for our Neural Network. The data - MC comparison is shown in Table 8.3. The systematic uncertainty has been calculated as at least 13.4% from normalization uncertainties. However shape based systematics such as jet energy scale and trigger uncertainties have not been evaluated for these events. The data - MC normalization has reasonable agreement. There is a slight excess of data, which is covered by the low side estimate of the uncertainty.

Comparisons of distributions utilized in the analysis for this control region are displayed in figure 8.5. The amount of data collected in this control region is approximately 14% higher than the prediction of the Monte Carlo backgrounds. The background is normalized absolutely, so the data will tend to have an excess averaged over all the bins.

The statistics in this control region are low when requiring a b-tag, so the selection is also loosened to before the b-tag requirement. This sample is predominantly W+l.f. The Monte Carlo in the 'Pretag' sample is normalized to the data, and comparisons of jet 1 E_T, jet 2 E_T, and Missing E_T distributions show no signs of mismodeling from trigger turn-on effects, as seen in figure 8.6.

Sample	Number of events in 1.7 fb−1
Mistags	26.4 ± 3.0
$t\bar{t}$	22.1 ± 2.9
W+bb	15.3 ± 6.1
Wc	7.8 ± 3.1
W+cc	5.8 ± 2.3
$Z \to \tau\tau$	1.6 ± .6
WW	3.0 ± .4
Z+hf	2.9 ± 1.2
WZ	1.4 ± .2
ZZ	0.5 ± .1
Single-top s-channel	4.5 ± .6
Single-top t-channel	3.7 ± .5
Total Expected	94.5 ± 12.7
Observed	108

Table 8.3: *Electroweak MC control region defined as data passing all our cuts but also containing a high P_T muon. The uncertainties quoted on normalizations do not include JES and trigger systematics.*

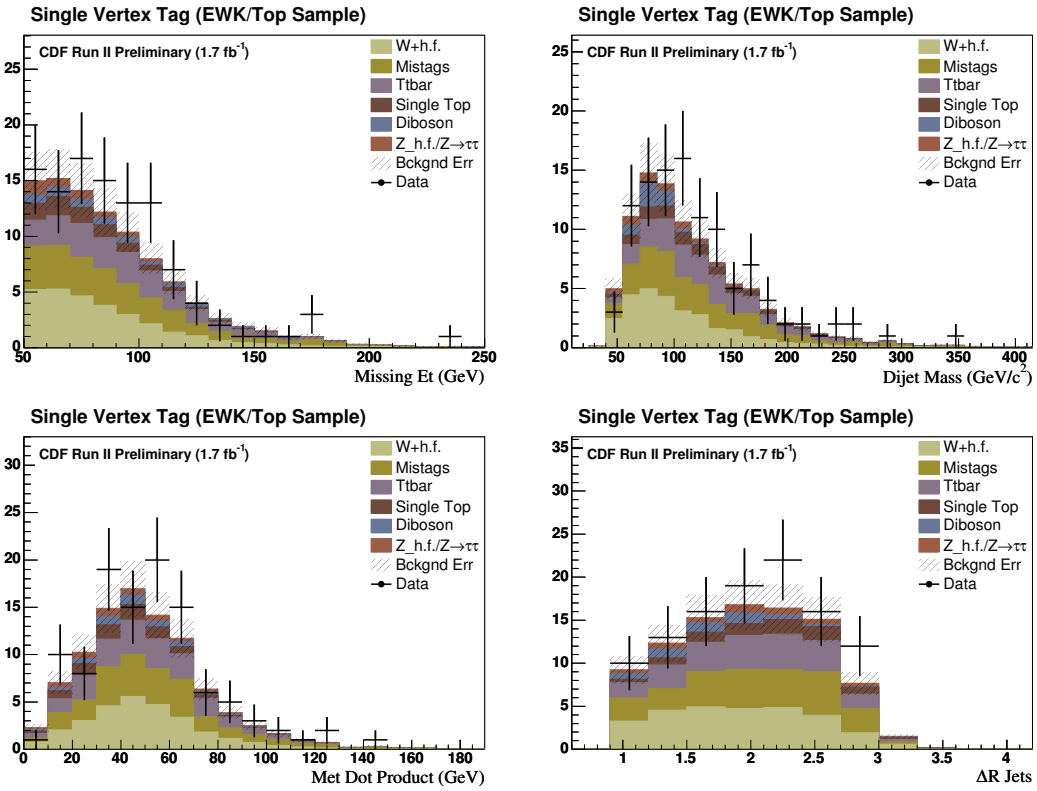

Figure 8.5: Event variables in events with an identified tight muon and at least one SecVtx tagged jet.. Black Hashes represent the normalization uncertainty on all backgrounds. Upper left: Missing E_T; upper right: Dijet Mass; lower left: Dot product of track and calorimeter Met; lower right: ΔR Lead-2nd Jet

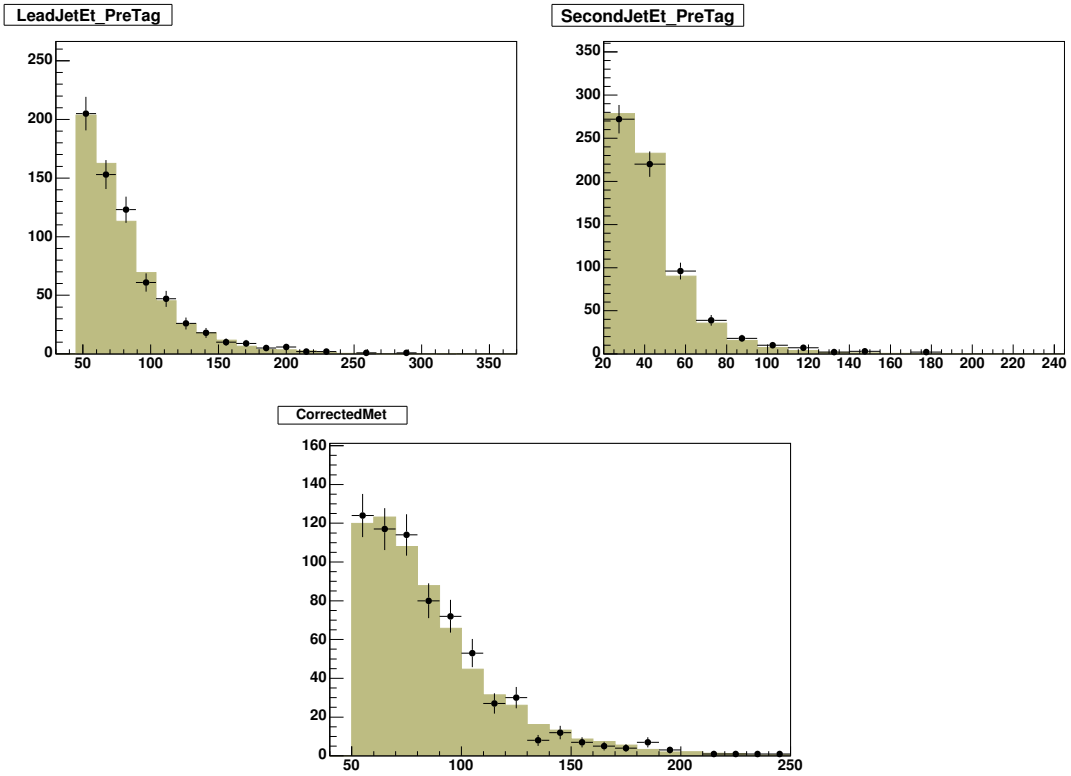

Figure 8.6: Agreement for pretagged electroweak MC control region. Expected background is W+l.f. and is normalized to data. Upper left: lead jet E_T; upper right: second jet E_T; lower : MET.

CHAPTER 9

ARTIFICIAL NEURAL NETWORKS

The difficult nature of Higgs analysis at the Tevatron is highlighted by a number of features. The low production cross-section is, of course the main difficulty. The limited amount of data to be collected in the full Tevatron dataset means only a handful of the highest quality Higgs events are likely to be available. As has been stated previously, the main backgrounds to Higgs all possess significantly greater production rates, making a counting experiment impossible. The third feature of Higgs analysis is that these backgrounds for the most part tend to look very much like a Higgs signal once reconstructed. Unlike analysis of top quarks, which tend to be much more energetic and discernible from its primary background, the multitude of different backgrounds, many of which display very similar kinematic features to the signal, dilute the ability to fit for a Higgs signal in with its most distinguishing feature, the reconstructed dijet mass. Therefore the development of artificial neural networks has been pursued to increase the potential for the isolation of a Higgs signal. Artificial neural networks have the advantage of evaluating an event globally with several variables, taking into account their correlations to provide a single number which indicates how signal-like or background-like an event is. Two separate neural

networks have been trained for different purposes in this analysis, enhancing the ability to reject background and possibly measure a Higgs signal.

9.1 Track Met and Track-based Neural Network

The largest backgrounds in the $\not\!\!E_T$ +jets dataset are the result of QCD processes with jet energies not being fully measured by the calorimeter. This leads to events with large calorimeter $\not\!\!E_T$ which can be mistaken for real electroweak processes which have high energy neutrinos. Since 60% of jet energy is in the form of charged particles, the Central Outer Tracker (COT) can provide an additional estimator of the $\not\!\!E_T$, by summing up the momenta of charged particles. This "trackMet" estimator should be uncorrelated to the calorimeter $\not\!\!E_T$ for events where there is not real $\not\!\!E_T$, and correlated for events where there is real $\not\!\!E_T$ from neutrinos. A new technique has been developed to discern real from fake $\not\!\!E_T$ using multiple track based quantities. An artificial neural network was trained to classify ZH signal events against untagged QCD data events. The inputs are based on the sum P_T of all tracks, the sum P_T of tracks originating from the primary vertex, the number of vertices, the missing P_T of the vector sum of the tracks, and the highest P_T track. Several versions of these quantities are calculated with different P_T cuts on the tracks, and different track selection requirements. The different P_T requirements provide more or less sensitive to the low P_T underlying event and extra interactions. The track selection cuts yield subsets of tracks that are cleaner or more central. The track-based NN discriminant is trained on our full signal selection, with a zero b-tag requirement. The network training was performed by MLPFit, combining these track based variables into a single function. The data sample is our full 1.7 fb^{-1} dataset. The Monte Carlo is 1

fb^{-1}, with the vertex multiplicity distribution re-weighted to match the data. The NN output shows excellent separation as is seen in Figure 9.1.

The track-based NN is validated in several high $\not\!\!E_T$ control regions : one dominated by electroweak processes modeled from Monte Carlo, one dominated by mistagged QCD dijets in the QCD control region, one using tagged QCD dijets in the QCD control region, one using untagged data in the signal region. More information about these control regions can be found in these respective sections of this dissertation. In Figure 9.2, the trackMet NN output is shown for events with the same kinematic requirements as the signal region. The pretagged electroweak control region validates a high statistics W+jets data sample. The tagged electroweak control region validates a lower statistics sample which has contributions from a variety of heavy flavor processes. The mistag control region requires a loose SecVtx tag, and does not require a muon, therefore it is dominated by QCD light flavor jets which are mistagged. Figure 9.3 displays the trackMet NN output for QCD control regions where the selection of objects is the same as our signal region, except that $\not\!\!E_T$ is aligned with the second jet. This is shown for two different double-tagged scenarios. Figure 9.4 displays the trackMet NN output for our signal region. This also shows excellent separation of mismeasured QCD events from the ZH signal. W events do not show as much separation from QCD events due to the fact that there is often a high P_T track that produces some amount of fake $\not\!\!E_T$. The utilization of this track-based discriminant is described in the next section.

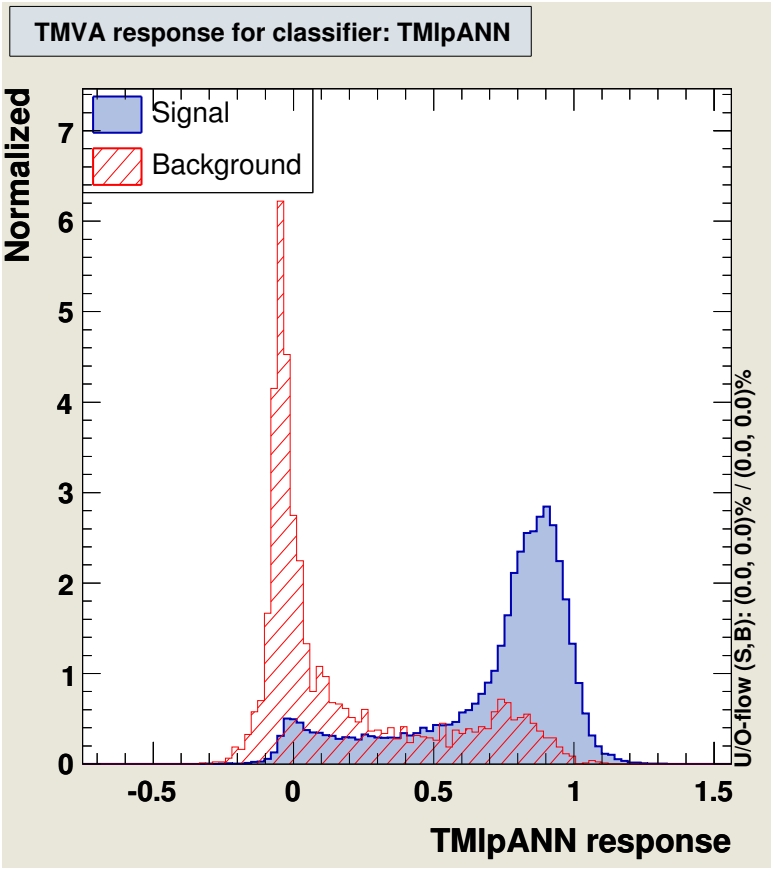

Figure 9.1: Track Met Neural Network Output from training NN to separate ZH signal from QCD background.

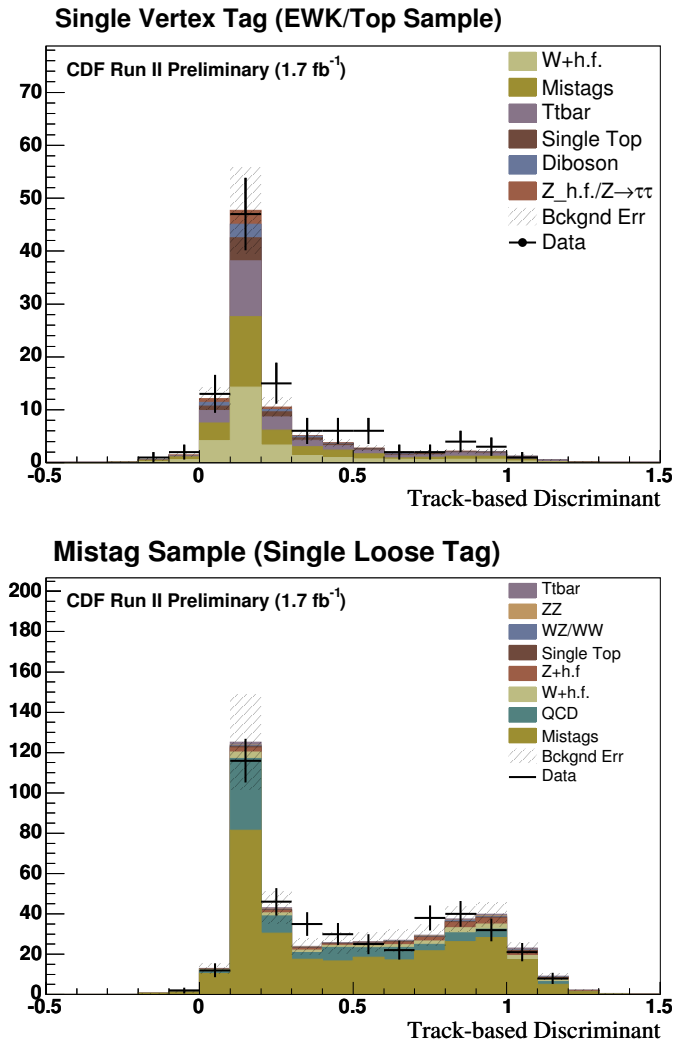

Figure 9.2: Track Met Neural Network Output for 2 different data sets. Top: Trackmet NN output for events in electroweak control region with 1 tight SecVtx tag. Bottom: Trackmet NN output for events with no leptons but with one loose SecVtx tag, and no tight tags.

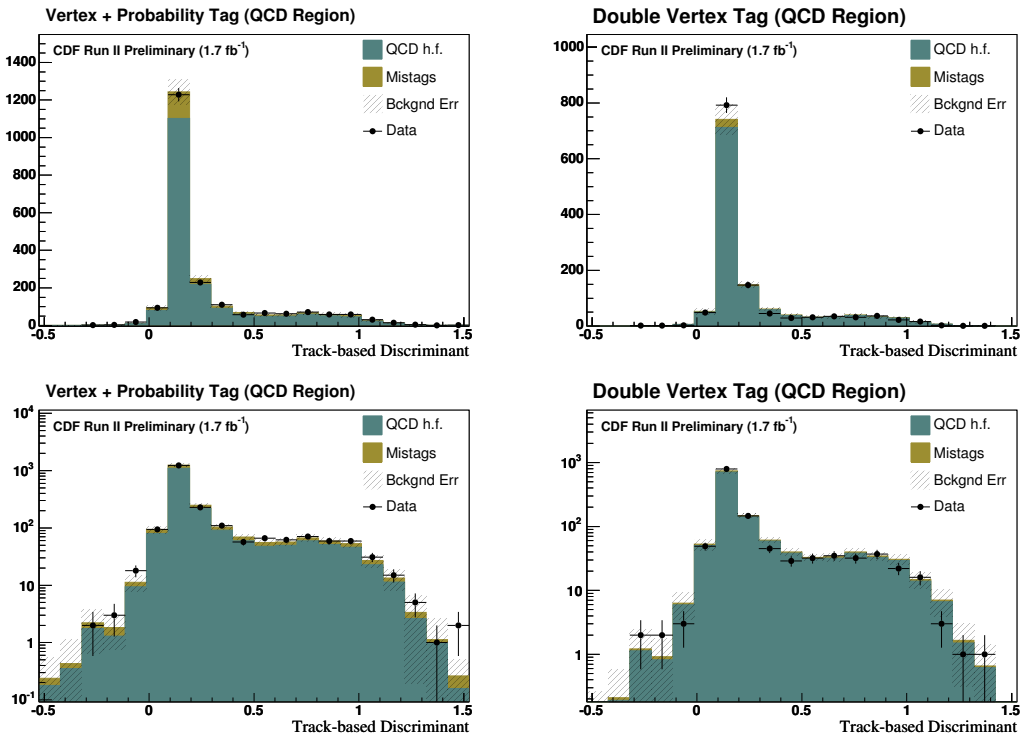

Figure 9.3: Track Met Neural Network Output in QCD control regions for both tagging categories. Black hashes represent the total systematic and statistical error of background model. On the left is the SECVTX + Jet Prob double-tagged category, shown on the bottom with a log scale. On the right is the SecVtx + SecVtx double-tagged category, shown on a log scale on the bottom.

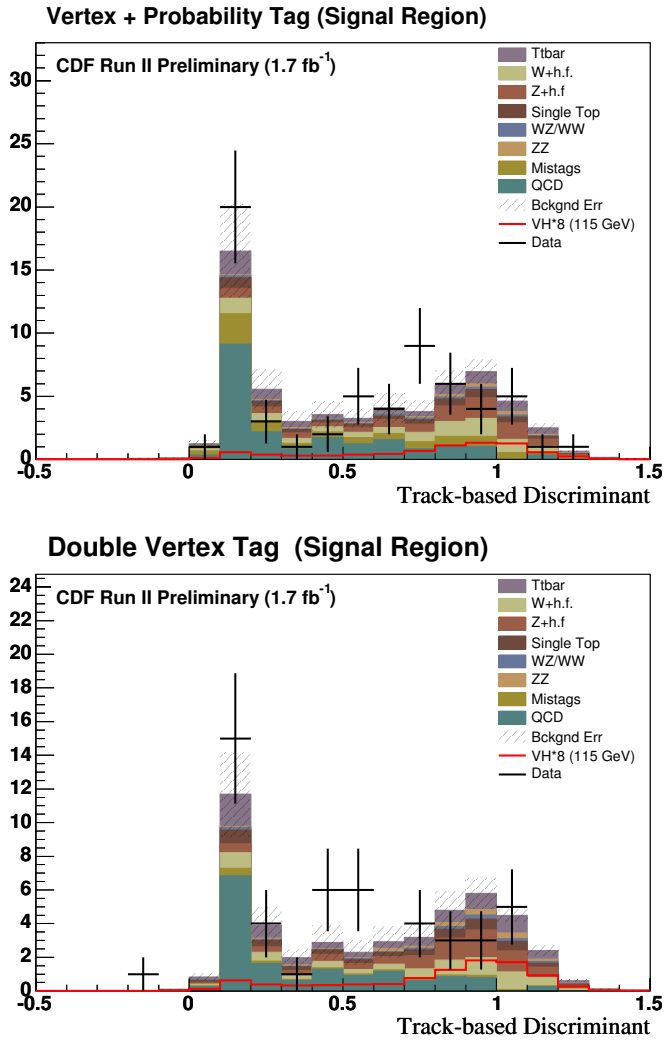

Figure 9.4: Track Met Neural Network Output for our two double-tagged signal regions. Top: SecVtx + SecVtx; bottom: SecVtx + Jet Prob.

9.2 Artificial Neural Network Discriminant

To take advantage of multiple kinematic and topological features of events in this analysis, an Artificial Neural Network has been developed as a discriminant. The utilization of a multivariate technique provides a means to loosen cuts compared to traditional mass fitting analyses. The loosening of cuts increases the amount of signal expected in this analysis, and additionally provides larger background statistics to take advantage of in fits of the neural network discriminant. Four different samples are used in the training process. A mixture of 40% $t\bar{t}$ and 60% untagged data is trained against 40% WH and 60% ZH. The untagged data consists largely of light flavor multi-jet QCD. Individual neural networks were trained for 115 GeV/c^2 Higgs mass and mass points between 110-150 GeV/c^2 at intervals of 10 GeV/c^2 to optimize the sensitivity over a range of possible Higgs masses. The neural network has been tested in control regions to verify that heavy flavor processes are successfully reproduced. An optimization study was performed with 9 event quantities to determine the best configuration for the neural network. [39] Neural network training is performed for each variable individually (1 input node), and the variable with the lowest training error is selected. The procedure is then repeated by training with the previously selected variable as well as each of the unselected variables in a 2 input node structure. Variables are continually added in this manner until an improvement in training error of less than 0.5% is observed. Nine event quantities were examined in this optimization procedure. They are listed below in the order in which they were selected.

- Variable 1 - The Invariant Mass of the Dijet System. (Input 1)

- Variable 2 - The Track-based discriminant (Track Met Neural Network) which distinguishes real from fake Missing E_T. (Input 2)
- Variable 3 - Missing Et corrected for the Level 5 Et of the Lead and Second Jet. (Input 3)
- Variable 4 - Dot Product of calorimeter based Missing E_T and resulting Missing P_T from the sum of event track momenta. (Input 4)
- Variable 5 - $|\Delta R|$ between the jets. (Input 5)
- Variable 6 - Lead Jet E_T. (Best unselected variable)
- Variable 7 - Second Jet E_T. (Not Selected)
- Variable 8 and 9 - Fox Wolfram Moments 1 and 2. Observables which characterize the shape of an event.[40] (Not Selected)

The neural network training was performed by JetNet using the RootJetnet [41] interface and consists of 5 input nodes, 5 hidden nodes and 1 output node. The neural network output of various processes are displyed in figures 9.5 and 9.6 Comparisons of the neural network output have been performed in the QCD dominated region as well as in muon data. Additionally, comparisons are made in the single loose tagged data. We find the output to be well modeled within systematic uncertainties. Figures 9.7-9.13 display input variables for the 3 signal region tagging categories, as well as the neural network output for the control regions.

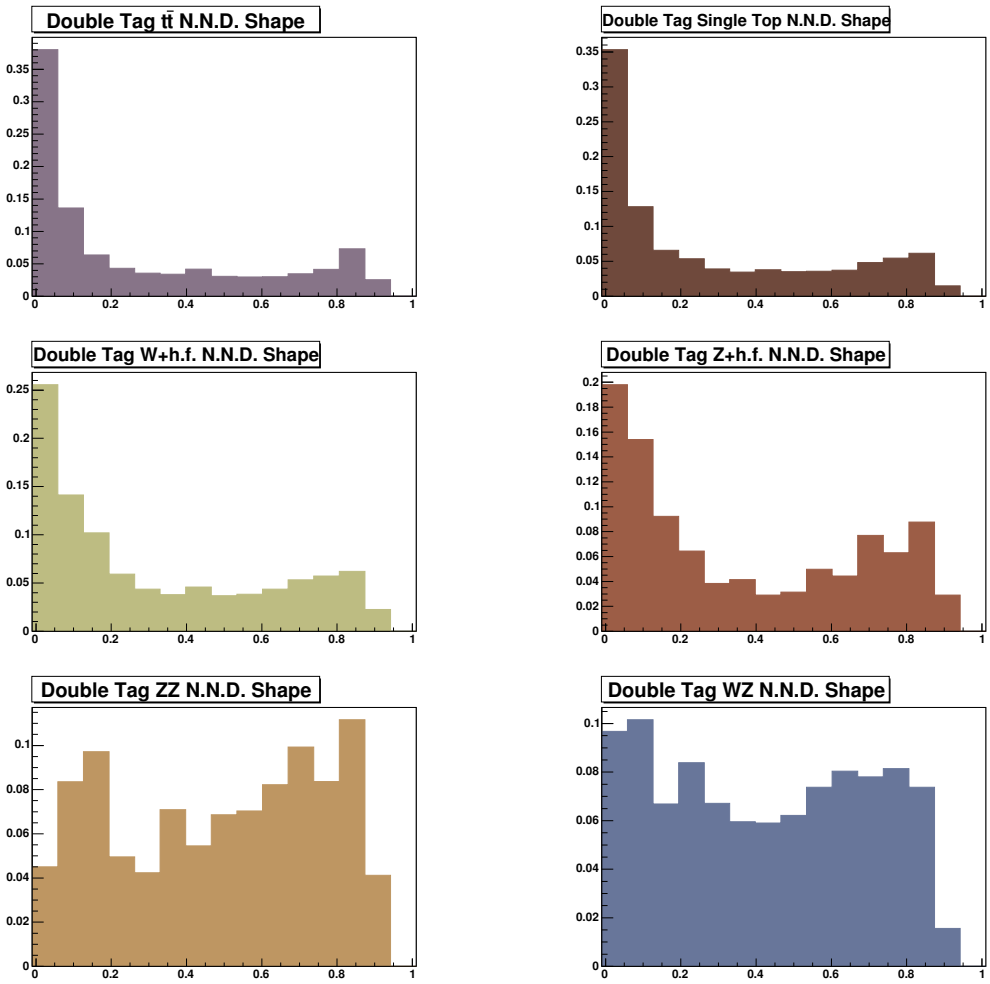

Figure 9.5: Neural network shapes for Monte Carlo background processes. The x-axis represents the output of the network, with events close to 1.0 categorized as signal-like and events close to 0.0 being background-like.

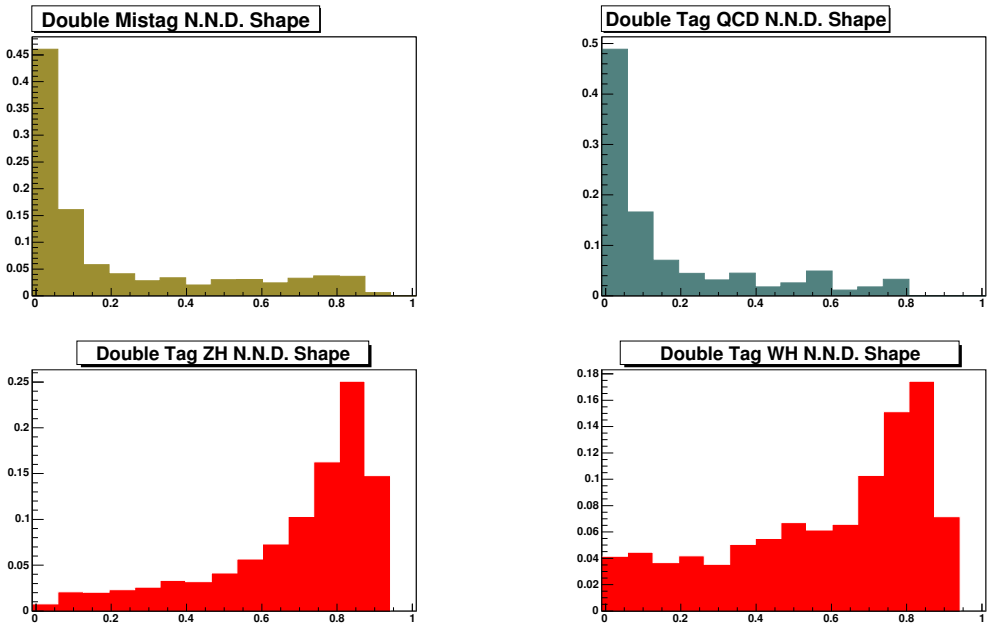

Figure 9.6: Neural network shapes for signal and data-based background processes. The x-axis represents the output of the network, with events close to 1.0 categorized as signal-like and events close to 0.0 being background-like.

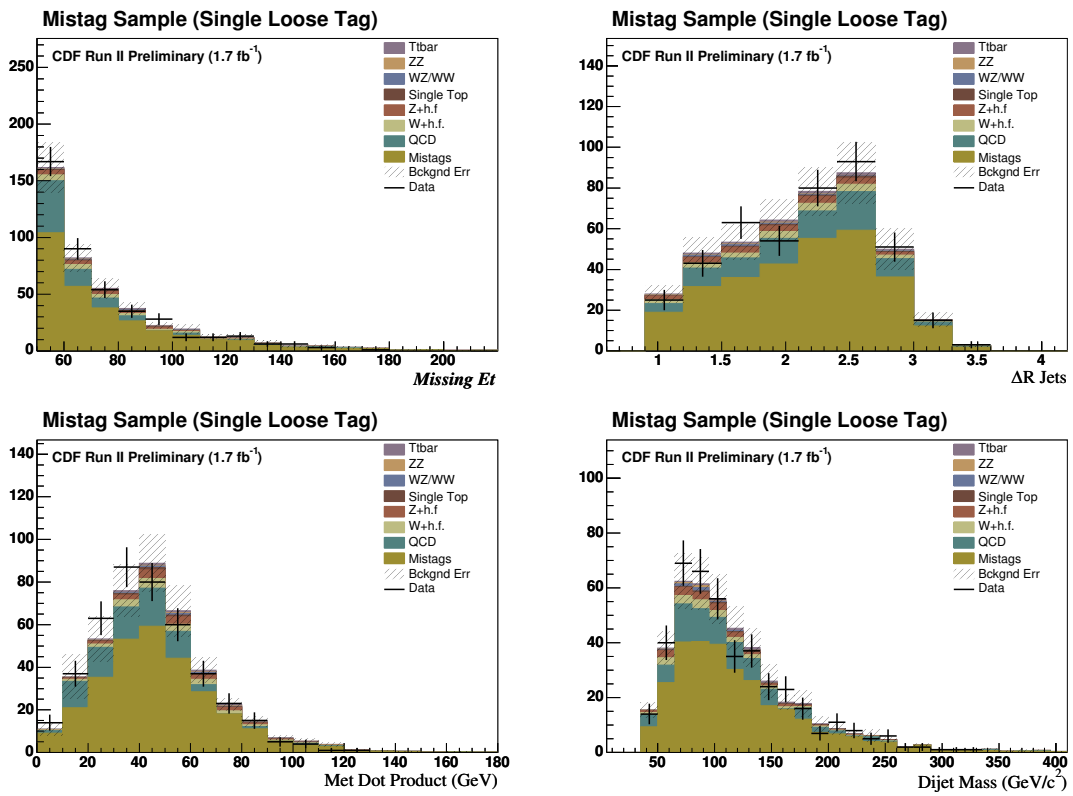

Figure 9.7: Figures for 1 loose tag in signal region. Error bands represent uncertainty on QCD model plus mistag uncertainty. Upper left: Missing E_T; upper right: ΔR Lead-2nd Jet; lower left: Dot product of track and calorimeter Met; lower right: Dijet Mass.

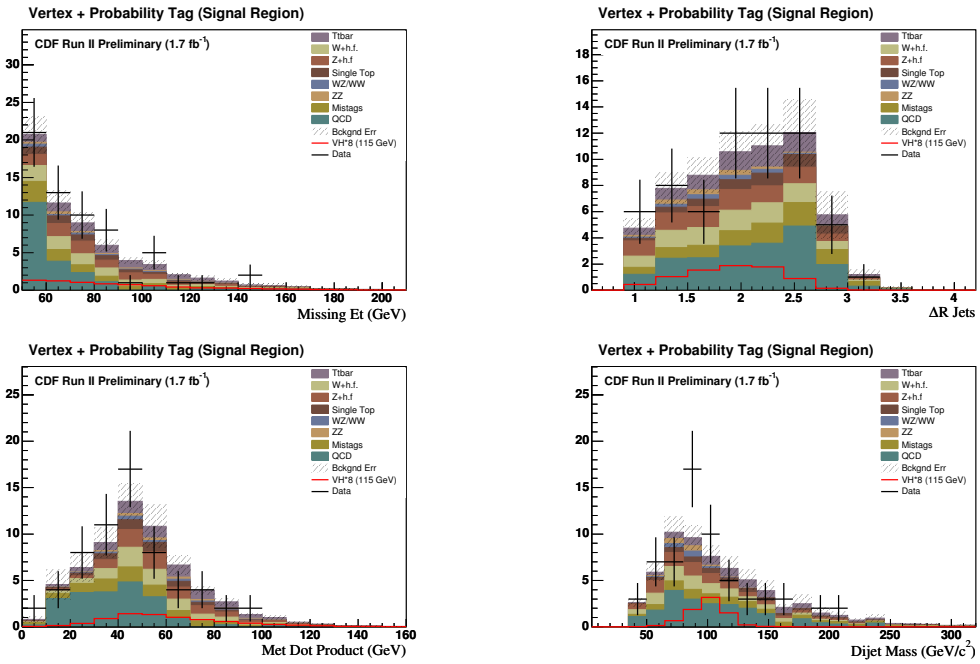

Figure 9.8: Figures for tight SecVtx + Jet Probability events in signal region. Error bands represent uncertainty on QCD model plus symmeterized JES uncertainty on Monte Carl backgrounds. Upper left: Missing E_T; upper right: ΔR Lead-2nd Jet; lower left: Dot product of track and calorimeter Met; lower right: Dijet Mass.

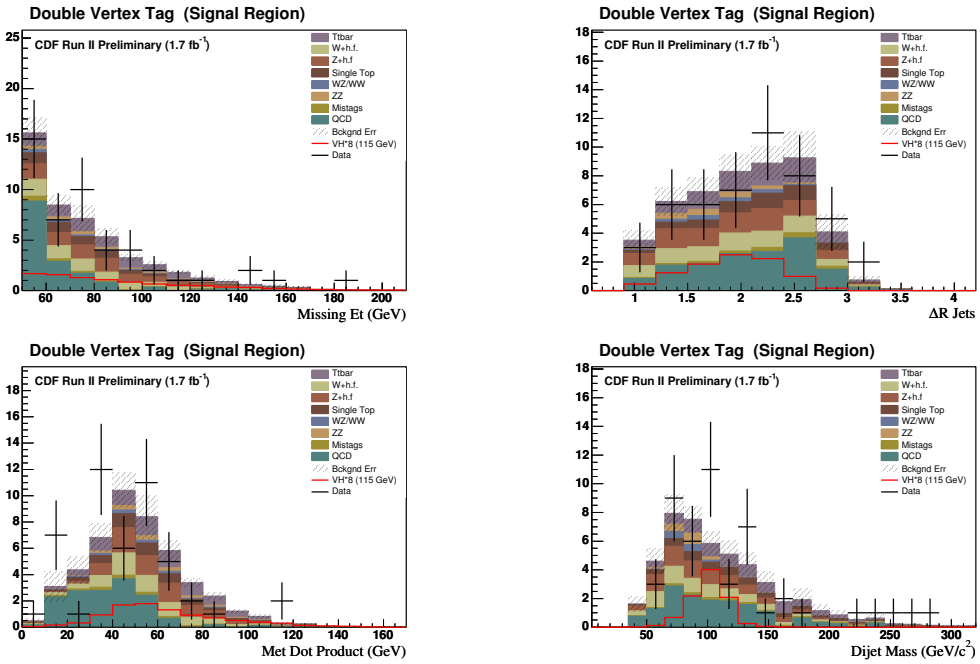

Figure 9.9: Figures for double tight SecVtx events in signal region. Error bands represent uncertainty on QCD model plus symmeterized JES uncertainty on Monte Carl backgrounds. Upper left: Missing E_T; upper right: ΔR Lead-2nd Jet; lower left: Dot product of track and calorimeter Met; lower right: Dijet Mass.

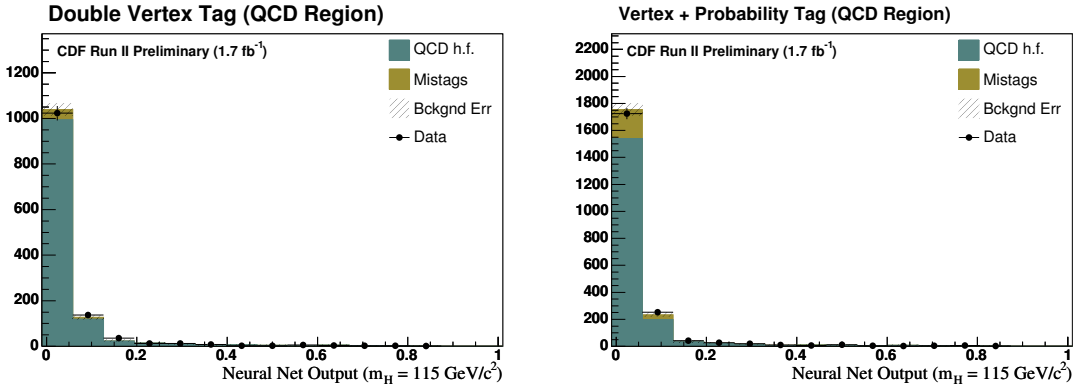

Figure 9.10: Neural Network Output in QCD control region. Black hashes represent the total systematic and statistical error of background model. Left: Double tight SecVtx tagged NN in QCD control region; Right: Tight SecVtx plus Jet Probability NN in QCD control region ;

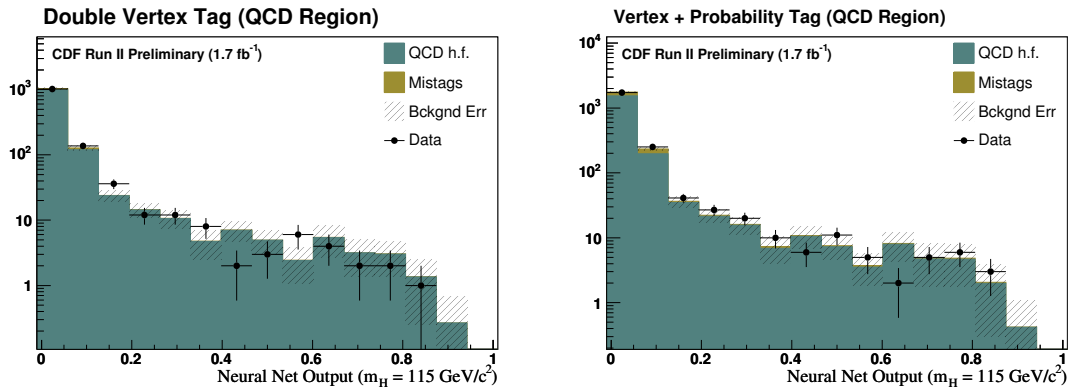

Figure 9.11: Neural Network Output on log scale in QCD control region. Left: Double tight SecVtx tagged NN in QCD control region; Right: Tight SecVtx plus Jet Probability NN in QCD control region ;

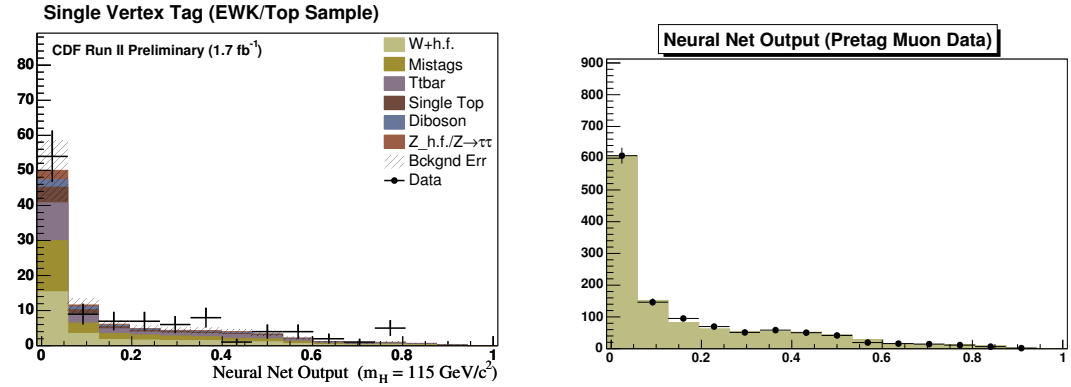

Figure 9.12: Neural Network Output for events with tight muon. Left: NN for inclusive single tagged events with identified muon ; Right: NN for inclusive Pretag events with identified muon ;

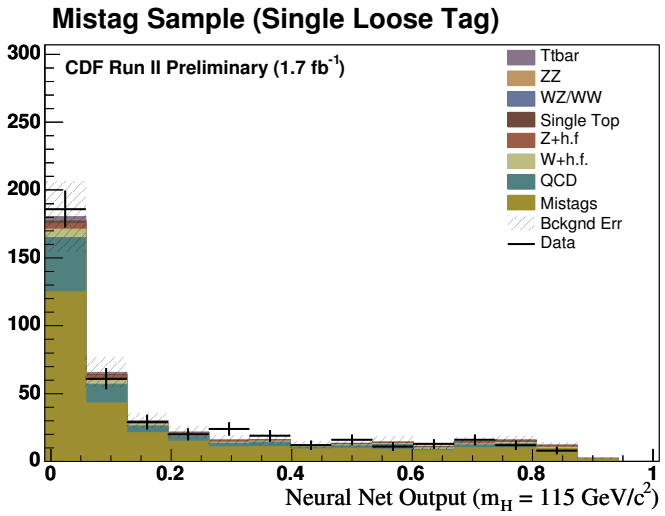

Figure 9.13: NN for single loose SecVtx tagged events in signal region.

CHAPTER 10

SYSTEMATIC UNCERTAINTIES

Due to imperfections in modeling the various physics processes in this analysis, we assign a number of systematic uncertainties. Our final discriminant is a one-dimensional Artificial Neural Network output, for which have distributions for a range of MC-based and data-based contributions to the data sample. The normalization and shape are fluctuated for these distributions according to which contribution is expected to be affected by the given systematic.

- In Monte Carlo based models, there is an uncertainty associated with the scale of jet energies. To account for this, a shape systematic has been developed by shifting the jet energy scale of all Monte Carl up and down by one sigma. Higher E_T jets will increase the jet multiplicity for a given E_T cuts, resulting in more 2-jet events, but also possibly rejecting events due to the 3-jet veto. Also, since $\not{E}_T$ is corrected due to the difference between raw and corrected jets, events may be promoted or demoted to the signal region due to the $\not{E}_T$ cut. Since there are competing effects, propagation of both up and down jet energy scale uncertainties into the Neural Network are performed separately, without symmetrizing them. The acceptance change and shape change are both considered in the systematic model of the Neural Network distribution.

- An uncertainty in the calculated luminosity for Monte Carlo based processes leads to a change in event yield of ± 6% [42].

- A 2% uncertainty in acceptance is assigned to the Parton Distribution Fuctions (PDF's) of Monte Carlo models. Since this is a relatively small uncertainty, the systematics from existing studies which have evaluated the uncertainty on backgrounds and signal [43] are used.

- A 40% uncertainty is assigned to the normalization of the W and Z plus heavy flavor production backgrounds, as is used in other WH and $ZH \rightarrow llbb$ analyses. Cross section errors of 10% are given to top production and 11.5% for diboson.

- Due to measured differences between Monte Carlo and data, b-tagging efficiencies are known to be too high in simulated data. Studies documented in ref. [44] assign jets with Jet Probability $< 5\%$ a scale factor of 0.846±0.017(stat)±.066(syst) while tight b-tagged jets are assigned a scale factor of 0.95±0.01(stat)±.04(syst) [45].

- The lepton veto, is assigned an uncertainty of 2%. Since this is a small uncertainty, existing studies [46] are adequate to evaluate this systematic.

- Signal samples in which Initial State Radiation(ISR) and Final State Radiation(FSR) are independently increased and decreased for a Higgs mass of 120 GeV/c^2 were utilized to generate alternate Higgs signal models. The percent change in signal efficiency is displayed in table 10.1 for each sample. The average of the two double tagged categories is used as an uncertainty for each ISR/FSR systematic.

	ZH			WH		
	JP+Vtx Tag	2 Vtx Tag	Ave.	JP+Vtx Tag	2 Vtx Tag	Ave.
ISR Up	-2.0%	-1.4%	-1.7%	-2.3%	+3.0%	+0.4%
ISR Down	+5.7%	+4.2%	+5.0%	+5.9%	+3.9%	+4.9%
FSR Up	+4.2%	+4.0%	+4.1%	+0.7%	+4.2%	+2.5%
FSR Down	+1.5%	-0.8%	+0.4%	+1.1%	+9.2%	+5.2%

Table 10.1: *Change in signal efficiency for initial and final state radiation systematic samples.*

- For the mistagged background estimate uncertainty, alternate NN shapes are generated. Uncertainties to the mistag probability for each taggable jet in an event are considered. These errors add and subtract to the nominal mistag estimates, summing over all mistagged jets in all events in order to generate alternate NN output shapes.

- Shape systematics are applied to the data-based QCD model using the procedure outlined in sections 8.1.3 and 7.2.1.

- Uncertainties on the trigger efficiency vary as a function of $\not\!\!E_T$. The errors assigned to the trigger turn-on measured in ref. [30] are used to create up and down shape systematics for all Monte Carlo based signal and background.

CHAPTER 11

95% CONFIDENCE LEVEL LIMITS ON STANDARD MODEL HIGGS PRODUCTION

A fit of the data is performed independently in the two b-tagged signal samples in order to determine the QCD background contribution necessary for making comparisons in the signal region. The fitting procedure, allows each background to fluctuate by its uncertainties in order to fit the data. The fit returns the fluctuation on each background due to each systematic. Therefore, comparisons of input background expectations to the actual background contributions can be made. The initial estimate of the QCD background is given by subtracting all known background contributions from the data. This initial estimate is set to be unconstrained in the fit. Backgrounds are allows to fluctuate according to all uncertainties. Fitting with the null hypothesis or test hypothesis results in less than a 3% difference in the QCD fit value. In the actual expected and observed limit calculations, the signal is of course allowed to float. Table 11.1 shows expected background compared to fit backgrounds in the two signal regions.

To extract the 95% confidence level limit, the *mclimit*[47] progam is used. *Mclimit* uses the NN output as the figure of merit for fitting. The goal of this procedure is to evaluate the compatibility of the data of interest with the background model

	SecVtx + JP expected	observed	2 SecVtx expected	observed
$t\bar{t}$	8.1 ± 1.5	8.2	8.2 ± 1.3	8.1
single top	4.5 ± 0.8	4.6	4.7 ± 0.8	4.6
WZ/WW	1.4 ± 0.3	1.4	1.2 ± 0.2	1.2
ZZ	1.5 ± 0.4	1.5	1.7 ± 0.3	1.7
W+h.f.	8.8 ± 3.7	10.0	6.9 ± 2.9	6.5
Z+h.f.	8.8 ± 3.7	10.0	8.2 ± 3.4	7.8
Mistags	8.3 ± 2.4	8.3	1.5 ± 0.3	1.5
QCD fraction	20.7 ± 10.4	16.5	15.6 ± 8.6	16.3

Table 11.1: *Fit for QCD fraction. This shows the input backgrounds and uncertainties, and the fit values obtained from mclimit.*

prediction for that dataset. More specifically, this method is a reliable figure of merit for determining the expected sensitivity of an analysis to the signal given a background hypothesis. Once this expectation has been determined, the data is fit with the purpose of setting a 95% Confidence Level (CL) limit, or 2σ certainty that the signal is not present in the data sample above some cross-section or expected signal event yield. The procedure for determining the expected and observed sensitivity begins with the bin-by-bin expectations, or predictions of all backgrounds in the binned histogram chosen as the discriminant. In the case of this analysis, the neural network output described and illustrated in section 9.2 provides the binned shapes for the backgrounds, while the normalization priors and displayed in table [**?**]. All background predictions in each bin are considered by

$$b^b_{ij} = \sum_{k=1}^{n_i^{bsources}} F^b_{ik} B_{ijk} \tag{11.1}$$

with $n_i^{bsources}$ representing the number of individual background processes considered in channel i, F^b_{ik} representing the floating scale factor on background k in channel i

and B_{ijk} being the shape of background k, meaning the relative normalization in each bin j for channel i.

To compute the probability of observing a collected dataset d_{ij}, a fit is performed which maximizes the Poisson probability that it is observed given the background hypothesis. The function to be minimized for channel i is

$$\mathcal{L}_b = -ln\left[\prod_{j=1}^{n_i^{bins}} \frac{e^{-b_{ij}^b}(b_{ij}^b)^{d_{ij}}}{d_{ij}} \cdot \prod_{k=1}^{n_i^{bsources}} \frac{1}{\sqrt{2\pi\sigma_{ik}}} e^{\frac{-(F_{ik}^b-1)^2}{2\sigma_{ik}^{b\ 2}}}\right] \tag{11.2}$$

with σ_{ik}^b representing the systematic uncertainty on the normalization of of background k in channel. The minimization procedure is performed by the MINUIT [48] program.

An alternate hypothesis for the data can be built by considering both signal and background. The fitting function in this case will also include bin-by-bin contributions from a signal.

$$\mathcal{L}_{s+b} = -ln\left[\prod_{j=1}^{n_i^{bins}} \frac{e^{-(s_{ij}+b_{ij}^b}(s_{ij}+b_{ij}^s)^{d_{ij}}}{d_{ij}} \cdot \prod_{k=1}^{n_i^{bsources}} \frac{1}{\sqrt{2\pi\sigma_{ik}}} e^{\frac{-(F_{ik}^s-1)^2}{2\sigma_{ik}^{b\ 2}}}\right] \tag{11.3}$$

The background in terms of the floating parameters are given by

$$b_{ij}^s = \sum_{k=1}^{n_i^{bsources}} F_{ik}^s B_{ijk} \tag{11.4}$$

for the signal hypothesis. The signal rate may be allowed to float in fits of the signal+background hypothesis. A likelihood ratio can be constructed as a test statistic, such that

$$Q = \frac{P(data|H_{s+b})}{P(data|H_b)} \tag{11.5}$$

where H_b is the null hypothesis and H_{s+b} contains some new physics. The minimization of the χ^2 function

$$-2lnQ = \chi^2(data|H_{s+b}) - \chi^2(data|H_b) = \Delta\chi^2 \tag{11.6}$$

must be done separately for both hypotheses. The confidence level for excluding the signal+background hypothesis is then given by

$$CL_{H_1} = P_{H_1}(Q \leq Q_{obs}) \tag{11.7}$$

where $CL_{H_1} = 0.05$ would correspond to 95% confidence that a signal is not present in the given data sample above the predicted cross-section or expected rate.

The NN output for the tight SecVtx plus Jet Probability and the double tight SecVtx tagging categories are shown in Figures 11.1 and 11.2 respectively. The two tagging classes are treated as independent samples in *mclimit*, however, they have correlated systematic errors. The uncertainties for both normalization and shape systematics (see Section 10) are handled by *mclimit*. We run *mclimit* in the mass range from 110-150 GeV/c^2 . Table 11 shows the *a priori* 95% CL limits along with the $\pm 1\sigma$ and $\pm 2\sigma$ range of limits. These are presented as a ratio of the limit divided by the Standard Model cross section. The observed limit with the CDF data sample is shown in the final column of the table.

Tight SecVtx + Jet Probablility b-tagged						
Higgs Boson	*a priori* limits					
Mass (GeV/c^2)	-2σ	-1σ	median	$+1\sigma$	$+2\sigma$	Obs
110	6.6	9.0	12.8	18.6	26.2	20.9
115	7.4	10.0	14.3	21.0	30.3	18.8
120	8.7	11.8	16.7	24.5	35.2	21.8
130	13.2	18.0	25.6	37.5	53.7	23.9
140	23.3	31.0	44.2	64.8	90.1	38.9
150	58.4	77.4	109.2	157.4	222.1	79.6
Double Tight SecVtx b-tagged						
Higgs Boson	*a priori* limits					
Mass (GeV/c^2)	-2σ	-1σ	median	$+1\sigma$	$+2\sigma$	Obs
110	4.7	6.3	9.0	13.0	18.0	8.6
115	5.2	7.1	10.2	14.9	20.9	8.1
120	6.3	8.6	12.3	18.1	25.5	9.8
130	10.0	13.3	18.9	27.5	39.3	18.3
140	16.2	22.2	31.4	45.6	64.1	28.7
150	43.4	58.5	80.9	118.7	167.3	70.2
Combined Tagging Samples						
Higgs Boson	*a priori* limits					
Mass (GeV/c^2)	-2σ	-1σ	median	$+1\sigma$	$+2\sigma$	Obs
110	3.7	5.2	7.4	10.7	15.1	9.6
115	4.3	5.8	8.3	12.1	17.0	8.0
120	5.1	7.0	9.9	14.4	20.6	9.5
130	7.8	10.7	15.3	21.9	30.6	12.8
140	13.0	17.8	25.1	35.9	49.9	20.0
150	32.8	44.5	63.3	91.3	129.0	44.3

Table 11.2: The 95% CL limits as calculated by *mcLimit*. The numerical values give the ratio of the limit divided by the Standard Model prediction. Systematic errors are included in the calculation. The right-hand column gives the observed limit with CDF's 1.7 fb^{-1} data sample.

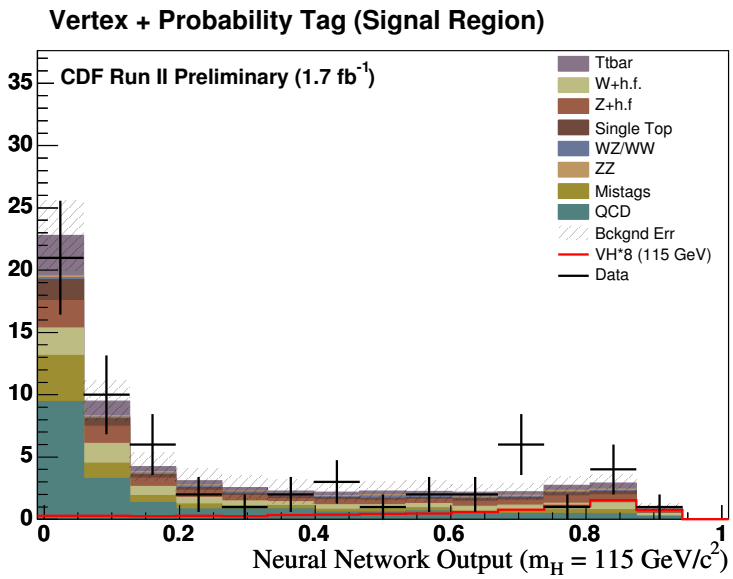

Figure 11.1: The N.N.D. output for Tight SecVtx plus Jet Probability tagged events.

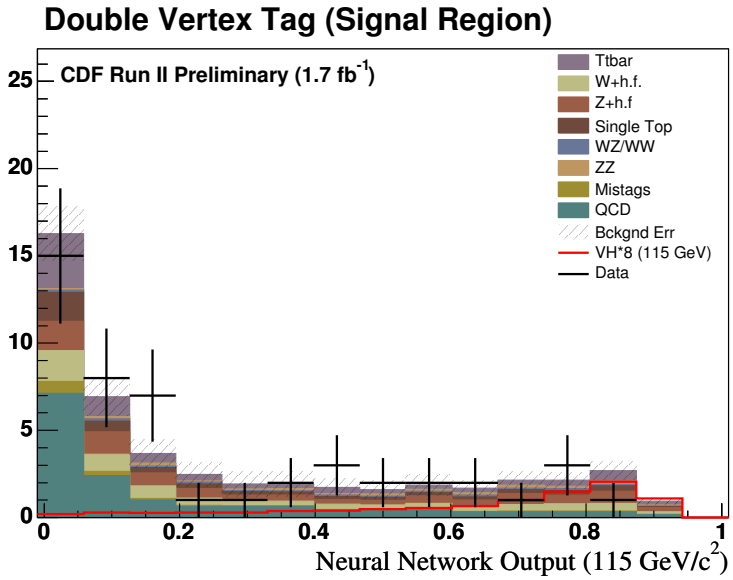

Figure 11.2: The N.N.D. output for double Tight SecVtx tagged events.

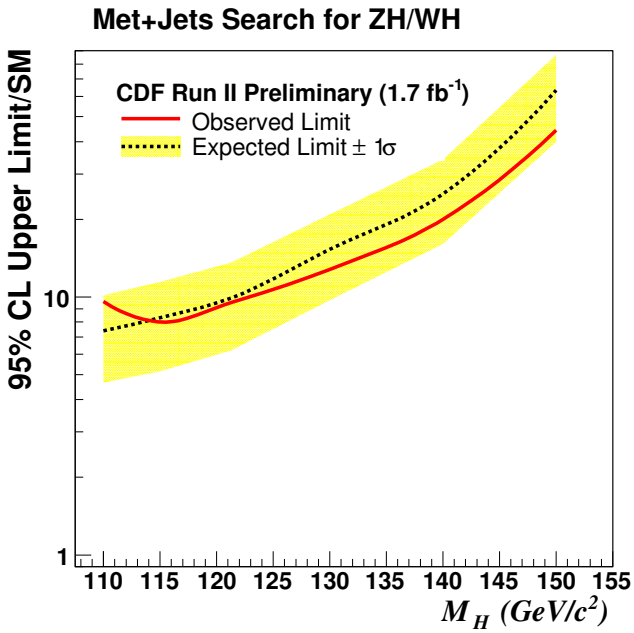

Figure 11.3: The expected and observed limits after combining the two double tag categories.

CHAPTER 12

CONCLUSION

The search for a Standard Model Higgs boson at the Tevatron has made immense progress since the first collisions of Run II took place. Large amounts of effort have been aimed at increasing the acceptance of Higgs signal events and developing innovative new techniques to reject background. This analysis has introduced a new track-based discriminant for rejecting the large multi-jet QCD background, which provides a means to loosen selection criteria and increase the expected Higgs yield without being overwhelmed by increased background rates. The development and implemtation of a neural network discriminant provides additional separation for not only the QCD background, but for top and electroweak processes as well. These elements are crucial in a search for the Higgs, as the signal rate is extremely small with large amounts of background. Additionally, techniques to derive multi-jet QCD models directly from CDF data have been developed to circumvent the immense difficulty of producing large QCD Monte Carlo datasets. The data-based approach provides an accurate desciption of heavy flavor QCD processes, and the statistical power of this technique only increases as more data is accumulated. Using these new analysis techniques have provided a significant boost in sensitivty, yielding the current CDF

limit on Higgs production in this channel as $8.0 \times SM$ with an expected value of $8.3 \times SM$ for a 115 GeV/c^2 Higgs boson.

While this channel alone has a large potential for the observation of an excess of events consistent with a Higgs signal once more data has been included, the true power of Higgs analysis at the Tevatron is only realized when the results of all analysis efforts are combined together. CDF and DØ have combined the results from the recent analyses, with data ranging from 1 to 2 fb^{-1} depending on on the channel and experiment. The results of this combination are displayed in Figure 12.1[49].

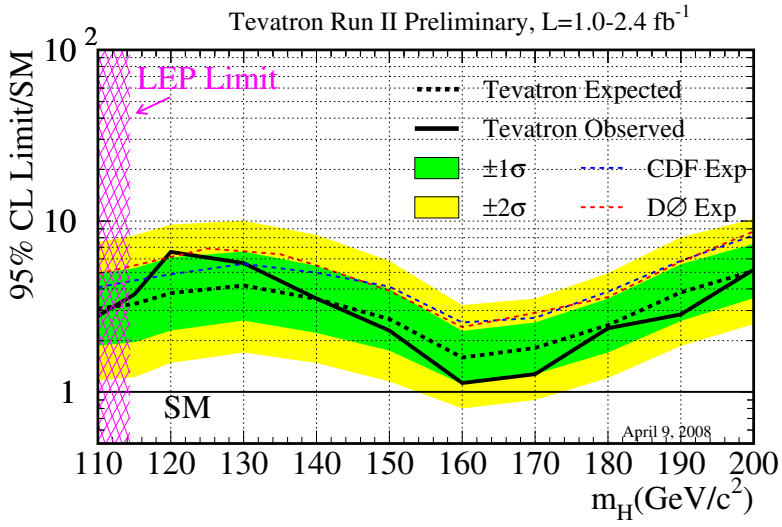

Figure 12.1: The combined sensitivity to a Standard Model Higgs for both the CDF and DØ collaborations. The sensivity is displayed as the expected and observed limits over the Standard Model expectation as a function of Higgs mass.

Results from the Tevatron are inching very close to excluding a Higgs boson in the mass region of 160 GeV/c^2 at the 95% confidence level. Improvements to the $H \rightarrow WW$ analysis and the addition of new data should make this possible within a year from now (June 2008). Many improvements to the lower mass Higgs analyses are underway as well, which promise to push the current expected limit of $3.3 \times SM$ for a Higgs mass of 115 GeV/c^2 even closer to the Standard Model expectation. Improvements to secondary vertex tagging, increased signal acceptance and more advanced mutlivariate discriminants are in the works, making the observation of the Higgs boson at the Tevatron a real possibility.

APPENDIX A

ADDITIONAL DISTRIBUTIONS

In addition to checks of input variables to the neural network (shown in the previous sections), we have also studied a variety of other kinematic and topological distributions. These are shown for both control regions, and the three tagging categories of the signal region.

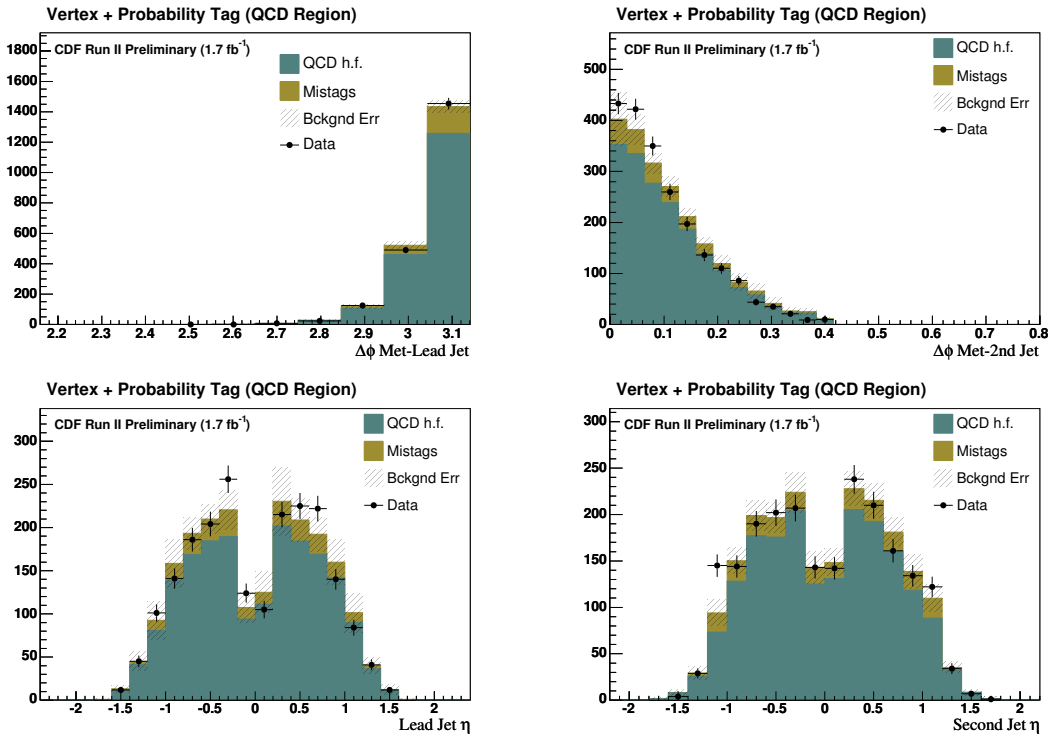

Figure A.1: Figures for 1 tight SECVTX + JP tags in region where Missing E_T is aligned with second jet. Upper left: $\Delta\phi LeadJet{-}MET$; upper right: $\Delta\phi SecondJet{-}MET$; lower left: Lead Jet η; lower right: Second Jet η.

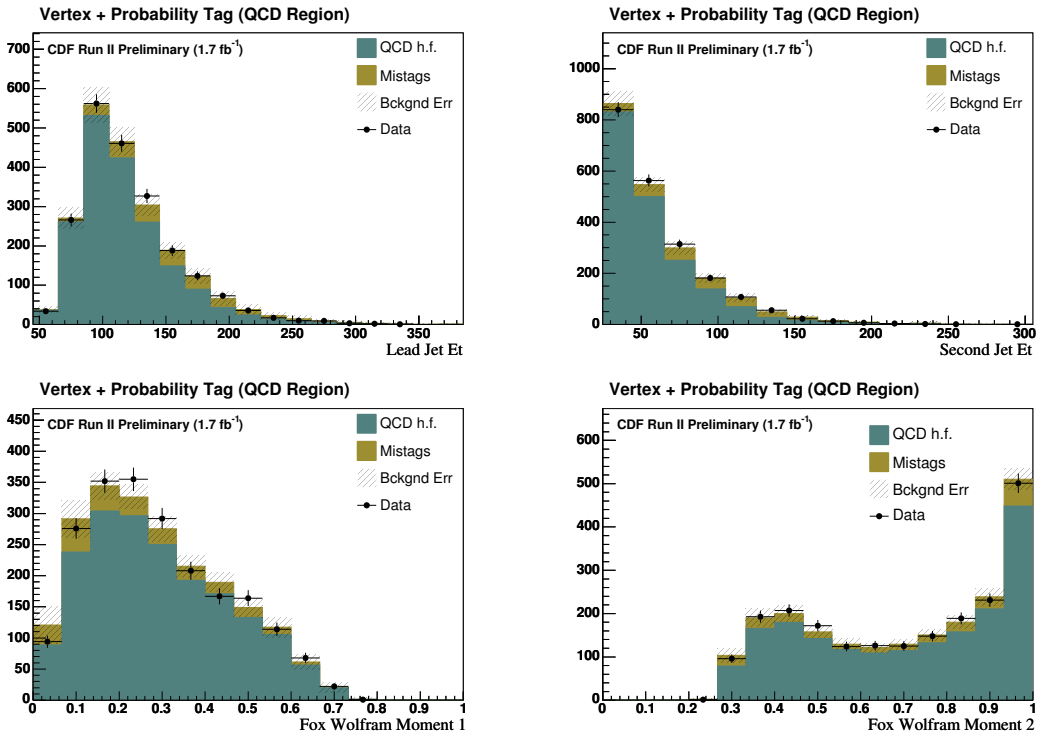

Figure A.2: Figures for tight + JP tags in region where Missing E_T is aligned with second jet. Upper left: Lead Jet E_t; upper right: Second Jet E_t; lower left: Fox Wolfram Moment 1; lower right: Fox Wolfram Moment 2.

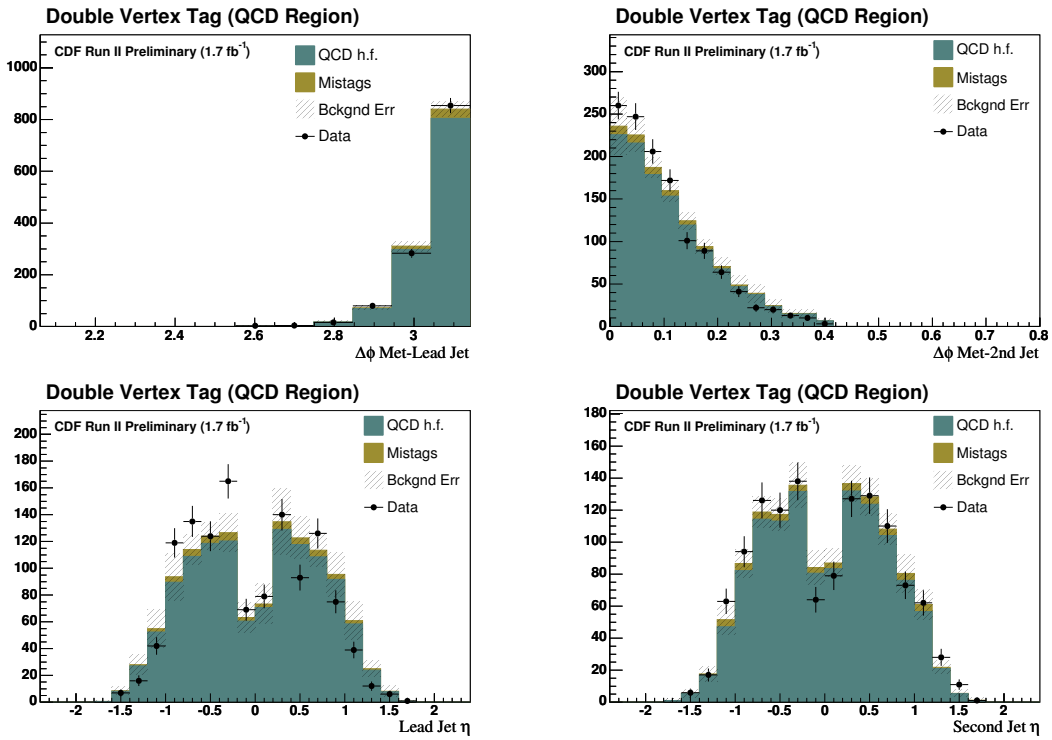

Figure A.3: Figures for 2 tight SECVTX tags in region where Missing E_T is aligned with second jet. Upper left: $\Delta\phi LeadJet - MET$; upper right: $\Delta\phi SecondJet - MET$; lower left: Lead Jet η; lower right: Second Jet η.

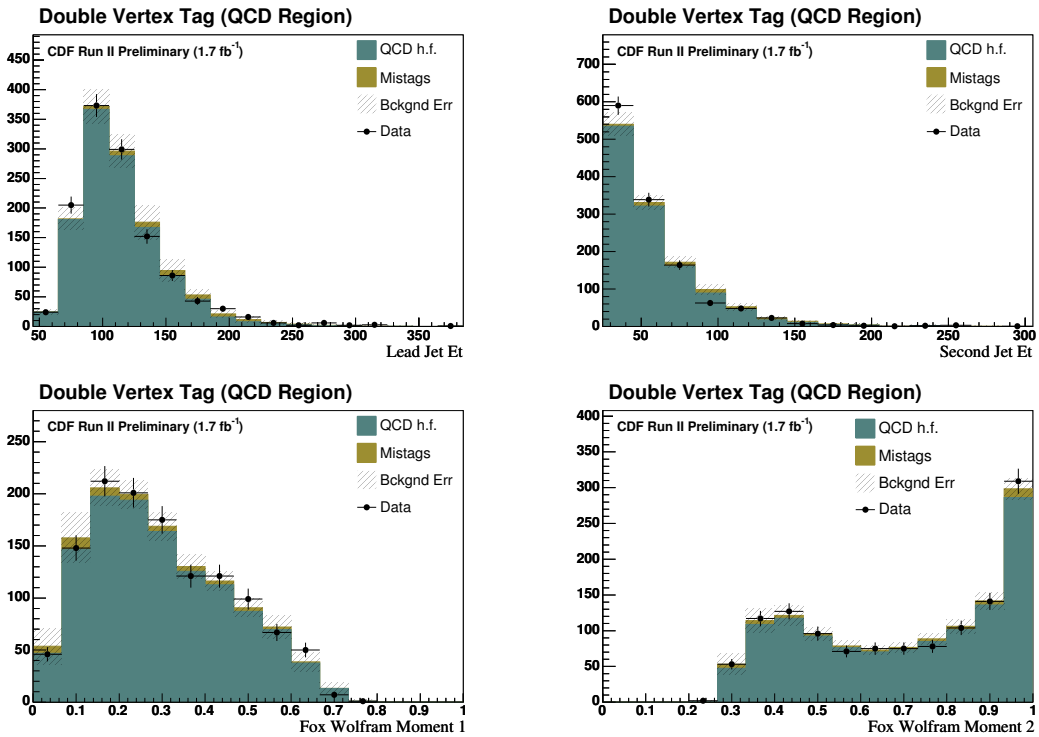

Figure A.4: Figures for 2 tight SECVTX tags in region where Missing E_T is aligned with second jet. Upper left: Lead Jet E_t; upper right: Second Jet E_t.; lower left: Fox Wolfram Moment 1; lower right: Fox Wolfram Moment 2.

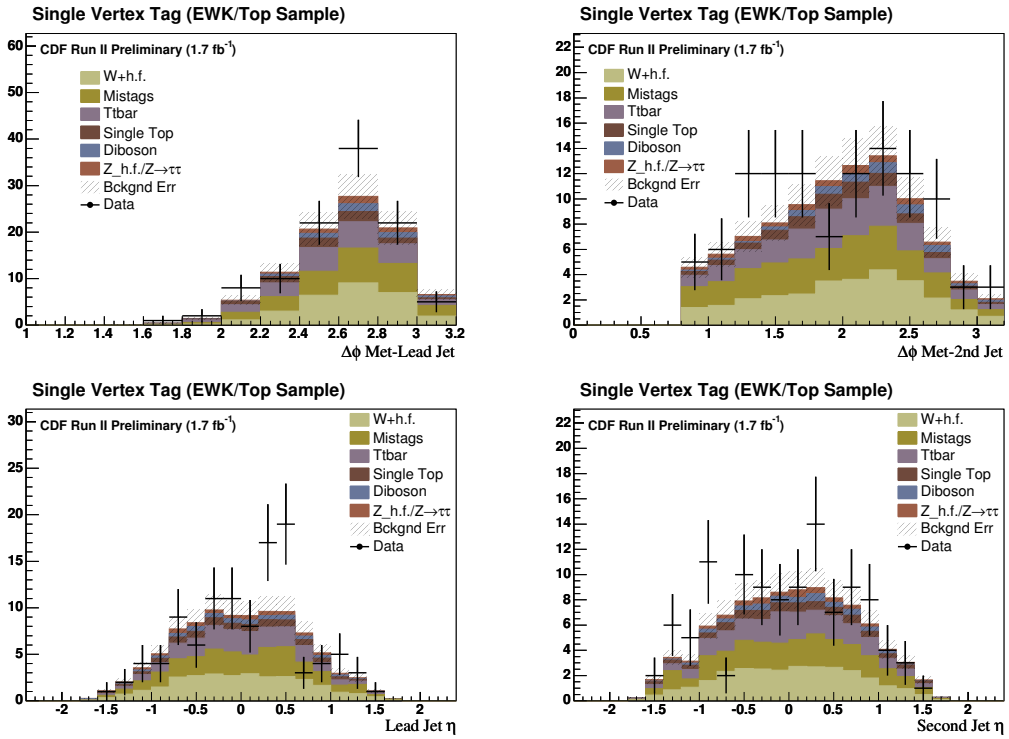

Figure A.5: Figures for single tag muon data. Upper left: $\Delta\phi(MET, jet1)$; upper right: $\Delta\phi(MET, jet2)$; lower left: Lead Jet *eta*; lower right: Second Jet *eta*.

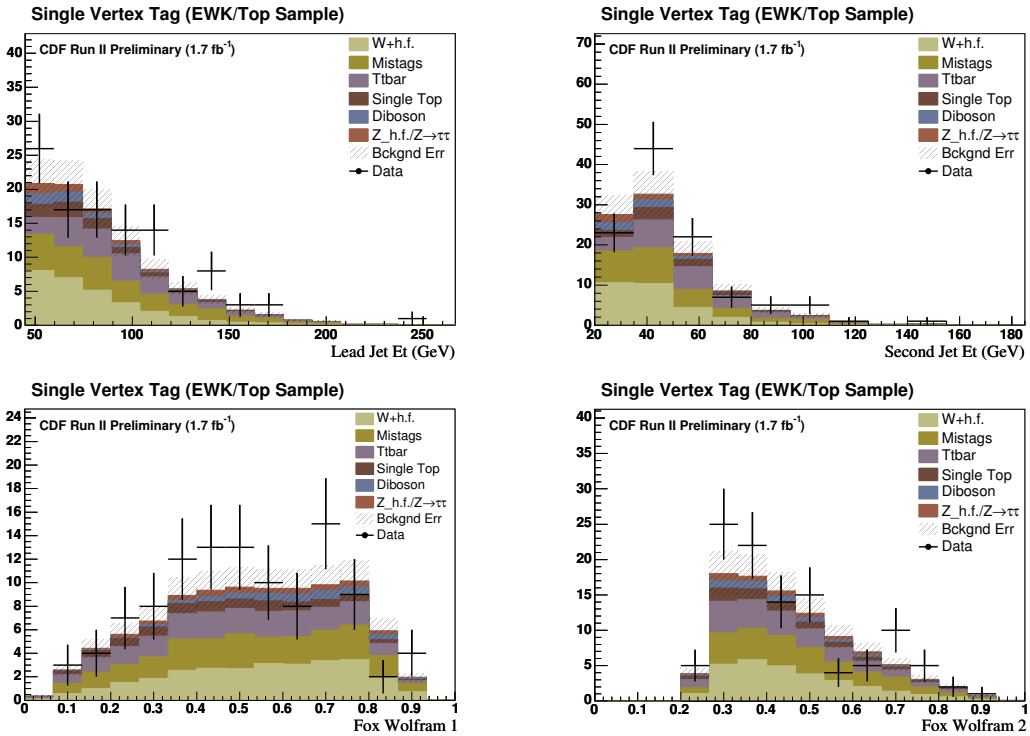

Figure A.6: Figures for single tag muon data. Upper left: Lead Jet E_t; upper right: Second Jet E_t; lower left: Fox Wolfram Moment 1; lower right: Fox Wolfram Moment 2;

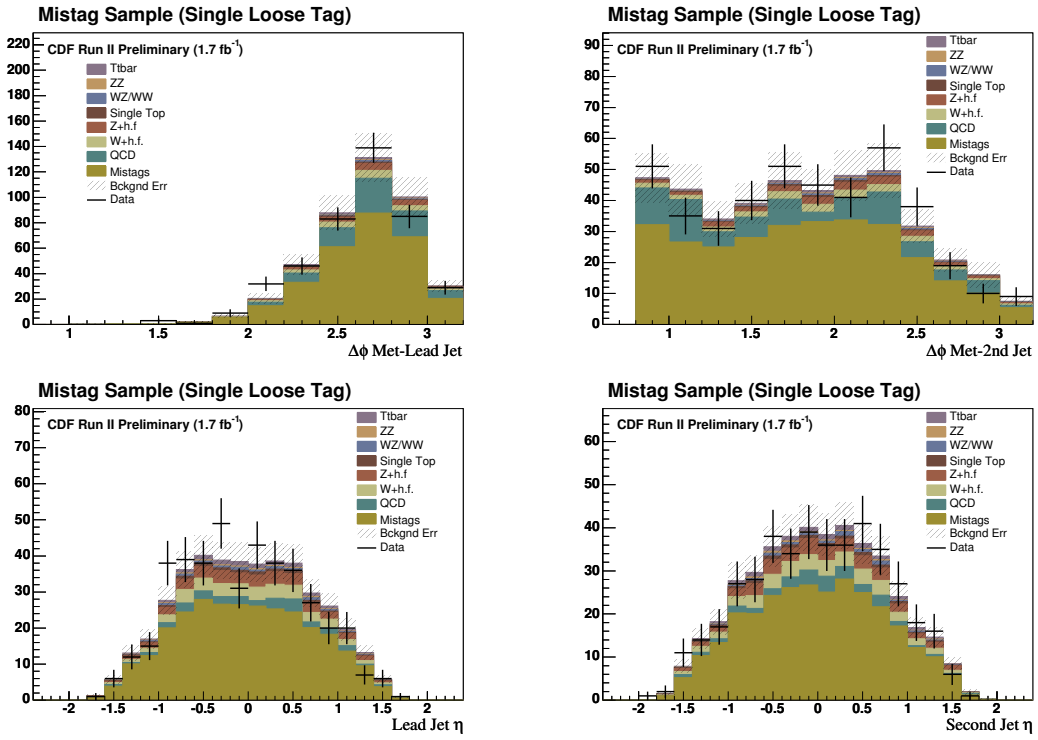

Figure A.7: Figures for 1 loose tag in signal region. Upper left: $\Delta\phi LeadJet - MET$; upper right: $\Delta\phi SecondJet - MET$; lower left: Lead Jet η; lower right: Second Jet η.

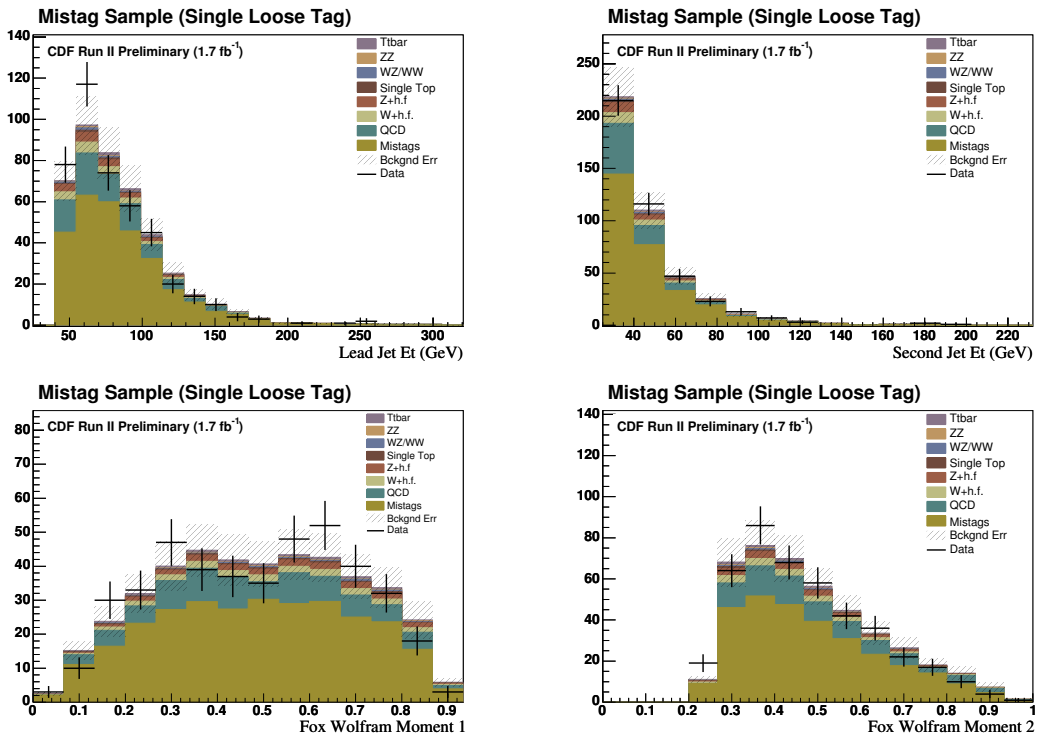

Figure A.8: Figures for 1 loose tag in signal region. Upper left: Lead Jet E_t; upper right: Second Jet E_t; lower left: Fox Wolfram Moment 1; lower right: Fox Wolfram Moment 2;

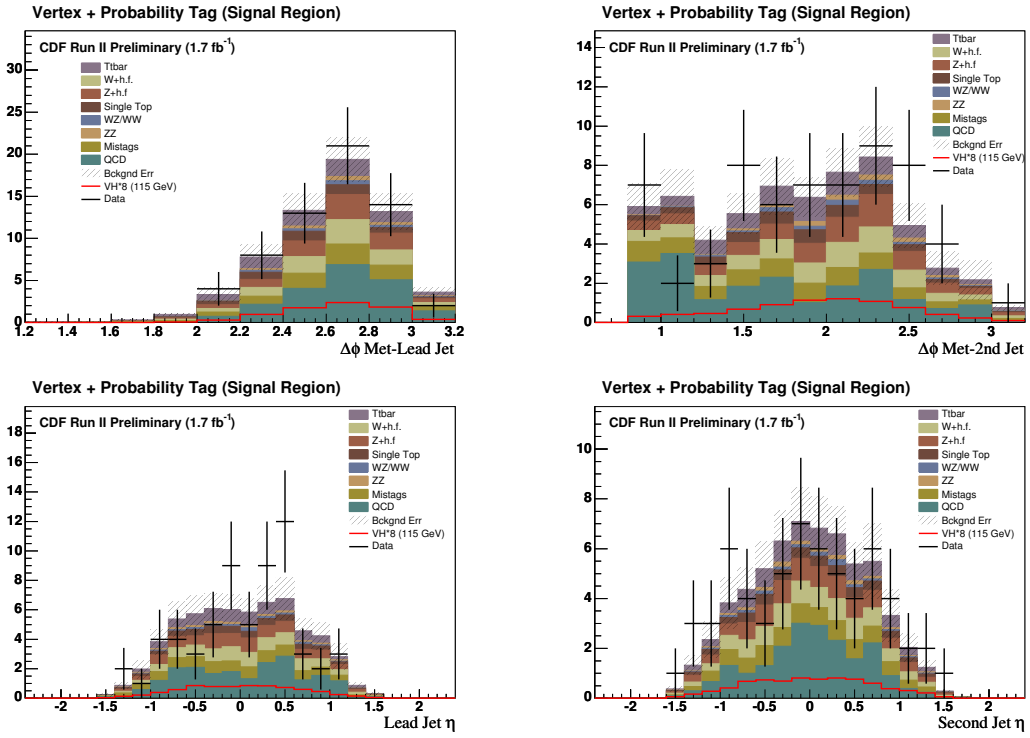

Figure A.9: Figures for 1 tight SECVTX plus Jet Probability tag in signal region. Upper left: $\Delta\phi LeadJet - MET$; upper right: $\Delta\phi SecondJet - MET$; lower left: Lead Jet η; lower right: Second Jet η.

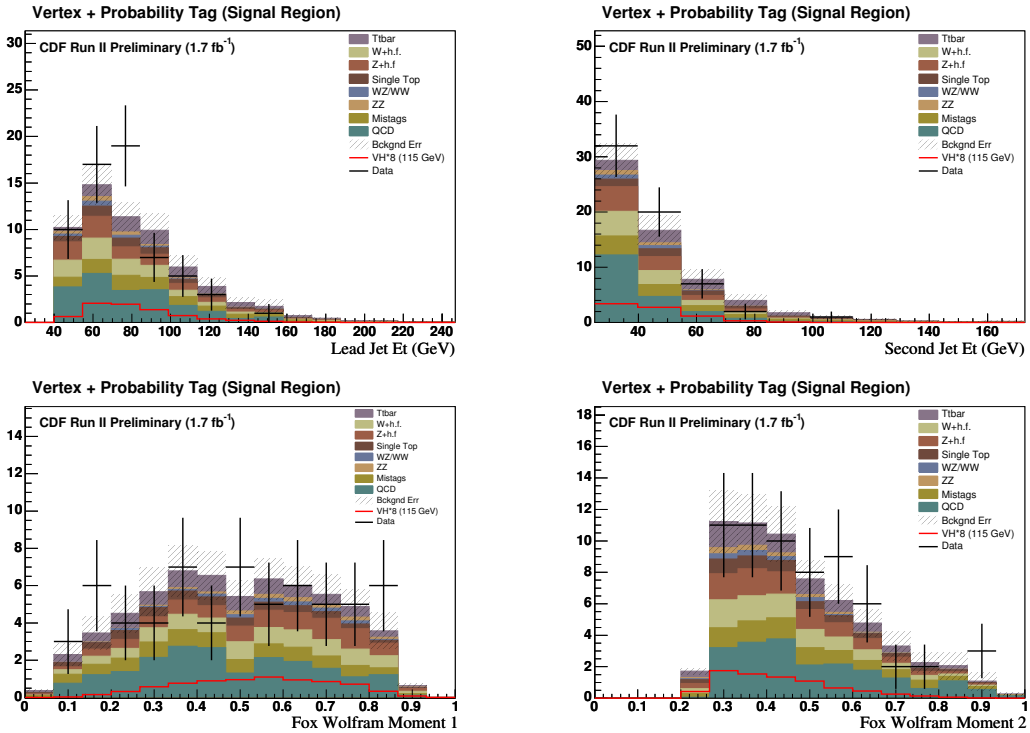

Figure A.10: Figures for 1 tight SECVTX tag + Jet Probability tag in signal region. Upper left: Lead Jet E_t; upper right: Second Jet E_t; lower left: Fox Wolfram Moment 1; lower right: Fox Wolfram Moment 2;

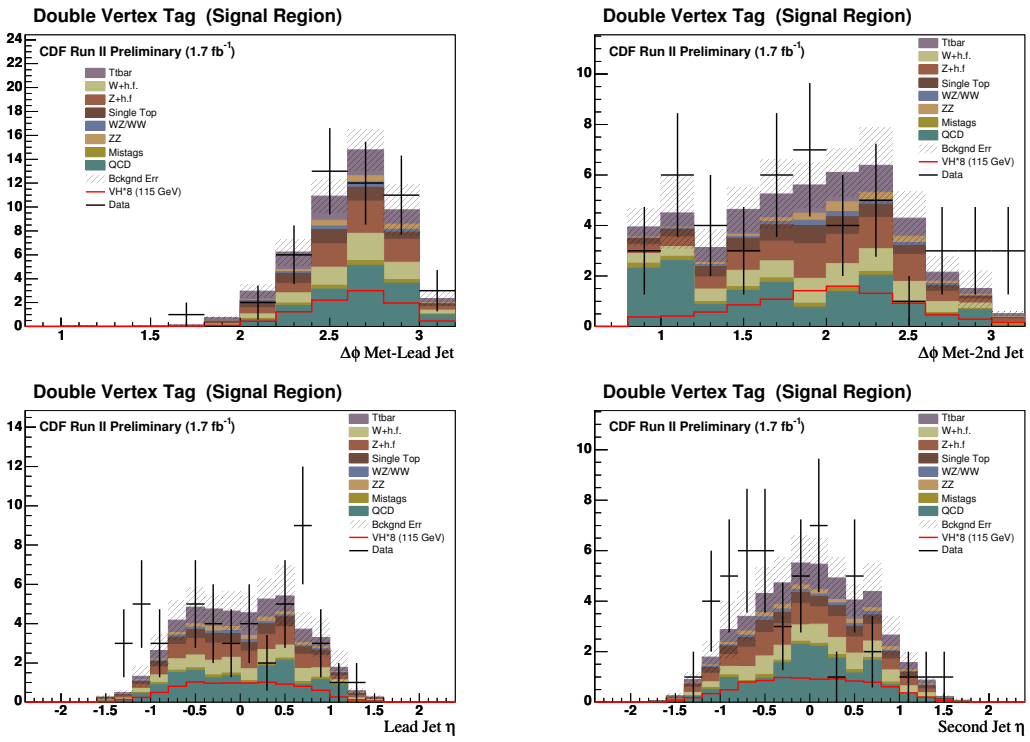

Figure A.11: Figures for 2 tight SECVTX in signal region. Upper left: $\Delta\phi LeadJet - MET$; upper right: $\Delta\phi SecondJet - MET$; lower left: Lead Jet η; lower right: Second Jet η.

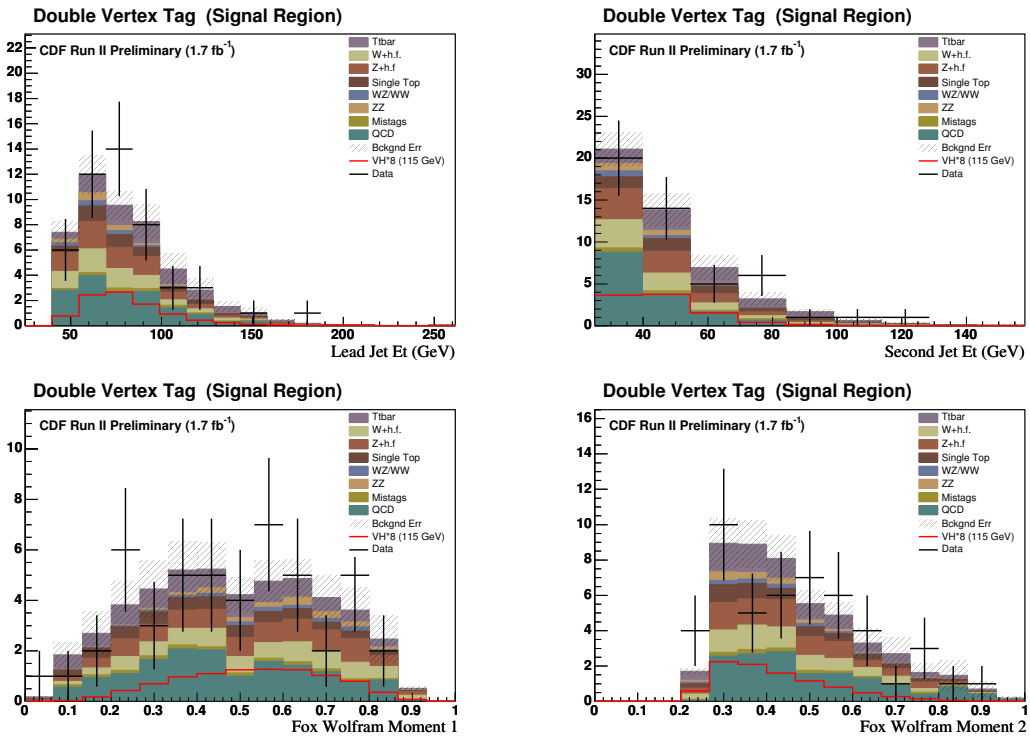

Figure A.12: Figures for 2 tight SECVTX tags in signal region. Upper left: Lead Jet E_t; upper right: Second Jet E_t; lower left: Fox Wolfram Moment 1; lower right: Fox Wolfram Moment 2.

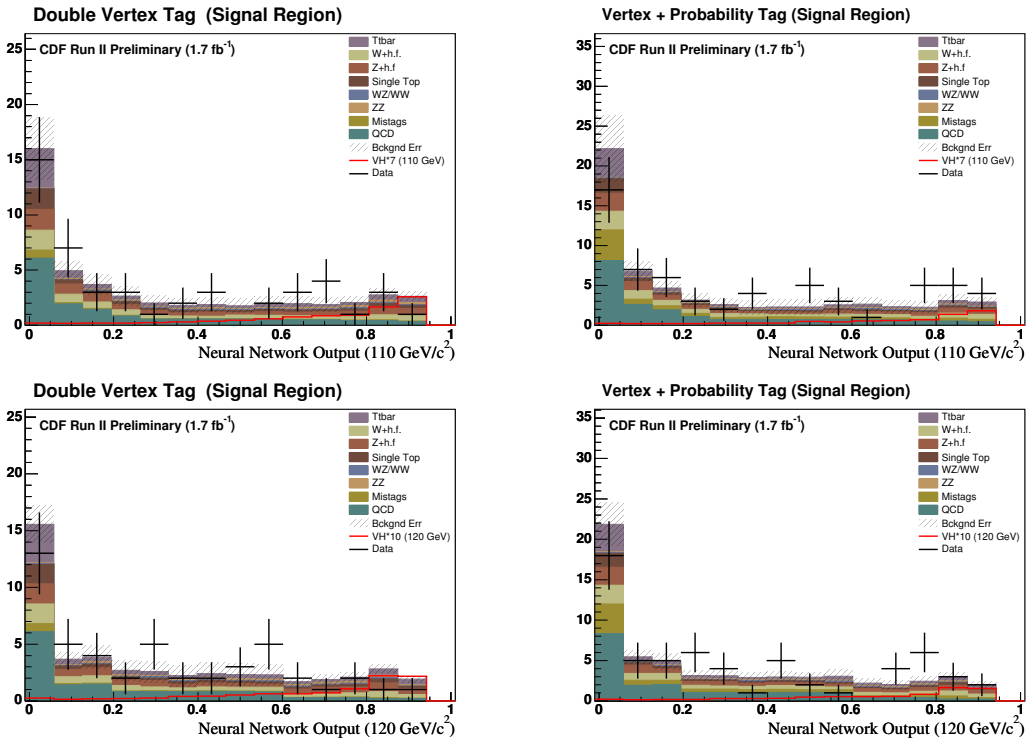

Figure A.13: Additional Neural Network Discriminants. Upper left: 110 GeV/c^2 2 tight SECVTX tags; upper right: 110 GeV/c^2 Tight SECVTX + Jet Probability tag; lower left: 120 GeV/c^2 2 tight SECVTX tags; lower right: 120 GeV/c^2 Tight SECVTX + Jet Probability tag.

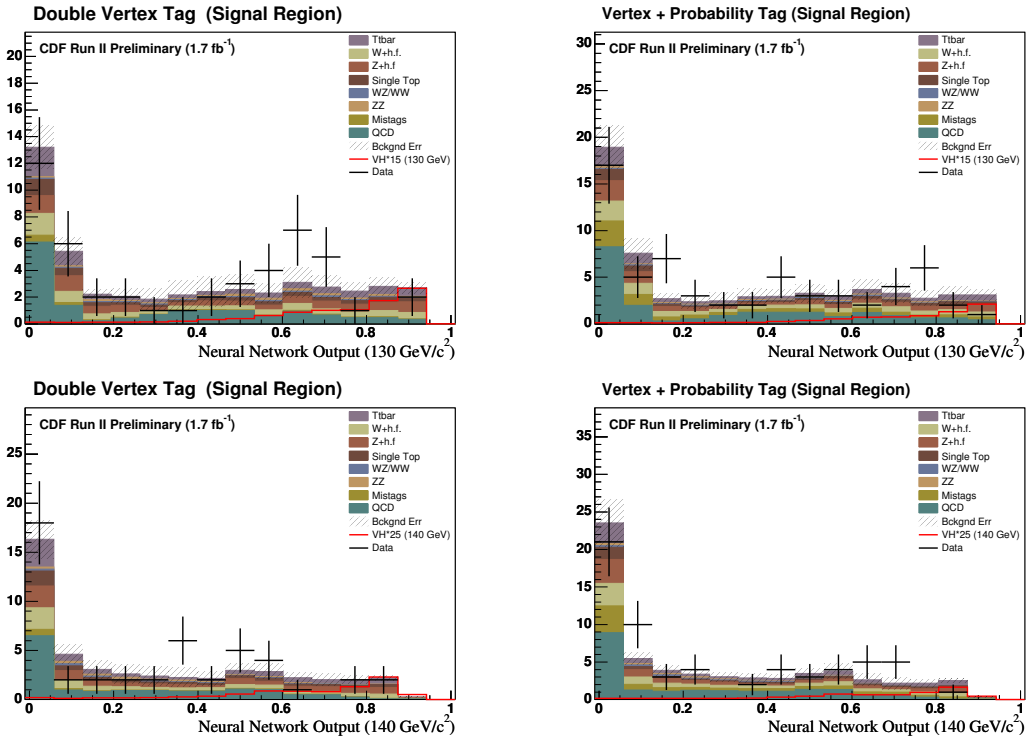

Figure A.14: Additional Neural Network Discriminants. Upper left: 130 GeV/c^2 2 tight SECVTX tags; upper right: 130 GeV/c^2 Tight SECVTX + Jet Probability tag; lower left: 140 GeV/c^2 2 tight SECVTX tags; lower right: 140 GeV/c^2 Tight SECVTX + Jet Probability tag.

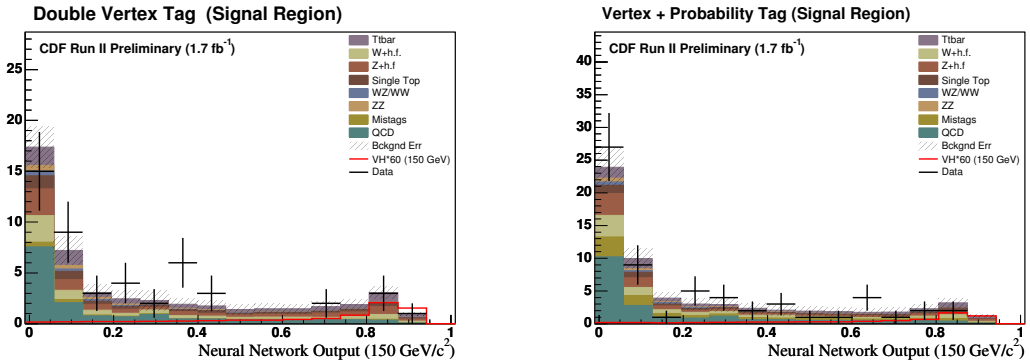

Figure A.15: Additional Neural Network Discriminants. Left: 150 GeV/c^2 2 tight SECVTX tags; Right: 150 GeV/c^2 Tight SECVTX + Jet Probability tag.

APPENDIX B

MOST SIGNAL-LIKE HIGGS EVENTS

A list of the most signal-like NN events are displayed in Table B.1. The most signal-like event has a NN output value of 0.886698. The breakdown of events in this bin are shown in Tables B.2 and B.3. Our most signal-like tight secvtx + jetprob event has a NN output of 0.887 and its bin (14) has a S:B of 1:9. The most signal-like tight secvtx + tight sectvx event has a NN output of 0.867 and its bin (13) has a S:B of 1:10. Various event displays of the most signal-like Higgs event are shown in figures B.1-B.5.

(Run, Event)	Type	NN Out	Mjj (GeV)	Met (GeV)	TrackMet NNOut
(184957, 962706)	T+T	0.8004	83.517	144.62	1.01028
(177624, 409702)	T+JP	0.8363	90.134	75.466	1.06492
(191727, 6339054)	T+JP	0.8192	92.815	105.82	1.05492
(200536, 4538872)	T+JP	0.8866	103.25	87.932	1.14904
(202399, 1194677)	T+T	0.7726	95.182	55.936	1.02202
(222250, 2474844)	T+T	0.8672	100.57	85.535	1.04985
(230782, 2230670)	T+JP	0.8099	102.17	54.719	1.0321
(236255, 25082019)	T+JP	0.8714	99.425	127.92	1.04084

Table B.1: *Most signal-like events with NN output > 0.75.*

Background	Expected events	Percentage
Z+h.f	0.214	25.8
TTBAR	0.186	22.5
W+h.f	0.181	21.8
single-top	0.064	7.7
WZ/WW	0.027	3.2
ZZ	0.054	6.5
Mistags	0.052	6.3
QCD	0.051	6.1
Total	0.829	100
ZH	0.070	74.8
WH	0.024	25.2
total VH	0.094	100

Table B.2: *Background composition of bin (bin 14) where we have our most signal-like event in tight+jet prob sample in data (run=200536, event=4538872).*

Background	Expected events	Percentage
Z+h.f	0.704	27.0
TTBAR	0.602	23.1
W+h.f	0.428	16.4
single-top	0.288	11.0
ZZ	0.262	10.0
QCD	0.182	6.97
WZ/WW	0.089	3.41
Mistags	0.053	2.04
Total	2.61	100
ZH	0.171	66.8
WH	0.085	33.2
total VH	0.256	100

Table B.3: *Background composition of bin containing most signal-like event in Vtx+Vtx output distribution (bin 13).*

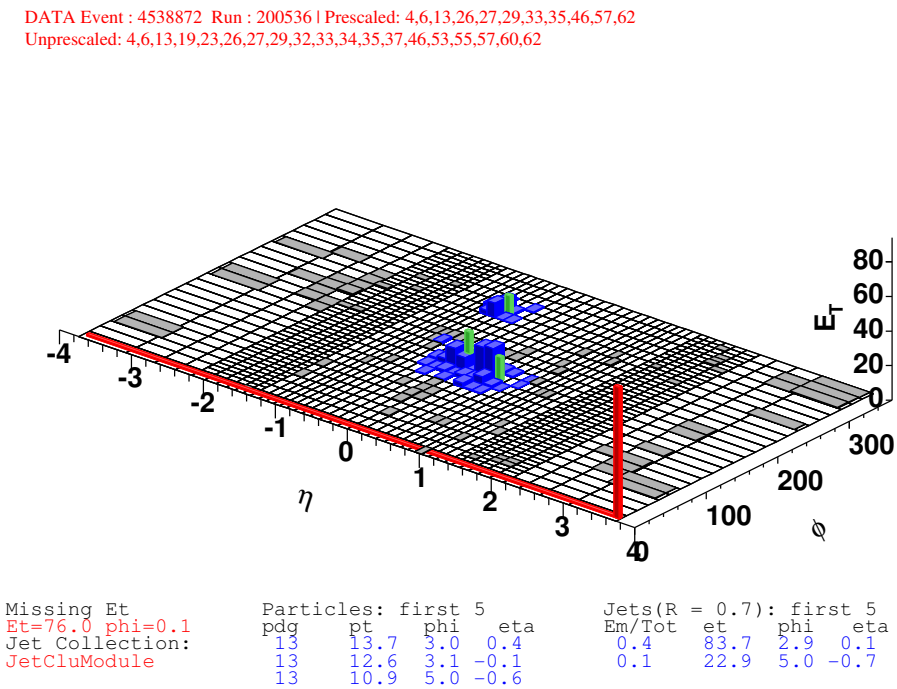

Figure B.1: Lego display of most signal-like event.

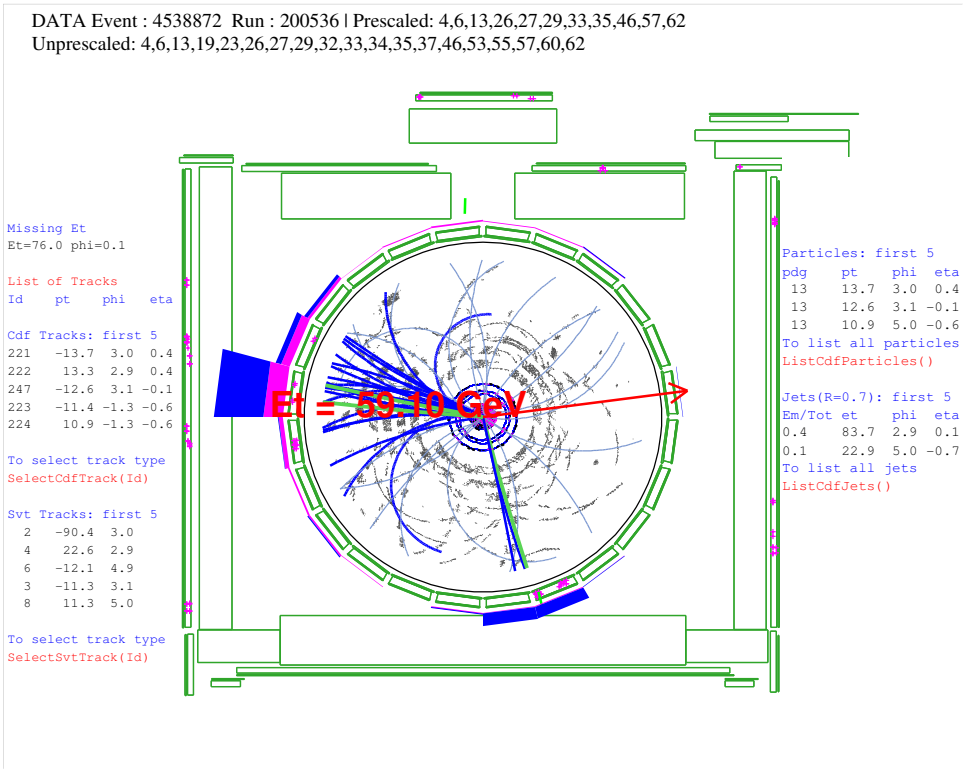

Figure B.2: COT display of most signal-like event.

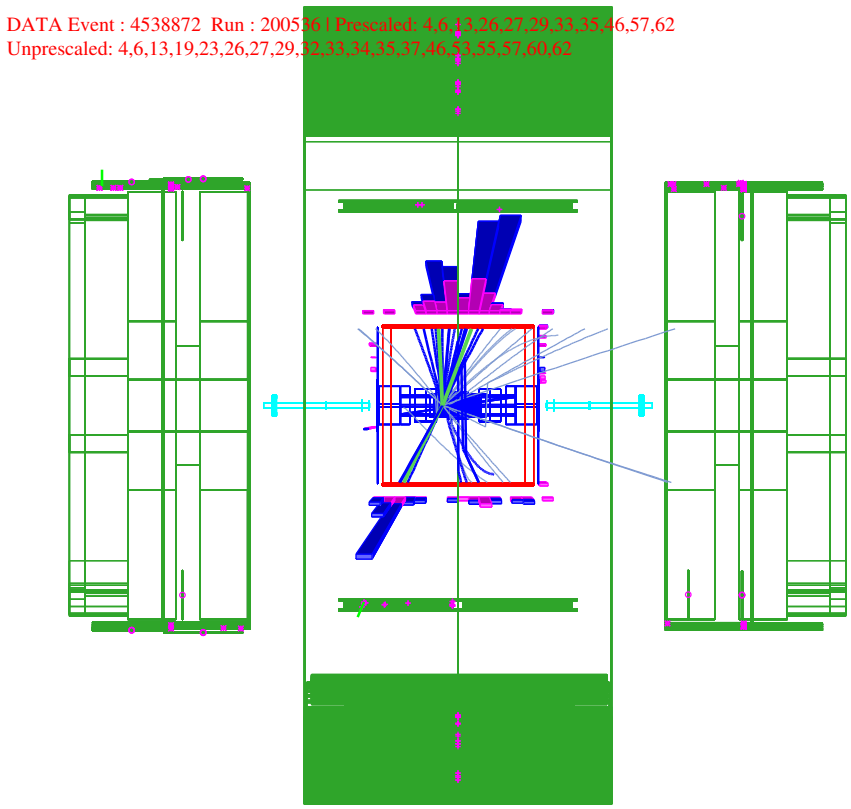

Figure B.3: RZ display of most signal-like event.

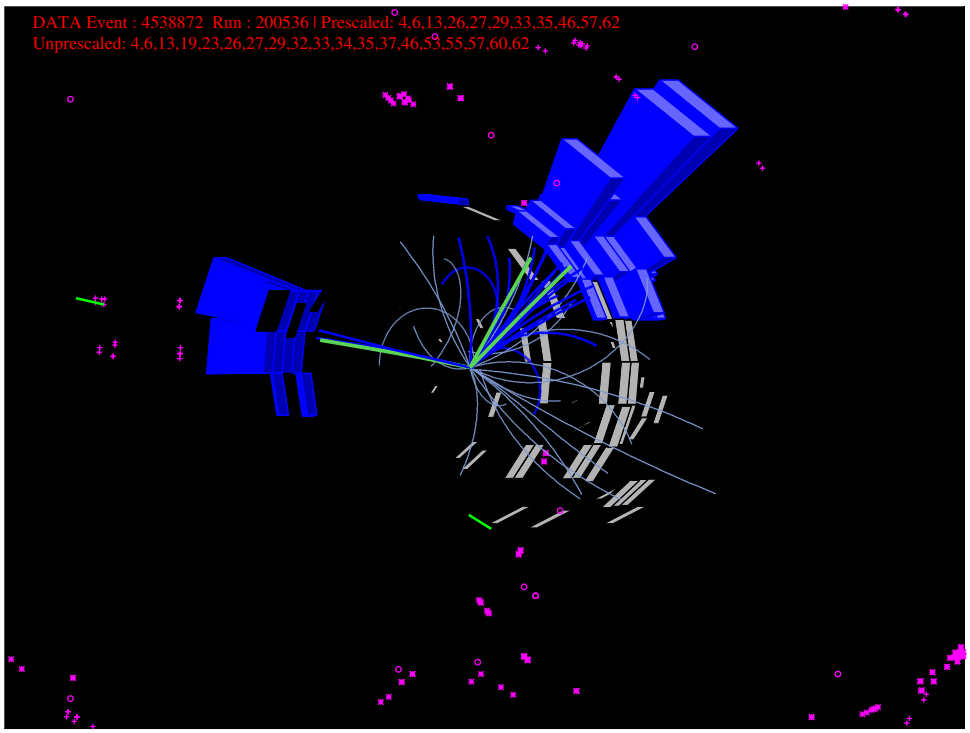

Figure B.4: Calorimeter display of most signal-like event.

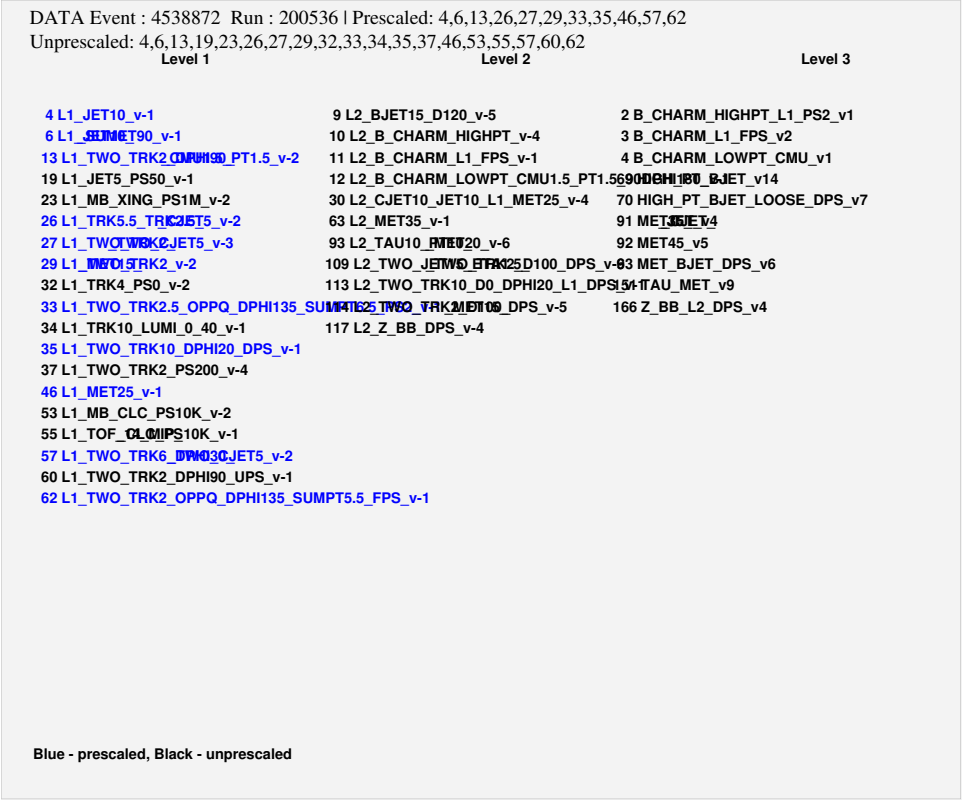

Figure B.5: Trigger display of most signal-like event.

BIBLIOGRAPHY

[1] S. L. Glashow, *Partial Symmetries of Weak Interactions*, *Nucl. Phys.* **22** (1961) 579–588.

[2] S. Weinberg, *A Model of Leptons*, *Phys. Rev. Lett.* **19** (1967) 1264–1266.

[3] F. Halzen and A. D. Martin, *QUARKS AND LEPTONS: AN INTRODUCTORY COURSE IN MODERN PARTICLE PHYSICS*, . New York, Usa: Wiley (1984) 396p.

[4] A. Salam, *Weak and Electromagnetic Interactions*, . Originally printed in *Svartholm: Elementary Particle Theory, Proceedings Of The Nobel Symposium Held 1968 At Lerum, Sweden*, Stockholm 1968, 367-377.

[5] H. E. Haber, *Introductory low-energy supersymmetry*, `hep-ph/9306207`.

[6] J. F. Gunion, H. E. Haber, G. L. Kane and S. Dawson, *THE HIGGS HUNTER'S GUIDE*, . SCIPP-89/13.

[7] **LEP** Collaboration, *The LEP collider*, 1990.

[8] **Fermilab Beams Division** Collaboration, *Tevatron Run 2 handbook*, 1998.

[9] **ALEPH** Collaboration, *Precision electroweak measurements on the Z resonance*, *Phys. Rept.* **427** (2006) 257 [`hep-ex/0509008`].

[10] F. Abe, H. Akimoto, A. Akopian, M. G. Albrow, S. R. Amendolia, D. Amidei, J. Antos, C. Anway-Wiese, S. Aota, G. Apollinari, T. Asakawa, W. Ashmanskas, M. Atac, P. Auchincloss, F. Azfar, P. Azzi-Bacchetta, N. Bacchetta, W. Badgett, S. Bagdasarov, M. W. Bailey, J. Bao, P. de Barbaro, A. Barbaro-Galtieri, V. E. Barnes, B. A. Barnett, P. Bartalini and G. Bauer, *Observation of top quark production in $p\overline{p}$ collisions with the collider detector at fermilab*, *Phys. Rev. Lett.* **74** (Apr, 1995) 2626–2631.

[11] S. Abachi, B. Abbott, M. Abolins, B. S. Acharya, I. Adam, D. L. Adams, M. Adams, S. Ahn, H. Aihara, J. Alitti, G. Álvarez, G. A. Alves, E. Amidi, N. Amos, E. W. Anderson, S. H. Aronson, R. Astur, R. E. Avery, A. Baden, V. Balamurali, J. Balderston, B. Baldin, J. Bantly, J. F. Bartlett, K. Bazizi, J. Bendich and S. B. Beri, *Observation of the top quark*, *Phys. Rev. Lett.* **74** (Apr, 1995) 2632–2637.

[12] **L3** Collaboration, M. Acciarri *et. al.*, *Search for the standard model Higgs boson in e^+e^- collisions at $\sqrt{s}$ up to 202-GeV*, *Phys. Lett.* **B508** (2001) 225–236 [hep-ex/0012019].

[13] **LEP** Collaboration, T. LEP Higgs Working Group, *Standard Model Higgs Boson at LEP: Results with the 2000 Data, Request for Running in 2001*, 2000.

[14] **LEP Working Group for Higgs boson searches** Collaboration, R. Barate *et. al.*, *Search for the standard model Higgs boson at LEP*, *Phys. Lett.* **B565** (2003) 61–75 [hep-ex/0306033].

[15] **CDF** Collaboration, F. Abe *et. al.*, *The CDF detector: an overview*, *Nucl. Instr. Meth.* **A271** (1988) 387–403.

[16] **CDF** Collaboration, A. Sill, *CDF run II silicon tracking projects*, *Nucl. Instrum. Meth.* **A447** (2000) 1–8.

[17] **CDF** Collaboration, A. A. Affolder *et. al.*, *Intermediate silicon layers detector for the CDF experiment*, *Nucl. Instrum. Meth.* **A453** (2000) 84–88.

[18] **CDF** Collaboration, K. T. Pitts, *The CDF central outer tracker*, *Nucl. Phys. Proc. Suppl.* **61B** (1998) 230–235.

[19] **CDF** Collaboration, A. A. Affolder *et. al.*, *CDF central outer tracker*, *Nucl. Instrum. Meth.* **A526** (2004) 249–299.

[20] **CDF** Collaboration, L. Balka *et. al.*, *The CDF central electromagnetic calorimeter*, *Nucl. Instrum. Meth.* **A267** (1988) 272.

[21] **CDF** Collaboration, S. Bertolucci *et. al.*, *The CDF central and endwall hadron calorimeter*, *Nucl. Instrum. Meth.* **A267** (1988) 301.

[22] **CDF** Collaboration, M. G. Albrow *et. al.*, *The CDF plug upgrade electromagnetic calorimeter: Test beam results*, *Nucl. Instrum. Meth.* **A480** (2002) 524–546.

[23] G. Ascoli *et. al.*, *CDF central muon detector*, *Nucl. Instrum. Meth.* **A268** (1988) 33.

[24] D. Acosta *et. al.*, *The performance of the CDF luminosity monitor*, *Nucl. Instrum. Meth.* **A494** (2002) 57–62.

[25] F. Abe, D. Amidei, G. Apollinari, M. Atac, P. Auchincloss, A. R. Baden, N. Bacchetta, M. W. Bailey, A. Bamberger, P. de Barbaro, B. A. Barnett, A. Barbaro-Galtieri, V. E. Barnes, T. Baumann, F. Bedeschi, S. Behrends, S. Belforte, G. Bellettini, J. Bellinger, D. Benjamin, J. Bensinger, A. Beretvas, J. P. Berge, S. Bertolucci, S. Bhadra, M. Binkley and R. Blair, *Topology of three-jet events in $p\overline{p}$ collisions at $s = 1.8$ tev*, *Phys. Rev. D* **45** (Mar, 1992) 1448–1458.

[26] A. Bhatti *et. al.*, *Determination of the jet energy scale at the Collider Detector at Fermilab*, *Nucl. Instrum. Meth.* **A566** (2006) 375–412 [hep-ex/0510047].

[27] **CDF-II** Collaboration, D. E. Acosta *et. al.*, *Measurement of the $t\bar{t}$ production cross section in $p\bar{p}$ collisions at $\sqrt{s} = 1.96$ TeV using kinematic fitting of $b-$tagged lepton + jet events*, *Phys. Rev.* **D71** (2005) 072005 [hep-ex/0409029].

[28] **ALEPH** Collaboration, D. Buskulic *et. al.*, *A Precise measurement of Gamma ($Z \to b$ anti-b) / Gamma ($Z \to$ hadrons)*, *Phys. Lett.* **B313** (1993) 535–548.

[29] D. Acosta *et. al.*, *Clean up of the missing transverse energy datasets*, *CDF Note 7410* (2004).

[30] V. Veszpremi, *Ph. D. thesis*, 2007.

[31] T. Han and S. Willenbrock, *QCD correction to the $p\ p \to W\ H$ and $Z\ H$ total cross- sections*, *Phys. Lett.* **B273** (1991) 167–172.

[32] A. Djouadi, J. Kalinowski and M. Spira, *HDECAY: A program for Higgs boson decays in the standard model and its supersymmetric extension*, *Comput. Phys. Commun.* **108** (1998) 56–74 [hep-ph/9704448].

[33] T. Sjostrand *et. al.*, *High-energy-physics event generation with PYTHIA 6.1*, *Comput. Phys. Commun.* **135** (2001) 238–259 [hep-ph/0010017].

[34] F. Maltoni and T. Stelzer, *MadEvent: Automatic event generation with MadGraph*, *JHEP* **02** (2003) 027 [hep-ph/0208156].

[35] M. L. Mangano, M. Moretti, F. Piccinini, R. Pittau and A. D. Polosa, *ALPGEN, a generator for hard multiparton processes in hadronic collisions*, *JHEP* **07** (2003) 001 [hep-ph/0206293].

[36] **CDF** Collaboration, F. Abe *et. al.*, *Evidence for top quark production in $\bar{p}p$ collisions at $\sqrt{s} = 1.8$ TeV*, *Phys. Rev.* **D50** (1994) 2966–3026.

[37] S. Grinstein and D. Sherman, *Jet Probability Tag Rate Matrix for Gen6 Data, CDF Note 8899*, 2004.

[38] B. Alavaraz *et. al.*, *Jet Probability Tag Rate Matrix for Gen6 Data, CDF Note 8899*, 2004.

[39] J. Efron, *Search for the Higgs Boson in the $ZH \to l^+l^-b\bar{b}$ Channel at CDF Run II, Ph. D. Thesis*, 2007.

[40] G. C. Fox and S. Wolfram, *Observables for the Analysis of Event Shapes in e+ e- Annihilation and Other Processes*, *Phys. Rev. Lett.* **41** (1978) 1581.

[41] C. Peterson, T. Rognvaldsson and L. Lonnblad, *JETNET 3.0: A versatile artificial neural network package*, *Comput. Phys. Commun.* **81** (1994) 185–220. We use a ROOT-based version of JETNET called Root_Jetnet which can be found online.

[42] D. Acosta *et. al.*, *The performance of the CDF luminosity monitor*, *Nucl. Instrum. Meth.* **A494** (2002) 57–62.

[43] O. Gonzalez and C. Rott, *Uncertainties due to the pdfs for the gluino-sbottom search*, 2004.

[44] E. Palencia *et. al.*, *Jet Probability B-Tag Efficiency Measurement Using Muon Transverse Momentum for 1.2 fb-1 analyses, CDF Note 8882*, 2004.

[45] F. Garberson *et. al.*, *Combination of the SecVtx 1.2fb^{-1} b-tagging scale factors, CDF Note 8666*, 2004.

[46] C. Rott, *Search for Scalar Bottom Quarks from Gluino Decays in Proton-Anitproton Collisions at 1.96 TeV, ph. d. thesis*, 2004.

[47] T. Junk, *Confidence level computation for combining searches with small statistics*, *Nucl. Instrum. Meth.* **A434** (1999) 435–443 [hep-ex/9902006].

[48] F. James and M. Roos, *Minuit: A system for function minimization and analysis of the parameter errors and correlations*, *Comput. Phys. Commun.* **10** (1975) 343–367.

[49] **CDF** Collaboration, T. T. W. Group, *Combined CDF and D0 Upper Limits on Standard Model Higgs- Boson Production with up to 2.4 fb-1 of data*, 0804.3423.